THE HONG KONG
POLYTECHNIC UNIVERSITY
香港理工大學
Pao Yue-kong Library
包玉剛圖書館

## Copyright Undertaking

This thesis is protected by copyright, with all rights reserved.

**By reading and using the thesis, the reader understands and agrees to the following terms:**

1. The reader will abide by the rules and legal ordinances governing copyright regarding the use of the thesis.
2. The reader will use the thesis for the purpose of research or private study only and not for distribution or further reproduction or any other purpose.
3. The reader agrees to indemnify and hold the University harmless from and against any loss, damage, cost, liability or expenses arising from copyright infringement or unauthorized usage.

**IMPORTANT**

If you have reasons to believe that any materials in this thesis are deemed not suitable to be distributed in this form, or a copyright owner having difficulty with the material being included in our database, please contact lbsys@polyu.edu.hk providing details. The Library will look into your claim and consider taking remedial action upon receipt of the written requests.

Pao Yue-kong Library, The Hong Kong Polytechnic University, Hung Hom, Kowloon, Hong Kong

http://www.lib.polyu.edu.hk

# PIEZOELECTRICITY AND FERROELECTRICITY IN TWO-DIMENSIONAL LAYERED METAL THIOPHOSPHATES AND THEIR APPLICATIONS

**IO WENG FU**

**PhD**

**The Hong Kong Polytechnic University**

**2025**

**The Hong Kong Polytechnic University**
**Department of Applied Physics**

# Piezoelectricity and Ferroelectricity in Two-dimensional Layered Metal Thiophosphates and Their Applications

**IO Weng Fu**

A thesis submitted in partial fulfillment of the requirements for the degree of Doctor of Philosophy

**August 2024**

# CERTIFICATE OF ORIGINALITY

I hereby declare that this thesis is my own work and that, to the best of my knowledge and belief, it reproduces no material previously published or written, nor material that has been accepted for the award of any other degree or diploma, except where due acknowledgement has been made in the text.

_____(Signed)

IO Weng Fu (Name of student)

# Abstract

Emerging two-dimensional (2D) van der Waals (vdW) layered materials possessing unprecedented properties, including atomically thin thickness, outstanding mechanical durability, and dangling bond-free surfaces, have garnered significant attention from fundamental research to various potential applications. In particular, they hold great promise to address the intrinsic size effect and constraints of lattice mismatch in ultrathin traditional piezoelectric and ferroelectric materials, opening up new opportunities for exploring ferroelectric and piezoelectric characteristics at low dimensions. However, most 2D layered piezoelectric materials discovered to date only exhibit piezoelectricity along in-plane direction, largely inhibiting their ability to be incorporated into vertical nanoelectronic device systems. Some out-of-plane piezoelectric materials have also been theoretically and experimentally reported but illustrate relatively weak piezoelectric response and low piezoelectric coefficients ($d_{33}$) compared to traditional piezoelectric materials. On the other hand, various 2D vdW materials are theoretically predicted with intrinsic ferroelectricity including $In_2Se_3$, monolayer group IV chalcogenides, and metal thiophosphates. Nevertheless, the experimental observations of robust room-temperature ferroelectricity in 2D layered materials, especially along the vertical direction, are still rather limited. Therefore, there

is an urgent need to search for strong vertical piezoelectricity in 2D materials with systematic investigations. Moreover, the experimental achievements in realizing intrinsic room-temperature ferroelectricity in 2D materials and studying the underlying mechanism are highly desired in developing multifunctional nanoelectronic devices.

As one of the most studied layered metal thiophosphates materials, $CuInP_2S_6$ (CIPS), with numerous intriguing characteristics including strong vertical piezoelectricity and ferroelectricity, shows immense promise for integration into vertical nanoelectronic device systems. In contrast to the extensive research to investigate its ferroelectric mechanisms and applications, the study on the piezoelectric effect of 2D CIPS and its relevant piezotronic device application is still in the early phases. In this thesis, a quantitative analysis of the high vertical piezoelectric responses in 2D CIPS nanosheets was performed and the potential device application as 2D piezoelectric nanogenerators (PENGs) fabricated on silicon substrates was demonstrated. Experimental result indicates a high $d_{33}$ piezoelectric coefficient of 17.4 pm $V^{-1}$ in few-layer CIPS that outperforms most 2D piezoelectric materials previously explored. Moreover, a prototype 2D CIPS-based PENG device illustrates a maximum piezoelectric power density of 70.4 nW $cm^{-2}$. The outstanding piezoelectric responses of 2D CIPS nanoflakes warrant their prospective utilizations in the next generation strain-modulable nanoscale electronic and piezotronic devices integrated with the

conventional silicon-based chips.

Recently, the isostructural layered metal thiophosphate $CuCrP_2S_6$ (CCPS) has been evidenced theoretically and experimentally the possibility of realizing 2D multiferroicity, which is of great significance from both fundamental physics and device application perspectives. Nevertheless, incorporating magnetic Cr cations in the ferroelectric framework results in antiferromagnetic and antiferroelectric orderings, whereas macroscopic spontaneous polarization is always lacking. Here, the direct observation of robust longitudinal ferroelectricity in 2D vdW layered CCPS at room temperature is reported with an in-depth investigation. Modification of the ferroelectric domain phase in 2D CCPS nanosheets is achieved experimentally by scanning probe technique. External electric field-induced polarization switching loops are acquired in CCPS down to 2.6 nm (around four layers). More importantly, the atomically resolution scanning transmission electron microscopy study unveiled the origin of the emergent room-temperature out-of-plane ferroelectricity in 2D CCPS layers. This comprehensive experimental study shall promote the development of multifunctional nanoelectronic devices and shed light on understanding the fundamentals of ferroelectric order of this 2D novel vdW material. As a proof-of-concept demonstration for the possible applications of ultrathin ferroelectric CCPS, various prototype devices including ferroelectric tunneling junction, ferroelectric diode, and ferroelectric field-effect

transistor were further constructed and characterized. Their applications as non-volatile memory devices operating at room temperature were presented and the feasibility of constructing heterostructures for multifunctional device applications was demonstrated. These findings signify the promising applications of 2D CCPS nanosheets in efficient nanoelectronic devices.

# List of Publications

1. **W.F. Io**, M.C. Wong, S.Y. Pang, Y. Zhao, R. Ding, F. Guo, J. Hao*, Strong piezoelectric response in layered $CuInP_2S_6$ nanosheets for piezoelectric nanogenerators. *Nano Energy* 2022, 99, 107371.

2. **W.F. Io**, S-Y. Pang, L.W. Wong, Y. Zhao, R. Ding, J. Mao, Y. Zhao, F. Guo, S. Yuan, J. Zhao, J. Yi, J. Hao*, Direct observation of intrinsic room-temperature ferroelectricity in 2D layered $CuCrP_2S_6$. *Nat. Commun.* 2023, 14, 7304.

3. S-Y. Pang‡, **W.F. Io**‡, L.W. Wong, J. Zhao, J. Hao*, Direct and *in situ* growth of 1T′ $MoS_2$ and 1T $MoSe_2$ on electrochemically synthesized MXene as an electrocatalyst for hydrogen generation. *Nano Energy* 2022, 103, 107835.

4. S-Y. Pang‡, **W.F. Io**‡, F. Guo, Y. Zhao, J. Hao*, Two-dimensional MXene-based devices for information technology. *Mater. Sci. Eng. R* 2025, 163, 1008942024.

5. S.Y. Pang, **W.F. Io**, J. Hao*, Facile Atomic-Level Tuning of Reactive Metal–Support Interactions in the Pt QDs@ HF-Free MXene Heterostructure for Accelerating pH-Universal Hydrogen Evolution Reaction. *Adv. Sci.* 2021, 8, 2102207.

6. F. Guo, M. Song, M.C. Wong, R. Ding, **W.F. Io**, S.Y. Pang, W. Jie, J. Hao*, Multifunctional optoelectronic synapse based on ferroelectric van der Waals heterostructure for emulating the entire human visual system. *Adv. Funct. Mater.* 2022, 32, 2108014.

7. R. Ding, Y. Lyu, Y. Zhao, Z. Wu, F. Guo, **W.F. Io**, S.Y. Pang, J. Mao, M.C. Wong, L.W. Wong, C, Yan, J. Yu, J. Zhao, G. Li, J. Hao*, Revealing photovoltaic behavior in 2D hybrid perovskite ferroelectric single-crystalline microwire arrays for self-powered photodetectors. *Mater. Today Phys.* 2022, 1011, 28, 100867.

8. W. Han, X. Zheng, K. Yang, C.S. Tsang, F. Zheng, L.W. Wong, K.H. Lai, T. Yang, Q. Wei, M. Li, **W.F. Io**, F. Guo, Y. Cai, N. Wang, J. Hao, S. Lau, C.-S. Lee, T.H. Ly*, M. Yang*, J. Zhao*, Phase-controllable large-area two-

dimensional $In_2Se_3$ and ferroelectric heterophase junction. *Nat. Nanotech.* 2022, 1-9.

9. F. Guo, **W.F. Io**, Z. Dang, R. Ding, S.Y. Pang, Y. Zhao, J. Hao*, Achieving reinforcement learning in a three-active-terminal neuromorphic device based on a 2D vdW ferroelectric material. *Mater. Horiz.* 2023, 10 (9), 3719-3728.

10. S. Yuan, Y. Zhang, M. Dai, Y. Chen, H. Yu, Z. Ma, **W.F. Io**, X. Luo, P. Hou, J. Hao*. A giant tunable piezoelectric performance in two-dimensional $In_2Se_3$ via interface engineering. *Advan. Electron. Mater.* 2023, 10, 2300741.

11. Y. Zhao, F. Guo, S.Y. Pang, **W.F. Io**, L.W. Wong, J. Zhao, and J. Hao*, Piezoelectric substrate-induced strain engineering on tuning polarized Raman spectra of crystalline black phosphorus. *Appl. Phys. Lett.* 2023, 122, 132903.

12. S. Shi, Y. Si, Z. Li, S. Meng, S. Zhang, H. Wu, H. Zhou, C. Zhi, **W.F. Io**, Y. Ming, D. Wang, B. Fei, H. Huang, J. Hao, J. Hu*, An intelligent wearable filtration system for health management. *ACS Nano* 2023, 17, 7, 7035–7046.

13. H. Wu, S. Shi, H. Zhou, C. Zhi, S. Meng, **W.F. Io**, Y. Ming, Y. Wang, L. Lei, B. Fei, J. Hao, J. Hu*, Stem cell self-triggered regulation and differentiation on polyvinylidene fluoride electrospun nanofibers. *Adv. Funct. Mater.* 2024, 34, 2309270.

14. Y. Ming, Z. Cheng, S. Shi, J. Su, **W.F. Io**, H. Wu, J. Li, B. Fei, Nanoarchitectonics toward full coverage of CdZnS nanospheres by layered double hydroxides for enhanced visible-light-driven $H_2$ evolution. *Small* 2024, 2309750.

15. C. Zhi, S. Zhang, H. Wu, Y. Ming, S. Shi, **W.F. Io**, S. Meng, Y. Si, B. Fei, J. Hao, J. Hu*, Perovskite nanocrystals induced core–shell inorganic–organic nanofibers for efficient energy harvesting and self-powered monitoring. *ACS Nano* 2024, 18, 9365-9377.

16. H. Chen, J. Shen, X. Du, S. Cai, F. Guo, **W.F. Io**, T. Zhou, Z. Dong, T. Bian, J. Guo, W. Liu, Y. Zhang*, Z. Wu*, J. Hao*, Frequency converting and digital modulation of light derived from lanthanide for signal encoding and logic computing. *InfoMat* 2024, 6, e12547.

17. Y. Zhao, J. Mao, Z. Wu, **W.F. Io**, S.-Y. Pang, and J. Hao*, A clean transfer approach to prepare centimetre-scale black phosphorus crystalline multilayers on silicon substrates for field-effect transistors. *Nat. Commun.* 2024, 15, 6795.

18. J. Mao, J. He, **W.F. Io**, F. Guo, Z. Wu, M. Yang, J. Hao*, Strain-engineered ferroelectricity in 2H bilayer $MoS_2$. *ACS Nano* 2024, 18, 30360–30367.

19. C. Li, M.Telychko, Y. Zheng, S.Yuan, Z. Wu, W.P.D. Wong, Y. Li, Y. Jin, **W.F. Io**, X. Wang, J. Lin, J. Hao, C. Han*, K. Leng*, Switchable planar chirality and spin texture in highly ordered ferroelectric hybrid perovskite domains. *Nat Commun* 2024, 15, 10221.

20. X. Yue, Yipu Xia, D. Ding, **W.F. Io**, D. He, C. He, Y. Wang, H. Xue, Y. Jin, M. Yuan, J. Zhang, W. Ho, H. Xu, D.-K. Ki, J. Hao, C. Jin, M. Xie*, Single-layer MoSeN – a synthetic Janus two-dimensional transition-metal compound grown by plasma-assisted molecular beam epitaxy. *2D Mater.* 2025, 12, 025004.

# Acknowledgements

First and foremost, I would like to express my deepest gratitude to my supervisor, Prof. Jianhua Hao, for his patient guidance and invaluable supervision throughout my three years of Ph.D. study. His expertise, profound insights, and passionate attitude towards research influenced and encouraged me a lot throughout the duration of my postgraduate research. He not only gave inspiring advice and valuable assistance in research, but also provided sufficient care and continuous support in my daily life.

I am grateful to Dr. Hardy Lui and Dr. Terence Wong for their assistance in equipment utilization for my research works.

I would also like to express my thankfulness to my fellow postgraduate colleagues Dr. Sin Yi Pang, Ms. Yuqian Zhao, Dr. Man-Chung Wong, Dr. Feng Guo, Dr. Jianfeng Mao, Prof. Ran Ding, Mr. Yifei Zhao, and Dr. Zehan Wu for their great support and encouragement, engaging discussions, and the friendship we established in my academic journey.

I would like to acknowledge the financial support from Research Grants Council of Hong Kong (ref. no. PF20-46080), which allowed me to devote myself fully to this research work.

Finally, I would like to express my deepest thanks to my family for their

continuous support, encouragement, and unwavering love and understanding in my three years of postgraduate study in PolyU. I am also grateful to my friends who accompanied me all the way through this process and provided me with emotional and moral support.

# Table of Content

Abstract ..... I

List of Publications ..... V

Acknowledgements ..... VIII

Table of Content ..... X

List of Figures ..... XIII

List of Table ..... XXIV

Chapter 1 Introduction ..... 1

1.1 Two-dimensional van der Waals materials ..... 1

1.2 Piezoelectricity and ferroelectricity in ultrathin materials ..... 2

1.2.1 Traditional piezoelectric and ferroelectric materials ..... 2

1.2.2 Size effect in traditional ferroelectric perovskite thin films ..... 6

1.2.3 2D vdW layered piezoelectric and ferroelectric materials ..... 8

1.3 Metal thiophosphate materials ..... 14

1.4 Motivation and significance of the research ..... 16

1.5 Structure of the thesis ..... 18

Chapter 2 Experimental Details ..... 21

2.1 Preparation of ultrathin materials ..... 21

2.2 Material characterization ..... 24

2.2.1 Optical microscopy ..... 24

2.2.2 Second-harmonic generation spectroscopy ..... 25

2.2.3 Raman spectroscopy ..... 26

2.2.4 Ultraviolet photoelectron spectroscopy ..... 28

2.2.5 X-ray diffraction ..... 29

2.2.6 Scanning transmission electron microscopy ..... 30

2.2.7 Energy dispersive X-ray spectroscopy ..... 32

2.2.8 Probe station with a semiconductor analyzer ..... 33

2.2.9 Scanning probe microscopy ..... 34

2.2.10 Theoretical calculations ..... 38

Chapter 3 Strong Piezoelectricity in 2D Layered CIPS for Piezoelectric Nanogenerators ..... 40

3.1 Introduction ..... 40

3.2 Structural characterization of CIPS nanoflakes ..... 43

3.3 Piezoelectric and ferroelectric characterizations ..... 47

3.4 Piezotronics effect in 2D CIPS-based nanodevices ..... 58

3.5 Performance of CIPS-based piezoelectric nanogenerators ..... 70

3.6 Summary ..... 77

Chapter 4 Direct Observation of Intrinsic Room-Temperature Out-of-plane Ferroelectricity in

vdW Layered CCPS Nanoflakes ..... 79

4.1 Introduction ..... 79

4.2 Crystal structure characterization of CCPS nanoflakes ..... 82

4.3 Room-temperature ferroelectricity 2D CCPS nanoflakes ..... 86

4.4 Origin of the intrinsic out-of-plane ferroelectricity in CCPS ..... 99

4.5 Summary ..... 106

Chapter 5 Nanoelectronic Devices based on 2D Ferroelectric CCPS ..... 107

5.1 Introduction ..... 107

5.2 Electronic structure of CCPS ..... 107

5.3 Performance of ferroelectric CCPS-based nanoelectronic devices ..... 110

5.3.1 Ferroelectric tunneling junction ..... 110

5.3.2 Ferroelectric diode ..... 112

5.3.3 Ferroelectric field-effect transistor ..... 116

5.4 Summary ..... 122

Chapter 6 Conclusions and Future Prospects ..... 123

6.1 Conclusions ..... 123

6.2 Future prospects ..... 125

References ..... 129

# List of Figures

**Figure 1.1** *P-E* hysteresis loop for a conventional ferroelectric material[31]..... 4

**Figure 1.2** Summary of the potential applications of ferroelectric materials[35]..... 5

**Figure 1.3** (a) Calculated Curie temperature versus PTO film thickness[36]. (b) The normalized polarization as a function of thickness for traditional ferroelectric perovskite oxides[37]. ..... 6

**Figure 1.4** (a) Piezoelectric current outputs of 2H $MoS_2$ with varying thicknesses[51]. (b) $d_{33}$ piezoelectric coefficient of 3R $MoS_2$ with respect to the thickness of the samples[64]..... 10

**Figure 1.5** Experimental evidences of ferroelectricity in various 2D vdW materials (a) SnTe[65], (b) $WTe_2$[66], and (c) d1*T*-$MoTe_2$[67]. ..... 11

**Figure 2.1** Te preparation of 2D materials through mechanical and liquid-phase exfoliation strategies[98]. ..... 22

**Figure 2.2** Working mechanism of Raman spectroscopy[99]. ..... 26

**Figure 2.3** Schematic of operating principle of X-ray diffraction. ..... 29

**Figure 2.4** Schematic of the working principle of UPS investigation on (a) metallic and (b) semiconducting materials.[100] ..... 32

**Figure 2.5** Setup of the probe station system employed in this work. ..... 34

**Figure 2.6** Schematic diagram of the operation principle of the tapping imaging mode in scanning probe microscopy. ..... 35

**Figure 2.7** Setup of the DART- PFM operating mode. ..... 37

**Figure 3.1** (a) Illustration of the atomic configuration from both the top and side perspectives of the CIPS crystal with non-centrosymmetric nature. (b) SHG response from CIPS under ambient conditions, excited by a laser with a 900 nm wavelength. ..... 43

**Figure 3.2** Raman spectra for CIPS nanoflakes of varying thicknesses under ambient conditions, by utilizing a 532 nm laser for excitation. ..... 44

**Figure 3.3** XRD analysis of CIPS crystal measured under ambient conditions. ..... 45

**Figure 3.4** (a) A high-resolution TEM image of a mechanical exfoliated CIPS flake, and (b) the associated SAED pattern. ..... 46

**Figure 3.5** Topography and PFM phase images showing clear ferroelectric domains in both out-of-plane and in-plane direction, and the height profiles of the characterized CIPS samples. ..... 47

**Figure 3.6** (a)-(c) Images depicting the surface topography and height profiles. (d)-(f) The respective out-of-plane ferroelectric hysteresis loops for CIPS nanoflakes of varying thicknesses at 9 nm, 14.4 nm, and 24 nm, respectively. ..... 48

**Figure 3.7** (a) Morphography and (b) height profile of a 28 nm CIPS nanoflake. (c) PFM amplitude and phase images before and after domain modification with box pattern. ..... 48

**Figure 3.8** AFM topographic image of mechanically exfoliated CIPS nanoflakes with different thicknesses. ..... 50

**Figure 3.9** Out-of-plane PFM amplitude images of CIPS nanoflakes exfoliated on $SiO_2$ substrate measured under different bias from 1 V to 4 V, respectively. ..... 51

**Figure 3.10** Out-of-plane PFM phase images of CIPS nanoflakes exfoliated on $SiO_2$ substrate conducted under tips voltages from 1 V to 4 V, respectively. Scale: 2 μm. ..... 52

**Figure 3.11** (a) A schematic diagram illustrating the PFM set-up employed in this study to evaluate the out-of-plane piezoelectric response of CIPS nanoflakes. (b) A depiction showing the correlation between the vertical amplitude responses and the voltage that the conductive AFM tip applied to the CIPS flakes. ..... 53

**Figure 3.12** (a) The relationship between the $d_{33}$ piezoelectric constant and the thickness of the CIPS nanoflakes. (b) Comparison of the $d_{33}$ coefficient of CIPS and α-$In_2Se_3$ nanoflakes under identical measurement conditions. ..... 56

**Figure 3.13** (a) Polarization hysteresis loop and (b) capacitance-electric field curve of CIPS[124]. ..... 56

**Figure 3.14** (a) An array of patterned Au electrodes. (b)-(d) Optical images of several fabricated vertical CIPS devices on $SiO_2$ substrates. Scale bar:10 μm. ..... 58

**Figure 3.15** (a)(c) Optical images and (b)(d) the corresponding AFM images and height profiles of typical vertical CIPS devices with symmetric top and bottom Au electrodes. ..... 59

**Figure 3.16** Electrical characteristics of the ferroelectric CIPS sample when the applied bias ..... 60

$V<V_C$ (Schottky junction behavior) and $V>V_C$ (resistive switching behavior). Inset: enlarged view of the *I-V* curve. ..... 60

**Figure 3.17** *I-V* characteristics of the fabricated CIPS device on rigid $SiO_2$ substrate subjected to varying degrees of compressive stress. ..... 62

**Figure 3.18** (a) The value of ln *I* as a function of $V^{1/4}$ based on the experimental data from Figure 3.17. (b) Output current under different stressed conditions with an external voltage of ± 0.5 V. (c) The estimated variation in Schottky barrier height corresponding to the compressive force exerted, extracted at external voltages of ± 0.3 V and ± 0.5 V, respectively. ..... 64

**Figure 3.20** Band diagrams under different situations: (a) no external voltage and unstressed; (b) a non-zero external voltage is applied to unstressed CIPS flake causing the energy bands to tilt; (c) with the application of compressive stress along with a non-zero external voltage, which results in the generation of a piezopotential at the metal-semiconductor interfaces. $\Phi_S$ and $\Phi_D$

represent the initial heights of the Schottky barriers at the source and drain contacts, and $\Phi_{S,C}$ and $\Phi_{D,C}$ denote the changes in barrier heights at the source and drain modulated due to the piezoelectric polarization charges, respectively. ..... 68

**Figure 3.21** A schematic diagram demonstrating the experimental setup to analyze the 2D CIPS PENGs in this work. ..... 70

**Figure 3.22** The (a) voltage and (b) current output of a 45 nm CIPS PENG device induced by periodic longitudinal compression. ..... 72

**Figure 3.23** The (a) voltage and (b) current output of a 15 nm CIPS PENG device under the application of periodic longitudinal compression. ..... 72

**Figure 3.24** The peak output piezoelectric current and power density of a 2D CIPS PENG device under different loading resistances. ..... 73

**Figure 3.25** Endurance test of a prototype 2D CIPS PENG under periodic compression and relax over 1200 seconds. ..... 73

**Figure 3.26** The piezoelectric output voltages generated by the CIPS PENG in the forward and reverse connections, respectively. ..... 75

**Figure 3.27** Voltage output recorded from PMMA-coated bare $SiO_2$ substrate. ..... 76

**Figure 3.28** (a) Schematic of the energy harvesting device based on piezoelectric CIPS and (b) the generated piezoelectric currents when subjected to different levels of compressive stress. ..... 77

**Figure 4.1** Raman spectra of exfoliated CCPS samples with different thicknesses, measured under ambient conditions. ..... 82

**Figure 4.2** Raman spectra of exfoliated CCPS at the temperature of 298 K and 248 K, respectively..... 82

**Figure 4.3** XRD spectrum of CCPS single crystal, conducted under ambient conditions..... 83

**Figure 4.4** EDX spectrum and elemental mapping of mechanically exfoliated CCPS sample. ..... 84

**Figure 4.5** (a) Top-view atomic structure of CCPS. (b) HRTEM image and (c) corresponding SAED pattern of CCPS. ..... 85

**Figure 4.6** Optical microscopy images of several prototype vertical Au/CCPS/Au device structures. ..... 86

**Figure 4.7** *P-E* hysteresis measurement of CCPS**.** (a) Voltage pulses (black) and current output (blue) in the PUND measurement. (b) Calculated *P-E* hysteresis loop of 0.2 μm CCPS. ..... 87

**Figure 4.8** (a)-(c) Topography of CCPS nanoflakes and the corresponding (d)-(f) amplitude and (g)-(i) phase images illustrating the ferroelectric domains as visualized by vertical PFM. Scale bar: 10 μm, 2 μm, and 1 μm, respectively. ..... 88

**Figure 4.9** (a) Topography (b)-(f) and out-of-plane amplitude images of CCPS nanoflakes under various AC voltages from 1 V to 3 V. ..... 89

**Figure 4.10**. (a) Surface topography and (b) corresponding PFM phase images of ultrathin CCPS samples. (c) AFM height profile of a CCPS nanoflake with the thickness of ~2.6 nm, corresponding to 4 CCPS layers. (d) Off-field PFM phase and amplitude hysteresis switching of the 2.6 nm CCPS nanoflake. ..... 90

**Figure 4.11** Out-of-plane off-field PFM amplitude (black) and phase (blue) hysteresis loops of CCPS nanoflakes with the thicknesses of (a)-(i) 3.3, 5, 6, 8, 15, 20, 79, 171, and 286 nm, respectively. ..... 91

**Figure 4.12** Out-of-plane off-field PFM hysteresis loops with (a) different DC voltage sweeps and (b) different measuring frequencies. ..... 93

**Figure 4.13** Thickness dependence of the ferroelectric coercive field of CCPS nanoflakes in double logarithmic scale. ..... 94

**Figure 4.14** (a) AFM topography, (b) ferroelectric domain modification imaged by PFM phase mapping by writing box patterns with ± 8 V, and (c) the corresponding PFM off-field phase and amplitude hysteresis loops of a 12 nm CCPS nanoflake. ..... 95

**Figure 4.15** (a) AFM topography, (b) ferroelectric domain modification imaged by PFM phase mapping by writing box patterns with ± 10 V, and (c) the corresponding PFM off-field phase and amplitude hysteresis loops of a 25 nm CCPS nanoflake. ..... 95

**Figure 4.16** (a) AFM topography, (b) ferroelectric domain modification imaged by PFM phase mapping by writing box patterns with ±10 V, and (c) the corresponding PFM off-field phase and amplitude hysteresis loops of an 82 nm CCPS nanoflake. ..... 96

**Figure 4.17** AFM topography and height profile of the CCPS sample for temperature-dependent ferroelectric domain observation..... 98

**Figure 4.18** Temperature-dependent observation of the ferroelectric domain in CCPS nanoflake from room temperature to 338 K and returns to room temperature..... 98

**Figure 4.19** (a) SHG signals measured from exfoliated CCPS samples at various temperatures and (b) the temperature-dependent SHG peak intensities. ..... 99

**Figure 4.20** Atomically resolved HAADF-STEM images of the cross-section of CCPS with (a) positive and (c) negative spontaneous polarization, respectively. Scale: 1 nm. (b)-(d) Z-contrast intensity profiles along the dashed lines corresponding to (a) and (c), respectively..... 100

**Figure 4.21** (a) Atomic resolution HAADF-STEM image of paraelectric phase CCPS and (b) the corresponding intensity profile along the dashed line. Scale: 1 nm. ..... 102

**Figure 4.22** (a) (c) HAADF-STEM images, and the corresponding colored DPC-STEM images indicating uniform (b) upward and (d) downward electric polarization fields in CCPS. Scale: 2 nm. ..... 103

**Figure 4.23** (a) Atomic model of CCPS with out-of-plane ferroelectricity. (b) Charge density difference between the ferroelectric and the paraelectric phase CCPS, the yellow and cyan region represents excess and depletion of charges respectively. ..... 104

**Figure 5.1** SKPM potential mappings of freshly cleaved HOPG surface at several randomly selected areas. The $V_{CPD}$ are -0.868 V, -0.847 V and -0.870 V, respectively..... 107

**Figure 5.2** SKPM characterization of CCPS nanoflakes. (a) Surface topography and (b) surface potential mapping of CCPS nanoflakes exfoliated on Pt substrate. ..... 108

**Figure 5.3** Simulation of the (a) electronic band structure and (b) DOS of CCPS in ferroelectric phase. ..... 109

**Figure 5.4** (a) UPS study of single crystalline CCPS. (b) Energy band diagram of CCPS sketched based on theoretical and experimental data. ..... 109

**Figure 5.5** (a) *I–V* characteristic of a vertical Pt/CCPS/MLG FTJ device with 3.3-nm-thick CCPS by voltage sweeping back and forth. (b) *I–V* characteristic of a representative Pt/CCPS/Pt resistive switching ferroelectric diode, with the channel CCPS nanoflake of 8.5 nm thick.. 111

**Figure 5.6** Schematic of the band structure of the Pt/CCPS/MLG FTJ device. ..... 112

**Figure 5.7** Electrical characterization of CCPS-based VFDs. (a)-(c) Resistive switching characteristics of the Pt/CCPS/Pt-structured VFDs with CCPS nanosheets of 7.2, 9.3, and 9.9 nm thick, respectively..... 113

**Figure 5.8** (a) Cycling measurement of the resistive switching characteristics and (b) retention test of the HRS and LRS states of the CCPS-based VFD. ..... 113

**Figure 5.9** Schematic of the band structure of the Pt/CCPS/Pt VFD. ..... 115

**Figure 5.10** *I-V* measurement of an Au/CCPS/Au VFD with a 280 nm thick ferroelectric CCPS flake. ..... 115

**Figure 5.11** (a) Schematic diagram of the fabricated FeFET device based on ferroelectric CCPS nanosheets. (b) Optical microscopy image of a prototype fabricated FeFET device. (c) AFM height profiles of the CCPS, h-BN, and $WSe_2$ nanosheets utilized in this FeFET device. ... 117

**Figure 5.12** Leakage current (gate current) measured from different FeFET devices in which (a) h-BN is not used, and (b) 7 nm h-BN and (c) 20 nm h-BN layer are utilized. ..... 118

**Figure 5.13** Raman spectra of 2D CCPS, $WSe_2$, and stacked CCPS/$WSe_2$ layers. ..... 119

**Figure 5.14** (a) Transfer characteristic ($I_{DS}$-$V_{DS}$) of the 2D semiconducting $WSe_2$ channel when no gate voltage is applied. (b) $I_{DS}-V_{TG}$ characteristics of the FeFET device measured at top-gate voltage sweep from −5 to 5 V and at $V_{DS}$ from 0.01 to 0.5 V. (c) $I_{DS}-V_{TG}$ characteristics at different gate voltage sweeps. (d) The distribution of HRS and LRS of the CCPS-based FeFET device in 100 consecutive polarization reversal by ± 7 V gate voltage sweep and read at -1 V gate voltage..... 121

# List of Table

**Table 1** A summary of the critical thickness and polarization value of several experimentally verified 2D vdW ferroelectric materials. ..... 12

**Table 2.** Comparison of the experimental piezoelectric coefficient of 2D CIPS with the currently reported 2D vdW layered materials. ..... 55

# Chapter 1 Introduction

## 1.1 Two-dimensional van der Waals materials

The introduction of graphene, a monolayer of graphite, has sparked significant research interest in two-dimensional (2D) materials with atomically thin thickness. These atomically thin van der Waals (vdW) layered materials exhibit unique properties that are not observed in their bulk counterparts. The emergence of 2D vdW layered materials has opened up new possibilities in the semiconductor industry and applications in multifunctional electronic devices. Graphene, as the first and most comprehensively studied 2D material, exhibits remarkable electrical, mechanical, and optical characteristics including high thermal conductivity (around 4400-5800 W $mK^{-1}$), ultrahigh room temperature carrier mobility (10000 $cm^2$ $V^{-1}s^{-1}$), large theoretical surface area (2630 $m^2$ $g^{-1}$), excellent Young's modulus (around 1 TPa), and significant optical transparency (97.7 %). These features make graphene suitable for various device applications such as field-effect transistors (FETs), flexible solar cells, energy storage devices with high performance, and transparent conducting materials for optoelectronics[1-8]. Since its discovery in 2004, research on graphene has grown exponentially, with thousands of graphene-related research works published each year. Pristine graphene has been comprehensively investigated and is now commercially

exploited in numerous everyday applications with continuously improving quality.

Motivated by the exceptional properties of graphene, researchers have turned their attention to exploring other 2D vdW layered members that exhibit diverse material characteristics, including transition metal dichalcogenides (TMDs, such as $MoS_2$, $WS_2$, $MoSe_2$, $MoTe_2$)[9-13], metal oxides[14], black phosphorus (BP)[15-17], MXenes (e.g. $TiCT_x$, $V_2CT_x$)[18,19], and elemental metals[20]. The rapid expansion of 2D materials has facilitated the advancement of various synthesis methodologies including mechanical exfoliation, physical and chemical vapor deposition, pulsed laser deposition, molecular beam epitaxy, and electrochemical-etching to fabricate high-quality 2D thin films[16,21-23]. Intriguingly, the categories of 2D layered materials span from conductors, semiconductors to insulators and possess different bandgaps, offering immerse potential to be utilized in different functional sectors. The distinctive physical, electrical, and optical properties endow them as potential candidates for a wide range of applications such as nanoscale electronics, optoelectronics, sensors, catalysts, biomedicines, and energy harvesting and storage devices[24-26].

## 1.2 Piezoelectricity and ferroelectricity in ultrathin materials

### 1.2.1 Traditional piezoelectric and ferroelectric materials

The piezoelectric effect is a unique property exhibited in certain materials, in

which they generate electric charges when subjected to external mechanical stress. This effect is reversible such that internal deformation will happen in the material when an electric field is applied. Ferroelectricity, a sub-category of piezoelectricity, refers to the material property demonstrating the presence of two or more stable spontaneous electric polarizations in the absence of an external electric field, and the direction of this spontaneous polarization can be switched by applying an external electric field higher than the coercive field of the material. Generally, as the temperature exceeds the Curie temperature ($T_c$), the spontaneous polarization in ferroelectric materials will vanish, associated with a structural transformation from a non-symmetric ferroelectric phase to a symmetric paraelectric phase.

The macroscopic spontaneous polarization in conventional bulk ferroelectric materials is usually analyzed through polarization-electric field (*P*-*E*) hysteresis measurements, as depicted in Figure 1.1. Materials possessing piezoelectric and ferroelectric properties hold great potential for the developing functional devices including actuators, sensors, piezo-phototronic devices, energy harvesters, synapses, and data storage devices, driving advancements in technology[27-30].

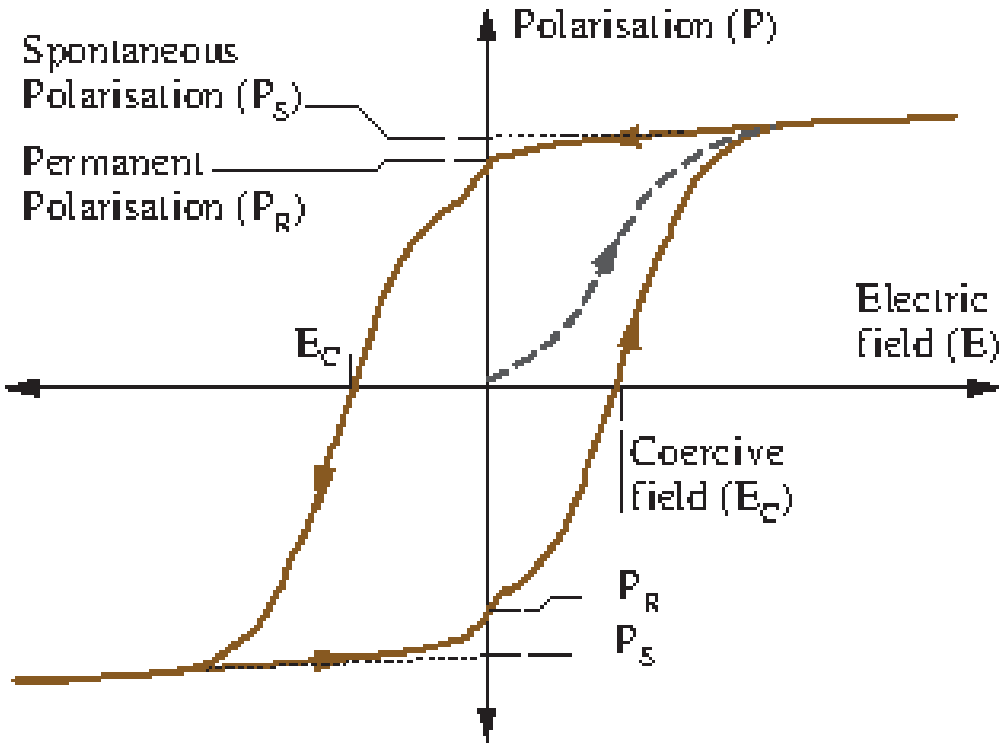


**Figure 1.1** *P-E* hysteresis loop for a conventional ferroelectric material[31].

The study of ferroelectrics can be traced back to the early demonstration of ferroelectricity in Rochelle salt by Valasek[32] in the previous century. This discovery has provoked extensive research on various ferroelectric candidates in the following decades. The most investigated ferroelectric perovskite materials have a general formula of $ABO_3$, where A represents alkali, alkaline earth, or rare earth ions such as $Ba^{2+}$, $Sr^{2+}$, or $Pb^{2+}$, while B corresponds to 3d, 4d, or 5d transition metal ions[33,34]. The ferroelectric phase in these perovskite oxides arises from a structural transformation occurring below the Curie temperature which involves the transition from a high-symmetry paraelectric cubic phase to a non-symmetric ferroelectric phase. During the paraelectric-ferroelectric phase transition, the A cations and B anions undergo

displacements relative to each other, resulting in the generation of stable electric dipoles within the unit cells. These dipoles do not coincide and give rise to the spontaneous polarization observed in ferroelectric perovskite oxides. The comprehensive studies of these ferroelectric materials and their unique properties has significantly contributed to the understanding of ferroelectric phenomena as well as practical applications.

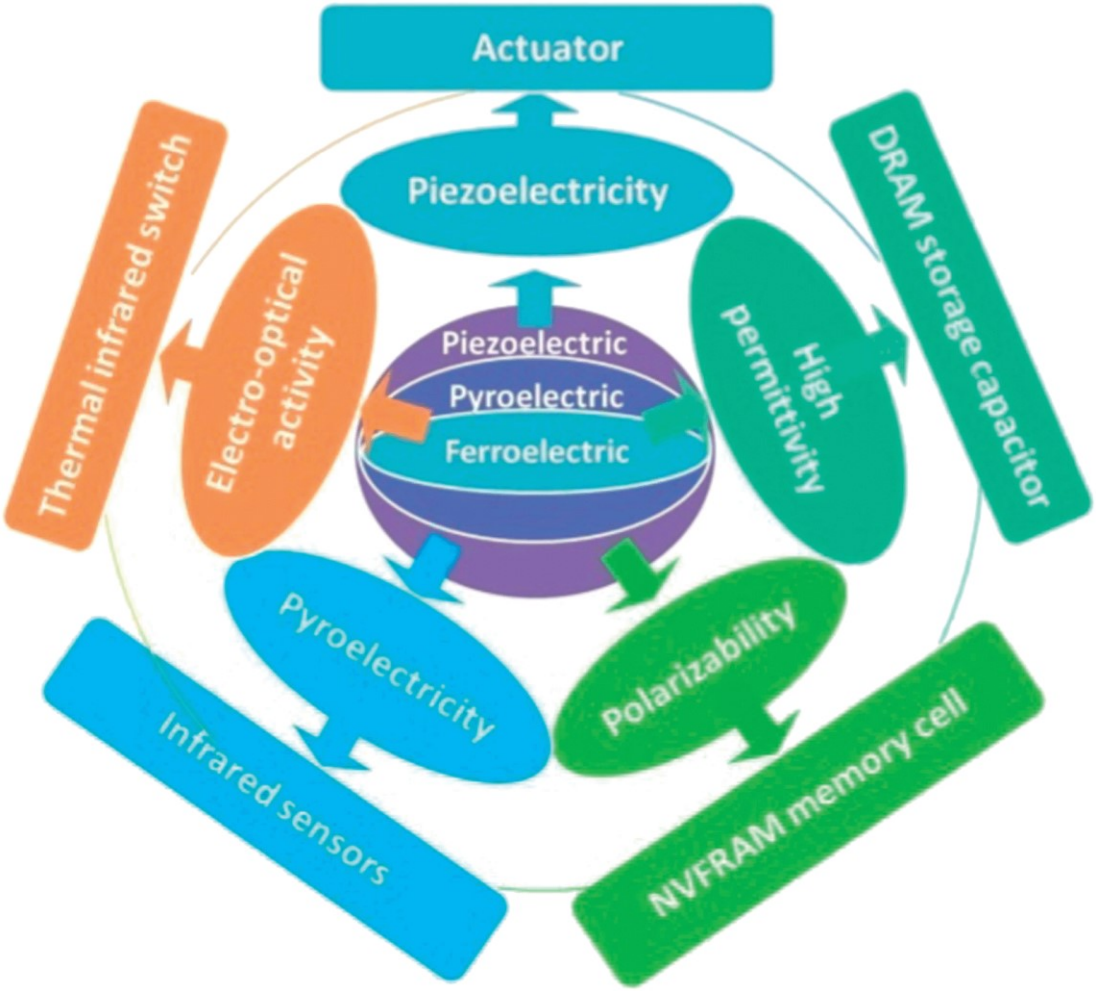


**Figure 1.2** Summary of the potential applications of ferroelectric materials[35].

### 1.2.2 Size effect in traditional ferroelectric perovskite thin films

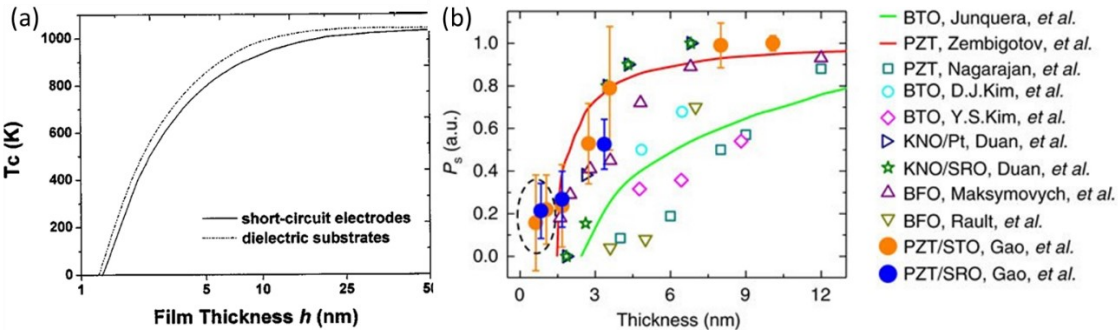


**Figure 1.3** (a) Calculated Curie temperature versus PTO film thickness[36]. (b) The normalized polarization as a function of thickness for traditional ferroelectric perovskite oxides[37].

The conventional perovskite oxide ferroelectric family includes materials such as $PbTiO_3$ (PTO), $Pb[Zr_xTi_{1-x}]O_3$ (PZT), $BaTiO_3$ (BTO), and $BiFeO_3$ (BFO). These materials have found widespread utilization in practical devices, including photovoltaic devices, memory devices, pyroelectric and piezoelectric sensors, and actuators[38-41]. In recent years, there has been a growing focus on ultrathin ferroelectric materials due to the trend towards miniaturization and integration of electronic devices, as well as rapid technological development. The demand for technological advancements has exposed the intrinsic size effects in traditional ferroelectrics[42,43]. Their ferroelectric polarization field originates from the non-centrosymmetric crystal structure that forms electric dipole moments within the materials. Owing to the cooperative behavior of these dipoles and the uncompensated charges accumulated at the material interfaces, an

internal depolarization field perpendicular to the surface is generated. It was believed that ferroelectricity in ferroelectric perovskite oxides would disappear below a certain critical size of around tens of nanometers, with poor compatibility with complementary metal-oxide-semiconductor (CMOS) technology[37,44]. Notably, the Curie temperature and polarization strength of conventional ferroelectric perovskites also decrease with the film thickness as they approached the 2D limit[37,45].

In the 2000s, significant efforts were made to overcome the challenges posed by the depolarization field in perovskite ferroelectrics. Remarkable advancements were achieved in thin-film fabrication techniques, allowing several traditional oxide ferroelectrics to maintain their ferroelectric properties even in atomically thin layers. For instance, in 2003, Junquera et al.[42] demonstrated the potential of sustaining ferroelectricity in BTO film to a thickness of 2.4 nm with the use of $SrRuO_3$ electrodes , through first-principles calculations. Furthermore, in 2004, Fong at al.[45] epitaxially deposited PTO films on insulating $SrTiO_3$ substrates, which exhibited stable room-temperature ferroelectricity with the thickness down as low as 1.2 nm. The selection of lattice-matched substrates resulted in the PTO films polarizing only in the longitudinal direction because of compressive strain. However, preserving the ferroelectric properties in ultrathin perovskite oxide films still remains a challenge. It is necessary to cooperate with specific electrodes and/or careful selecting substrates with small

lattice mismatch to the ferroelectric materials, which severely hinder the development of interface-assembling heterostructures and restrict their possibility in nanoelectronic applications towards miniaturization. Additionally, the introduction of defects and dangling bonds during high-temperature deposition and device fabrication procedure are often unavoidable, which can potentially degrade the ferroelectric performance of the ferroelectric oxide thin films[46,47].

### 1.2.3 2D vdW layered piezoelectric and ferroelectric materials

In contrast to the challenges faced with traditional ferroelectric perovskite oxides, the investigation of the first 2D monolayer graphene, has sparked a large amount of research into the exploration of potential ultrathin piezoelectric and ferroelectric materials with different crystal structures than the typical ferroelectrics. Considerable progress has been made in various aspects, including synthesis approaches, property characterizations, and the design of ferroelectric devices[48,49]. Several novel ultrathin vdW layered ferroelectric materials have been theoretically predicted and verified experimentally to exhibit ferroelectricity. Compared to traditional ferroelectric oxide materials and Hf/$ZrO_2$-based systems[50], 2D layered materials offer the advantages of an atomically thin structure, good mechanical durability, excellent carrier mobility, no constraints of lattice mismatch, surfaces free of dangling-bond, and high compatibility

with other materials[44,45,57]. More importantly, they offer the possibility of constructing vdW heterostructures without the restriction of lattice matching, which is a major limitation in traditional ferroelectric oxide systems[51,52]. These unique properties of 2D vdW ferroelectric materials can provide substantial advantages over traditional ferroelectric oxides. They hold promise to overcome the depolarization effect while retaining desirable piezoelectric and ferroelectric properties. Particularly, their high CMOS compatibility with various substrates make them appealing in the pursuit of integration in miniaturized electronic device applications with high performance and low power consumptions.

Since the discovery of 2D piezoelectricity in monolayer $MoS_2$ by Wang's group, tremendous theoretical and experimental investigations have been conducted to predict and verify piezoelectric properties in atomically thin layered materials, including monolayer TMDs[51,53,54], 2D wurtzite structures[55-58], group-IV monochalcogenide monolayers[59], and group-V binary compounds[60]. Nevertheless, the piezoelectric polarization of most newly explored members of the piezoelectric family is limited only to the in-plane direction. This in-plane-restricted piezoelectricity significantly hinders their ability to be incorporated into vertical nanoelectronic architectures. Furthermore, the majority of the currently reported 2D layered piezoelectric materials exhibit layer-dependent piezoelectric properties. For example, the in-plane piezoelectricity is often

limited to monolayer or few-layer TMDs, and their piezo-polarization strength diminishes as the film thickness increases[51,61], as shown in Figure 1.4a. Moreover, certain 2D piezoelectric materials present an odd-even-layer dependency, where piezoelectric characteristics can only be identified in odd layers[51,62,63].

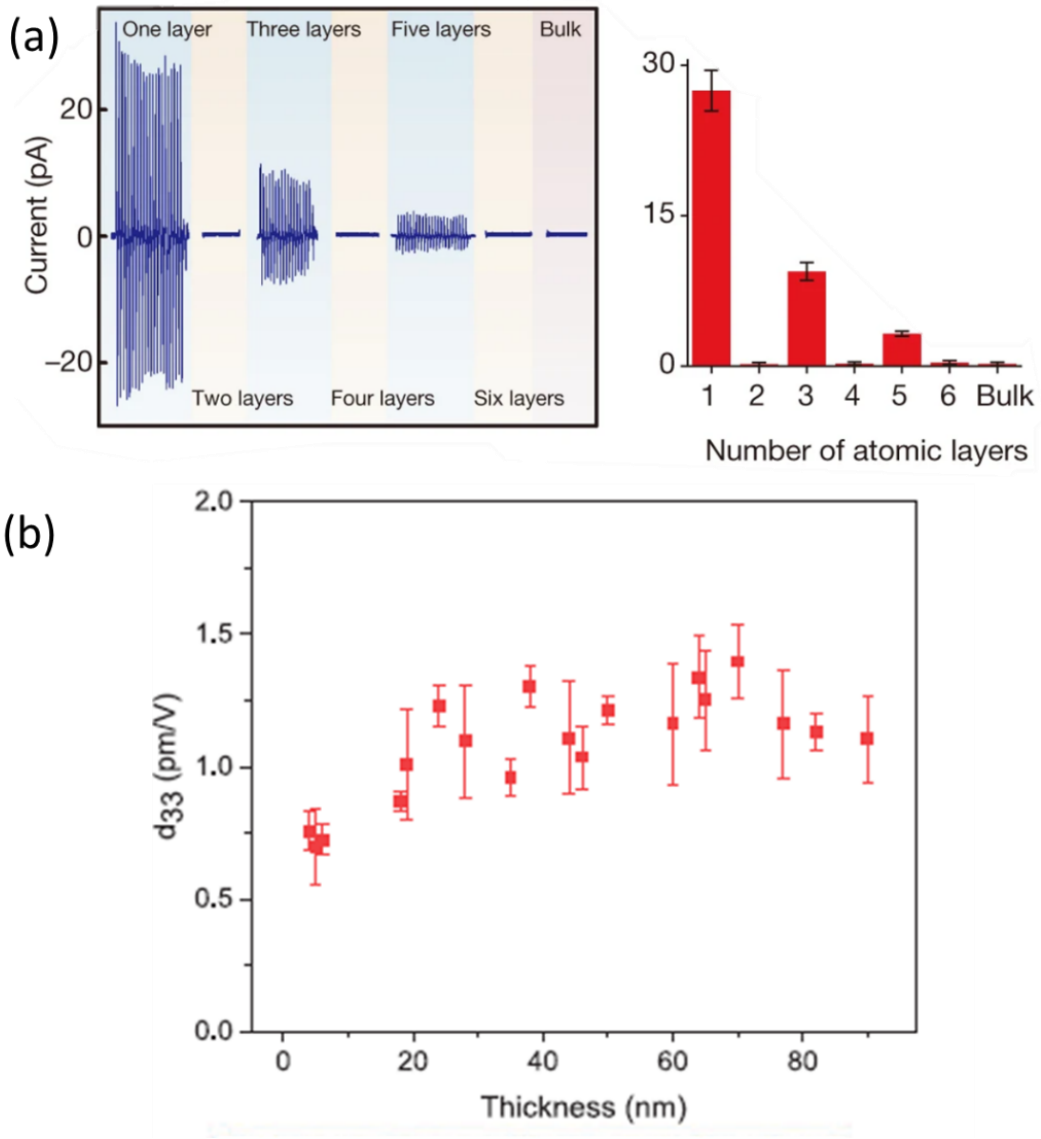


**Figure 1.4** (a) Piezoelectric current outputs of 2H $MoS_2$ with varying thicknesses[51]. (b) $d_{33}$ piezoelectric coefficient of 3R $MoS_2$ with respect to the thickness of the samples[64].

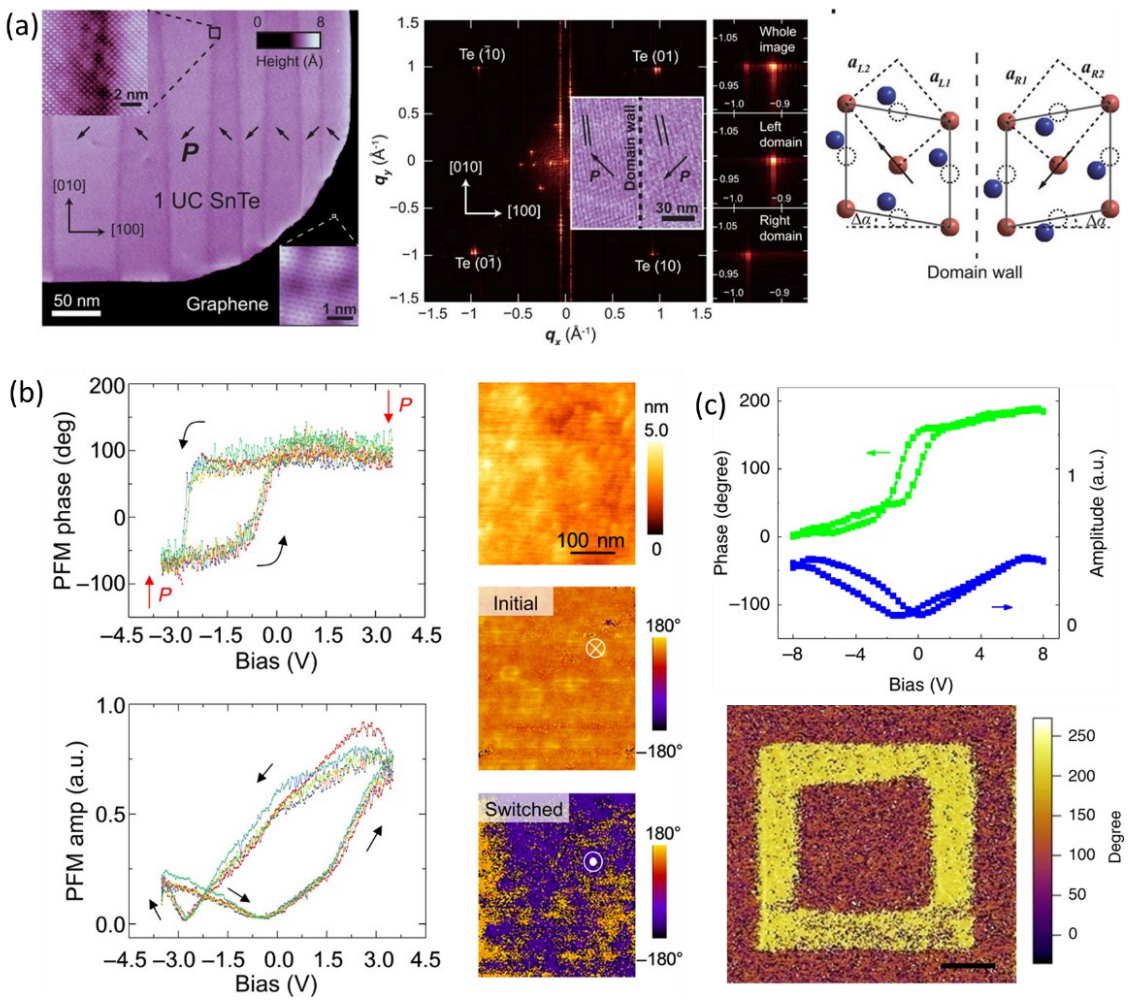


**Figure 1.5** Experimental evidences of ferroelectricity in various 2D vdW materials (a) SnTe[65], (b) $WTe_2$[66], and (c) d1*T*-$MoTe_2$[67].

Accordingly, considerable studies have been participated into searching new 2D layered materials that exhibit strong out-of-plane piezoelectricity. Thus far, vertical piezoelectricity has been reported in several 2D materials, including buckled group-III-V monolayers ($d_{31}$: 0.02 to 0.6 pm $V^{-1}$), Janus group-III chalcogenide monolayers ($d_{31}$: 0.07-0.46 pm $V^{-1}$), α-$In_2Se_3$ ($d_{33}$: 0.34-5.6 pm $V^{-1}$), $SnS_2$ ($d_{33}$: 2.2 to 5 pm $V^{-1}$), and 3R $MoS_2$ (0.7-1.5 pm $V^{-1}$)[55,64,68-72]. While the discovery of these novel 2D materials with

out-of-plane piezoelectricity is promising for technology development, their piezoelectric coefficients are still rather low compared to traditional out-of-plane piezoelectric materials.

**Table 1** A summary of the critical thickness and polarization value of several experimentally verified 2D vdW ferroelectric materials.

| **Material** | **Polarization direction** | **Critical thickness (nm)** | **Polarization value (μC cm$^{-2}$)** | **Ref. #** |
|---|---|---|---|---|
| SnTe | In-plane | 0.63 | — | 64 |
| SnS | In-plane | 0.58 | 26 | 79 |
| $BA_2PbCl_4$ | In-plane | 1.7 | 4 | 78 |
| *d*1*T*-$MoTe_2$ | Out-of-plane | 0.8 | — | 80 |
| $WTe_2$ | Out-of-plane | 1.4 | 0.2 pC m$^{-1}$ | 66 |
| α-$In_2Se_3$ | In-plane and out-of-plane | 2H: 1.2<br>3R: 3 | 2.14 | 82, 83 |
| $CuInP_2S_6$ | Out-of-plane | 4 | 4 | 65 |
| $CuCrP_2S_6$ | Out-of-plane | — | — | 96 |
| Rhombohedral TMDs | Out-of-plane | bilayer | ~2.0 pC m$^{-1}$ | 88 |
| $MoS_2/WS_2$ | Out-of-plane | bilayer | 1.45 pC m$^{-1}$ | 89 |
| Twisted h-BN | Out-of-plane | bilayer | 1.88 pC m$^{-1}$ | 84 |
| — : not reported | | | | |

In recent years, the possibility of realizing intrinsic ferroelectricity in 2D layered materials has been extensively investigated through theoretical predictions. Several potential ferroelectric materials have been identified including group IV chalcogenide monolayers (such as SnS, SnSe, GeS, and GeSe)[73], distorted 1*T*-phase TMDs[11,74], elemental group V monolayers[75], $III_2$–$V_3$ compounds ($In_2Se_3$)[76], and metal thiophosphates (such as $AgBiP_2Se_6$ and $CuInP_2S_6$)[77,78], while many of these 2D materials have been shown to maintain robust ferroelectricity at room temperature, even in atomically thin thickness. Ferroelectricity in 2D materials can be classified based on the direction of the polarization field along in-plane (parallel to surface) and out-of-plane (perpendicular to surface) directions. Experimentally, stable room-temperature in-plane ferroelectricity has been disceovered in ultrathin SnTe, SnS, $BA_2PbCl_4$, and so on[65,79,80]. For instance, one unit-cell thick 2D SnTe can still retain ferroelectricity at around 270 K, and 2-4 unit-cell thick SnTe films can maintain ferroelectric effect at room temperature[65]. The advantage of in-plane ferroelectricity is that the materials can retain their ferroelectric properties even in the ultrathin limit, without being affected by the longitudinal depolarization field. However, the polarization along in-plane direction also largely limits their potential for efficient device applications. Out-of-plane spontaneous polarization was experimentally observed in ultrathin vdW layers such as $WTe_2$, $CuInP_2S_6$, and distorted 1*T*-$MoTe_2$[66,67,81], and intercorrelated in-plane and out-

of-plane ferroelectricity was identified in α-$In_2Se_3$[23,82-84]. Vertical ferroelectricity is more beneficial for designing nanoelectronic devices, but the polarization strength usually declines with decreasing thickness due to the depolarization field effect. On the other hand, 2D materials have been anticipated to exhibit novel physical and chemical properties, such as superconductivity and Moiré pattern, which are not observed in their bulk counterpart with atomically thin sheet-like structures[85,86]. In the 2D system, a polarization switching process differs from the conventional ferroelectric mechanism of ionic displacement, known as sliding ferroelectricity, has been proposed and verified experimentally. The out-of-plane dipoles originate from the interlayer asymmetric charge distribution, and the reversal of polarization direction is induced by a relative shift between adjacent layers causing the redistribution of charges. Sliding ferroelectricity was first discovered in metallic TMDs $WTe_2$[66], and then explored in more 2D materials such as γ-InSe[87], artificially twisted h-BN bilayers and twisted TMDs bilayers[85,88], untwisted $MoS_2/WS_2$ heterostructures[89], and 3R $MoS_2$[90]. Several 2D vdW ferroelectric materials currently reported with experimental evidence are summarized in Table 1.

## 1.3 Metal thiophosphate materials

The vdW layered metal thiophosphate materials, with the general structure of

$ABP_2X_6$ (where A/B can be Cu, Ag, In, Cr, etc. and X can be S/Se), are recently attracting a growing attention as they can offer a stable and flexible framework that allows for intentional incorporation of various transitional metals, enabling the design of structures with desired functionalities suitable for advance device fabrications[91]. Particularly, 2D $CuInP_2S_6$ (CIPS) has been widely investigated to possess room-temperature out-of-plane ferroelectricity and ion conductivity down to an ultrathin thickness of 4 nm[92]. Theoretical and experimental studies have revealed the origin of the negative out-of-plane piezoelectricity in CIPS which is rarely identified in the piezoelectric family[93]. Quantitative measurements indicate that the piezoelectric and electrostriction coefficients of bulk CIPS are significantly higher than that of most intrinsic ultrathin layered piezoelectric materials. Analogous to CIPS, replacing the In with magnetic Cr cations makes $CrCuP_2S_6$ (CCPS) a potential candidate for achieving low-dimensional multiferroics[94]. The co-existence of antiferromagnetic and antiferroelectric orderings are shown below 32 K[95,96]. Above 190 K, CCPS is observed to possess a nonpolar antiferroelectric configuration, where the Cu ions are evenly distributed between the up and down sites within the sulfur framework. Meanwhile, recent study also suggested that ultrathin CCPS exhibits ferroelectric-like at room temperature[97].

## 1.4 Motivation and significance of the research

As information nanotechnology advances rapidly, there is an increasing demand for higher density and smaller scale electronic devices. This has led to a continuous reduction in the dimensions of functional materials. Nonetheless, the problem of poor CMOS compatibility and intrinsic size effect have seriously restricted the potential of conventional ferroelectric perovskite thin films in the semiconductor and nanoelectronic industries. Moreover, the Curie temperature and the polarization strength of traditional ferroelectric materials gradually declines as the film thickness is reduced to the 2D regime, further impeding their availability and suitability for modern nanoscale devices. Enormous efforts have been dedicated to addressing the effect of depolarization in traditional ferroelectrics and reducing the critical thickness below 10 nm. Nevertheless, selection of specific electrodes and/or substrates is still unavoidable to realize minimal lattice mismatch. In addition, complex fabrication processes are required to achieve high-quality thin films with few defects. These limitations hinder the promising applications of perovskite-based ferroelectrics in nanoscale electronic and other systems.

Significant progress has been made in the exploration of novel 2D layered materials and the development of deposition methods of 2D thin films. To date, a variety

of new 2D piezoelectric materials have been discovered and mostly only exhibit in-plane piezoelectricity. Amongst, several 2D in-plane piezoelectric materials exhibit layer-dependent piezoelectric properties in which their strength of the piezo-polarization declines with decreasing layer thickness and can only be identified in odd-layers. These limitations restrict their potential for incorporation into vertical nanoelectronic device architectures. Although out-of-plane piezoelectricity has been reported in numerous 2D vdW members, their piezoelectric response is weak compared to traditional piezoelectric materials. Therefore, the discovery of new 2D materials exhibiting strong piezoelectricity, particularly in the out-of-plane direction, help promote the development and implementation of efficient piezotronic nanodevices.

Recently, 2D metal thiophosphate materials have garnered high research attention especially after the widespread experimental achievements in understanding the room-temperature ferroelectricity in CIPS. The piezoelectric and electrostriction coefficients of bulk CIPS are higher than most intrinsic piezoelectric materials such as PVDF and PZT[93]. Despite the advancements in understanding the ferroelectric behavior of CIPS, the room-temperature piezoelectric characteristics of CIPS in the ultrathin limit have not been well examined and await further investigation. Moreover, the prospective applications in nanoelectronics exploiting their piezoelectricity are also lacking. Therefore, the potential of employing 2D CIPS in nanoscale piezoelectric devices and

systems remains to be fully realized.

On the other hand, pilot theoretical studies have suggested the existence of out-of-plane ferroelectricity in a variety of 2D materials, but the experimental discoveries of stable room-temperature 2D ferroelectricity in vdW layered materials are still relatively limited[65,67,69,92]. Prior study has reported the presence of ferroelectric behaviors in ultrathin CCPS layers at room temperature. However, there is a lack of a thorough investigation into the ferroelectricity of CCPS. Also, the origin of the observed ferroelectric characteristics has not been comprehensively understood. The underlying mechanism contributing to the apparent ferroelectric behaviors in the ultrathin CCPS layers at room temperature remains to be elucidated through further studies.

## 1.5 Structure of the thesis

The thesis chapters are arranged as follows:

**Chapter 1**: Introduction. This chapter first presents a general background of 2D vdW layered materials with their unique characteristics and possible applications. Then, the recent advances and challenges in ultrathin traditional piezoelectric and ferroelectric materials are discussed, and the emerging 2D layered piezoelectric and ferroelectric materials are described. Next, the metal thiophosphate material is introduced. Finally, the significance of research is illustrated to denote the motivation and objectives of the

thesis, and the structure of this thesis is presented.

**Chapter 2**: Experimental details. In this chapter, the various experimental techniques employed in the research activities of the thesis are described. First, the strategies utilized to prepare the 2D ultrathin layers are described. Then, different techniques conducted to characterize the crystal structure and properties of materials are demonstrated. Finally, details of the theoretical calculations in this thesis are described.

**Chapter 3**: Strong piezoelectricity in 2D layered CIPS for piezoelectric nanogenerators. In this chapter, the strength and thickness dependence of the out-of-plane piezoelectricity in 2D CIPS nanosheets are comprehensively characterized and analyzed. Then, the piezotronic effect is revealed, and vertical piezoelectric nanogenerators based on piezoelectric CIPS nanosheets are fabricated on rigid substrates and their device performance is characterized.

**Chapter 4**: Direct observation of intrinsic room-temperature out-of-plane ferroelectricity in vdW layered CCPS nanoflakes. This chapter characterizes the material properties and vertical ferroelectricity in ultrathin CCPS flakes. Then, the origin and underlying mechanism of the intrinsic ferroelectricity in 2D CCPS at room temperature are investigated.

**Chapter 5**: Nanoelectronic devices based on 2D ferroelectric CCPS. In this

chapter, various device structures incorporating the ferroelectric properties of CCPS nanoflakes are constructed and demonstrated for non-volatile memory applications.

**Chapter 6**: Conclusions and future prospects. This chapter summarizes the findings in this thesis. Then, the future prospects of 2D layered piezoelectric and ferroelectric metal thiophosphates are proposed.

# Chapter 2 Experimental Details

This chapter presents the experimental techniques applied in this work. Ultrathin $CuInP_2S_6$ (CIPS) and $CrCuP_2S_6$ (CCPS) nanosheets were prepared by mechanical exfoliation. The optical characteristics of the two-dimensional (2D) materials were studied using optical microscopy and Raman spectroscopy. Crystal structures and chemical compositions were characterized through second harmonic imaging microcopy (SHIM), X-ray diffraction (XRD), (scanning) transmission electron microscopy ((S)TEM), and energy dispersive X-ray spectroscopy (EDX). The electrical performances were characterized by probe station with semiconductor analyzer and conductive atomic force microscopy (C-AFM). The surface morphography of the materials was studied using atomic force microscopy (AFM). The piezoelectric and ferroelectric responses, and ferroelectric domains at the nanoscale were observed and analyzed by piezoelectric force microscopy (PFM). Surface potential and band structure analysis were conducted by ultraviolet photoelectron spectroscopy (UPS) and scanning Kelvin probe microscopy (SKPM).

## 2.1 Preparation of ultrathin materials

Mechanical exfoliation is a commonly utilized top-down approach for preparing

ultrathin 2D materials from their bulk crystal, as schematically described in Figure 2.1. In this process, a sticky tape or polymer film is adopted as the medium to apply shear force to the van der Waals (vdW) layered materials, breaking the weak vdW interactions between adjacant layers without destroying the strong interlayer covalent bonds. The peeling of thinner flakes from the bulk crystal onto the tape surface is followed by repeated exfoliation between the two surfaces several times to obtain atomically thin layers, which can then be attached to an arbitrary substrate. Since no chemical reaction occurs during the entire exfoliation process, the prepared ultrathin materials own the advantages of a clean surface and high crystallinity, which are beneficial to the fundamental research of material properties.

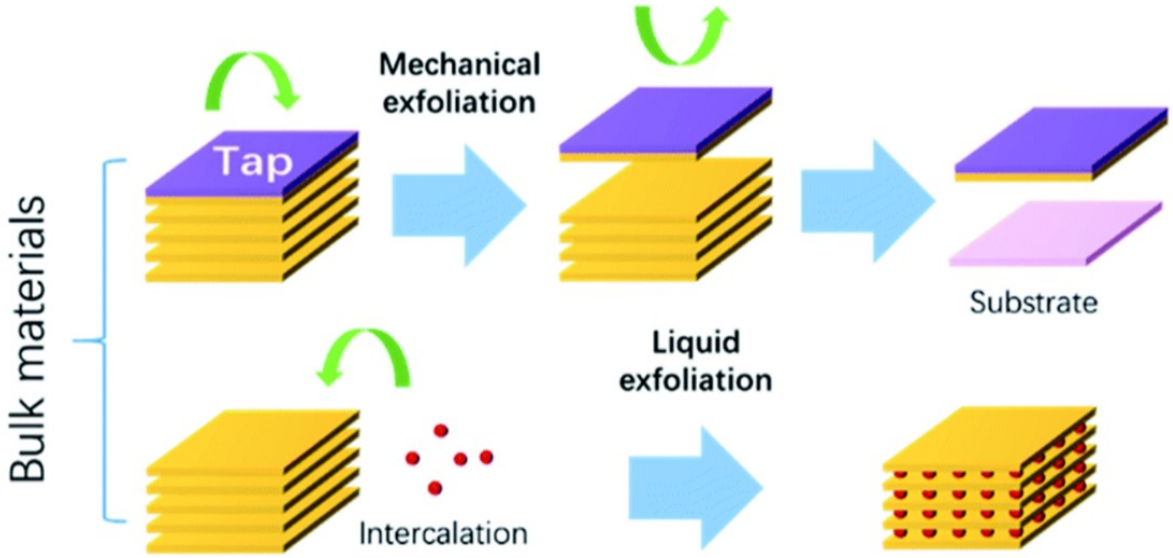


**Figure 2.1** Te preparation of 2D materials through mechanical and liquid-phase exfoliation strategies[98].

Besides the facile utilization of sticky surfaces, liquid-phase exfoliation is also a typical and well-developed technique to prepare ultrathin 2D nanosheets. The yield of the exfoliated 2D flakes greatly depends on the type of solvents applied to the materials. By sonication in a certain solvent, the bulk vdW layered crystal can be efficiently exfoliated into a 2D form. In this process, ultrasonic waves aid to achieve delamination of bulk crystal by breaking the weak vdW interactions between layers, while strong interlayer covalent bonds are not affected. Experimental findings and theoretical calculations have revealed that energy matching of surface tension between vdW layered materials and solvents helps reduce the potential energy barrier between adjacent layers and affects the exfoliation efficiency. Through appropriate energy matching, layered materials can efficiently adsorb solvent molecules into the interlayer spacing, in which the insertion of solvent molecules will expand the spacing, reduce interlayer vdW interactions, and further delaminate the materials into ultrathin nanosheets. Furthermore, the solvent is crucial for subsequent stabilization and preventing the restacking and aggregation of the exfoliated nanosheets. However, water, a frequently used solvent, is insufficient to effectively exfoliate most layered materials. During the ultrasonic treatment, stabilizers such as polymers and surfactants are mixed with organic solvents to improve the exfoliation efficiency. Consequently, various atomically thin 2D materials, including TMDs and BN, can be prepared from bulk

crystals using this method. The thickness and lateral dimensions of the exfoliated nanosheets can be controlled by regulating the ultrasonic treatment time, frequency, power, and the type of solvent utilized. After delamination, exfoliated sheets of different sizes and thicknesses can be selectively obtained through controlled centrifugation procedure. Liquid-phase exfoliation is a comparatively cost-effective, simple, and fast approach for scalable and high-yield preparation of 2D materials feasible for commercial applications. Nevertheless, the lateral dimensions of the exfoliated nanosheets fabricated through this approach are usually small, and the yield of mono- and few-layer nanosheets is rather low. Also, stabilizer may remain on the exfoliated 2D nanosheets, which is undesirable for material characterization and device applications.

## 2.2 Material characterization

### 2.2.1 Optical microscopy

Optical microscopy serves as a straightforward and facile method for initially examining the surface morphology, thickness, and phase of 2D materials. This technique primarily relies on a series of lenses that direct light onto the sample's surface and receive the light reflected back to form images at various magnifications in real time. With light illumination under an optical microscope, different materials interface

with light differently, leading to optical contrast, and images are generated by collecting this reflected light, allowing for the distinction between 2D materials and their substrates. Also, the optical transparency of 2D materials changes with thickness, enabling the determination of the thickness contrast of 2D nanoflakes through optical microscopy. For 2D materials that exhibit significant variations in optical path and transparency, the color and intensity of the reflected light can be quantitatively analyzed to evaluate the thickness of the nanoflakes.

### 2.2.2 Second-harmonic generation spectroscopy

Second-harmonic imaging microscopy (SHIM) is an efficient, fast, and non-invasive optical approach that utilizes the nonlinear optical phenomenon known as second-harmonic generation (SHG). SHG occurs exclusively in materials that lack a center of symmetry. When non-centrosymmetric materials are exposed to light, pairs of photons at the same frequency (ω) interact with the material and “merge” to produce a new photon with doubled frequency (2ω) (halved wavelength) of the original incident photons. In SHIM, a high-intensity light source with the frequency of 2ω is employed to stimulate coherent SHG signals. The emitted photons near the frequency ω are then captured to create second-harmonic images. In this study, the symmetry of the 2D vdW layered materials were analyzed using a Leica TCS SP8 MP confocal microscope.

### 2.2.3 Raman spectroscopy

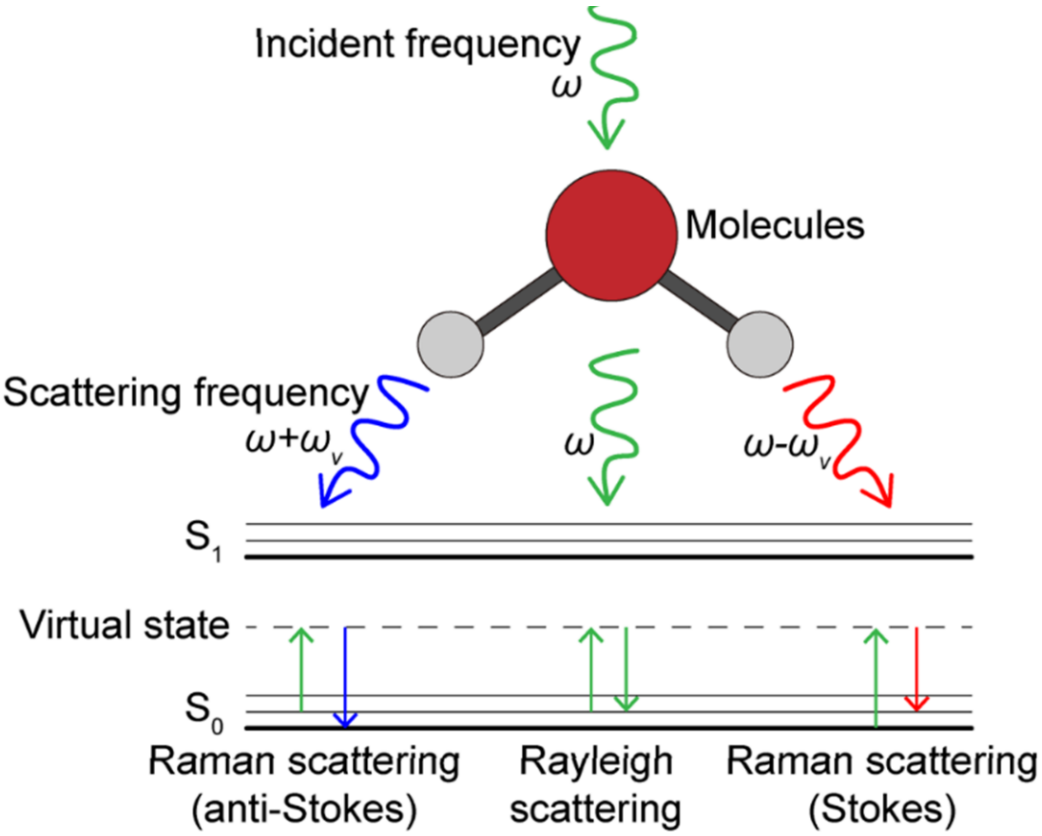


**Figure 2.2** Working mechanism of Raman spectroscopy[99].

Raman spectroscopy is a widely utilized, non-invasive technique that leverages light to determine the structure, phase, and crystallinity of materials. The core principle of Raman spectroscopy is based on the interaction between laser light and the molecules within the material being studied, as depicted in Figure 2.2. It captures the vibrational modes of the material for analysis. During the process, a laser beam is directed onto the sample and interacts with the molecular structure. Molecules initially in their ground state absorb the photon energy and promote to a higher virtual energy state.

Subsequently, the molecules return to a lower energy state and photons are emitted. If the molecules return to their initial ground state, the energy of the emitted photons are consistent to the incident photons, and this phenomenon is known as Rayleigh elastic scattering. Since the energy of incident and emitted photons are identical, Rayleigh scattering does not provide insightful information on the crystal structures. If the molecules turn into a lower energy state that differs from the original one, the photons emitted will exist a different energy than the incident photons. This results in Stokes Raman scattering and anti-Stokes Raman scattering (inelastic scattering) and the inelastic scattered photons exhibit a shift in wavelength due to the energy difference. Anti-Stokes Raman scattering occurs when molecules are initially in an excited state, hence the possibility for Stokes Raman scattering to occur is much greater than that for anti-Stokes Raman scattering. Therefore, the Raman spectrum is predominantly based on the more intense Stokes Raman scattering signals. Raman spectroscopy offers a distinctive fingerprint for identifying various materials, providing insights into their crystal structures and phases.

In this study, the Raman spectra were obtained using a Witec Alpha 300 R confocal Raman system equipped with a 532 nm excitation laser source, which has a penetration depth of several hundred nanometers. This confocal Raman system not only allows for single-point measurements but also facilitates large-scale Raman mapping at selected

positions on the materials.

### 2.2.4 Ultraviolet photoelectron spectroscopy

Photoelectron spectroscopy is a powerful tool used to study the electronic structure by characterizing the energy of photoelectrons that are emitted from sample surfaces due to the photoelectric effect. The excitation sources for this technique can be either X-ray or ultraviolet (UV) light, depending on the measurement purposes. For photoelectron spectroscopy, conducting measurements in a high vacuum environment is necessary to prevent interactions between the photoelectrons and air molecules.

Ultraviolet photoelectron spectroscopy (UPS) is a useful technique utilizing UV photons to measure the ionization energies of the valence electrons in the outermost shell, in which information about the band structure and the work function of a metallic or semiconducting surface can be acquired. UPS exhibits a low penetration depth of approximately 2 to 3 nm and the measurement is highly surface sensitive. In principle, when UV light is incident on the sample surface, UV photons are absorbed by the electrons in the valence band, leading to the emission of photoelectrons. The emitted photoelectrons are collected and their kinetic energy and counts are analyzed which contributed to an observed UPS spectrum. The UPS measurements in this study are conducted by a Nexsa G2 Surface Analysis System.

### 2.2.5 X-ray diffraction

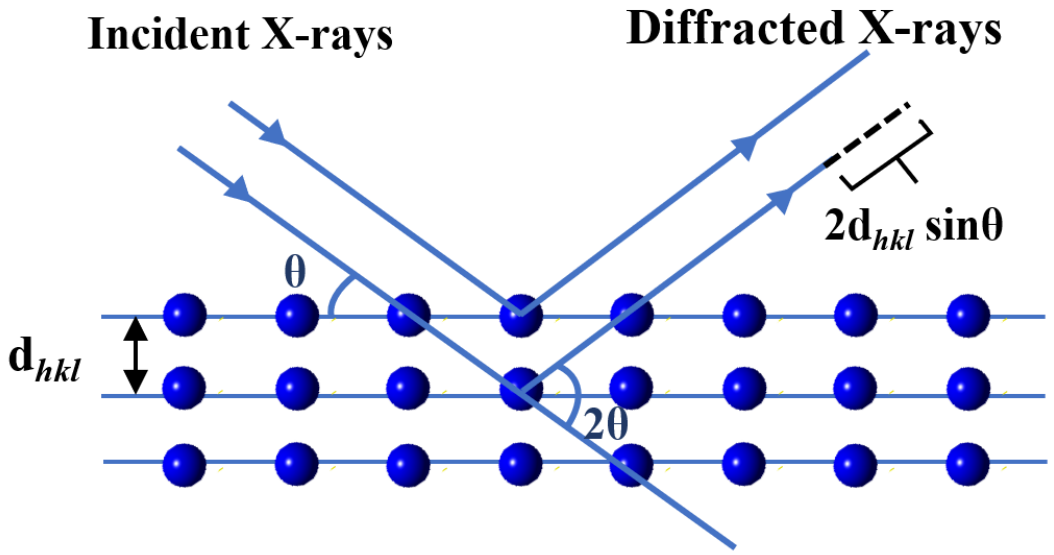


**Figure 2.3** Schematic of operating principle of X-ray diffraction.

X-ray diffraction (XRD) is an essential equipment for rapidly characterizing the crystallinity of materials in a non-destructive manner. The working mechanism of XRD is schematically depicted in Figure 2.3, based on the constructive interference of the monochromatic X-ray incident on the sample surface. The interaction of the incident monochromatic X-rays on the investigated samples produces constructive interferences only when the condition of Bragg's Law is satisfied: $2d_{hkl}\sin\theta = n\lambda$, where $\theta$ refers to diffraction angle, $\lambda$ refers to wavelength of the incident X-ray, $h$, $k$, and $l$ are the Miller indices, and $d_{hkl}$ is the distance between adjacent lattice planes of the analyzed samples. The diffracted X-rays are collected and analyzed, then a diffraction pattern can be constructed using the number of counts and diffraction angles. The diffraction spectrum

can provide various structural information towards the studied samples such as crystallinity, lattice structure, phase, orientation, and lattice spacing. The XRD results in this work were acquired by a Rigaku Smartlab 9 kW X-ray diffractometer equipped with a 2D detector and X-ray source from Cu $K\alpha$ radiation ($\lambda = 0.154$ nm).

### 2.2.6 Scanning transmission electron microscopy

Scanning transmission electron microscopy (STEM) is a useful and imperative technique for studying materials at an atomic scale. In general, the TEM equipment is consisting of an electron gun chamber, sample chamber, and projection chamber, and are always maintained at ultrahigh vacuum environment. Instead of photons, STEM employs high-energy electrons to construct images with a much higher resolution than optical microscopy since the de Broglie wavelength of electron is much shorter than the wavelength of light. In STEM acquisition, a focused electron beam is directed on the sample and the electrons transmitted through the sample are collected and analyzed. To allow electron to transmit through, the thickness of the sample is necessarily prepared to approximately less than 100 nm.

TEM can be operated in either the imaging mode or the diffraction mode. For real-space imaging, there are several contrast mechanisms to generate images, such as diffraction contrast, mass-thickness contrast, and phase-contrast imaging. A variety of

information about the inspected sample, including crystallinity, lattice structure, crystal orientation, thickness differences, and chemical composition, can be obtained through the different imaging modes. By adjusting the lens inside TEM, the working mode can be changed to diffraction mode to measure the diffraction pattern of the observed samples. The diffraction patterns produced by single-crystalline, polycrystalline, and amorphous materials are different and can be used to determine the crystallinity.

In this study, high-resolution transmission electron microscopy (HRTEM) images and selected area electron diffraction (SAED) patterns were acquired using an Orius SC1000 charge-coupled device (CCD) camera in a JEOL JEM-2100F electron microscope operating at an accelerating voltage of 200 kV. Atomically resolved STEM images were captured with an aberration-corrected (S)TEM (Thermo Fisher Spectra 300) at an accelerating voltage of 300 kV. The instrument was set with a convergence semi-angle of 14 mrad and the segmented detectors collected electrons over an angular range of 5 to 21 mrad. Prior to capturing images, the electron probe was optimized using a spherical aberration and DCOR corrector, calibrated with a standard gold sample. The imaging process involved a dwell time of 8 μs and a probe current of 16 pA.

### 2.2.7 Energy dispersive X-ray spectroscopy

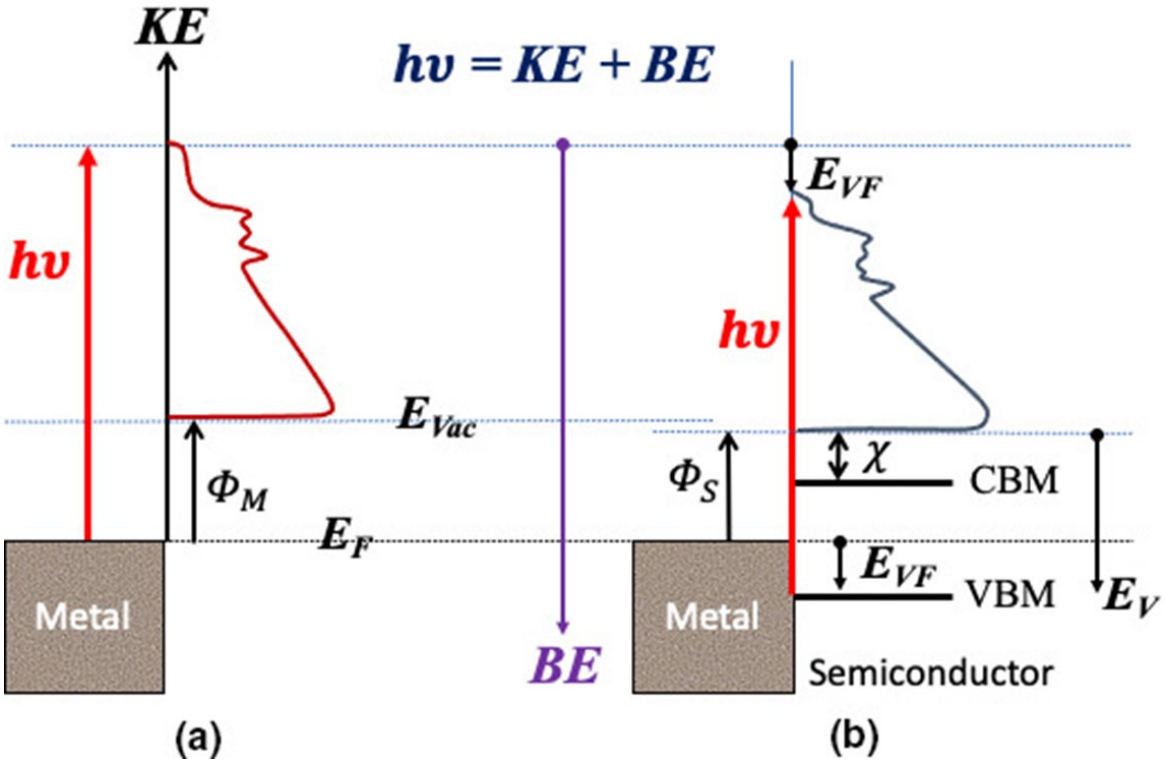


**Figure 2.4** Schematic of the working principle of UPS investigation on (a) metallic and (b) semiconducting materials.[100]

Energy dispersive X-ray spectroscopy (EDX) is a method employed for the chemical analysis of materials at a microscopic level, and it is commonly integrated with electron microscopy. An energy dispersive X-ray detector is installed within the electron microscope to capture the characteristic X-rays that are emitted from the studied material when exposed to an electron beam, as illustrated in Figure 2.4. This process allows for the determination of the elemental composition of the sample under

investigation. As the electron beam strikes the sample, inner shell electrons are kicked out which are referred to as secondary electrons. These vacancies are then filled by electrons from the higher energy outer shells. The transition of electrons from higher to lower energy levels results in the emission of high-energy X-ray photons, which are then detected by the X-ray detector. Every element exhibits a distinct electronic structure, leading to a unique set of characteristic X-ray peaks. Consequently, EDX has been a powerful tool for identifying the element composition of the inspected sample.

### 2.2.8 Probe station with a semiconductor analyzer

The probe station system is a typical system for evaluating the electrical properties of different devices and is basically consists of an optical microscope, a probe station, and a semiconductor parameter analyzer. During testing, the devices are placed on the probe station, and tungsten probes are used to make contact with the device electrodes, connecting the devices to analyzer. The integrated optical microscope in the probe station aids in identifying and locating the device electrodes. The devices in this study were characterized using a probe station (Lakeshore) equipped with a Keithley 4200-SCS semiconductor parameter analyzer which measures the current responses with an ultrahigh current resolution at femto ampere scale.

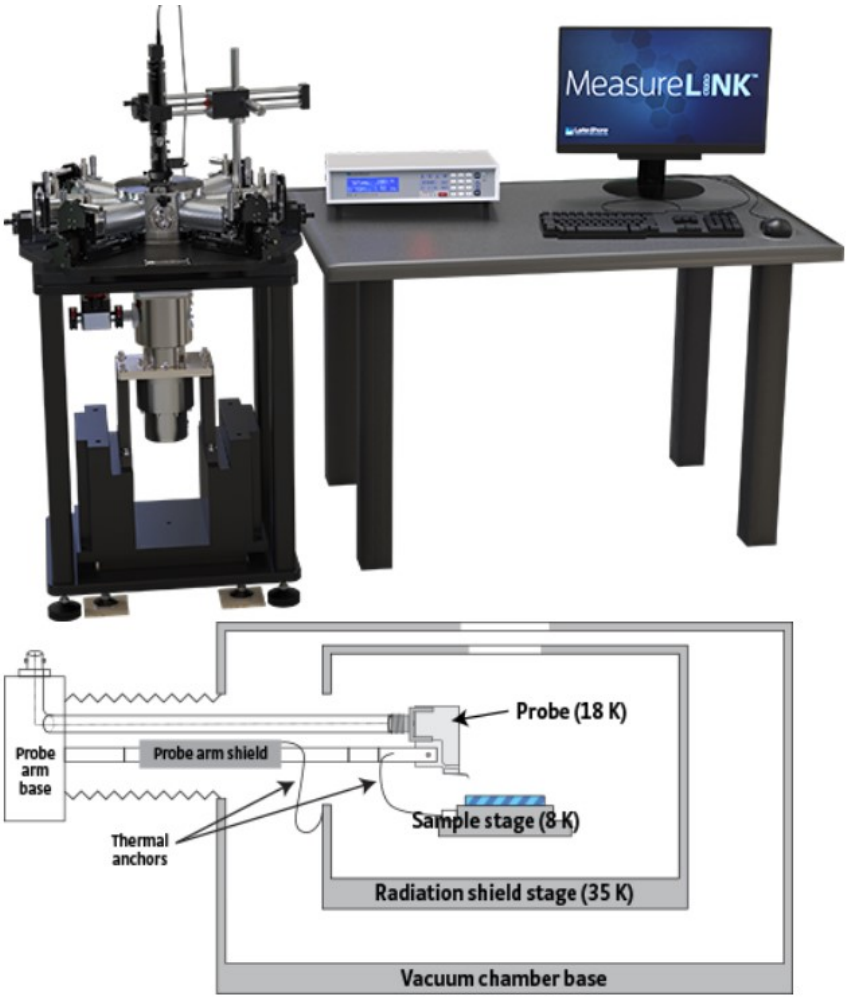


**Figure 2.5** Setup of the probe station system employed in this work.

## 2.2.9 Scanning probe microscopy

Scanning probe microscopy (SPM) encompasses a series of sophisticated instruments designed to analyze various material properties and features at the atomic level. The operating modes include atomic force microscopy (AFM), kelvin probe force microscopy (KPFM), piezoelectric force microscopy (PFM) , conductive atomic force microscopy (C-AFM), and so on. The functionality of SPM technologies hinges on detecting and analyzing the various interaction forces that occur between a nano-sized

probe and the surface of the material under investigation.

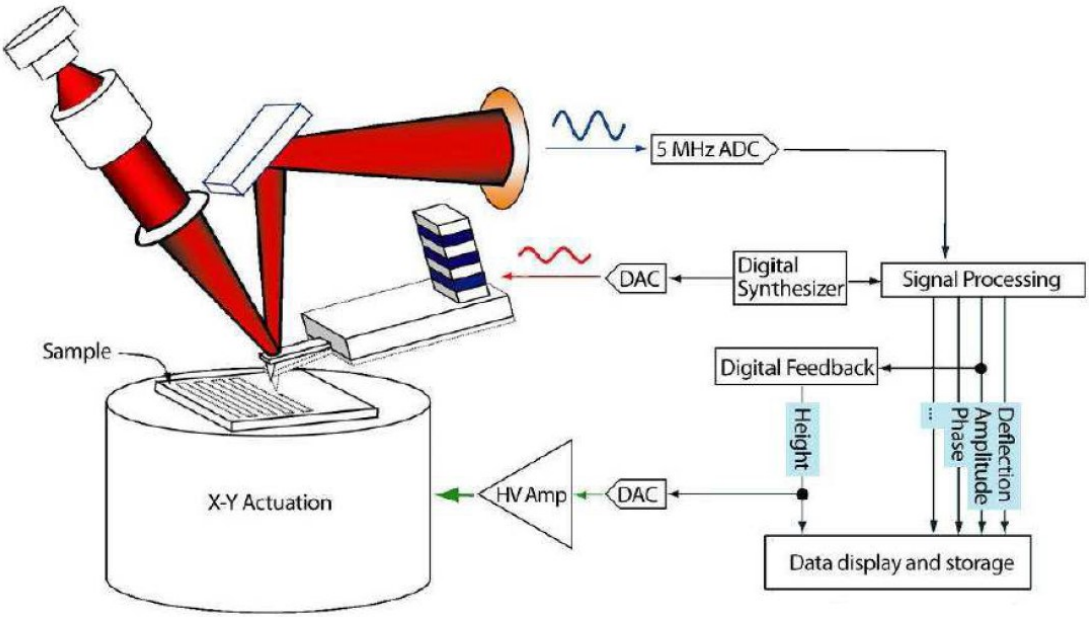


**Figure 2.6** Schematic diagram of the operation principle of the tapping imaging mode in scanning probe microscopy.

Among the variety of SPM operation modes, AFM is the most commonly employed mode for assessing the topography, height, surface roughness, and phase contrast of the materials. The AFM utilizes a nanoscale physical probe that scans across the sample's surface in close proximity to generate an image. The AFM probe is connected to a cantilever that deflects in response to the interaction forces as the tip reaches nears the surface. The degree of cantilever deflection is monitored by a laser beam aimed at the cantilever, while the reflected beam is collected by a photodiode to record the changing position of the laser beam. AFM can be operated in several modes,

including contact, tapping, and non-contact modes. Contact mode utilizes the repulsive force between the probe and the sample surface at a very close distance and provides the highest accuracy since repulsive force is sensitive to distance. However, maintaining the tip in contact can easily destroy the sample surface. Non-contact mode records the attractive force and the AFM probe is kept at a certain distance above the sample surface. This imaging mode is non-destructive but the image resolution is the least accurate among the different operating modes. In this study, tapping mode is mostly adopted to capture high-resolution images without damaging the investigated sample. The operating principle of tapping mode is shown in Figure 2.6. During measurements, the AFM tip is oscillating near its resonance frequency by a piezoelectric actuator in the cantilever and the oscillatory motion of the cantilever is detected by a photodiode. The electronic components inside the controller record the resultant amplitude and phase of the oscillating signal with respect to the initial driving signal.

PFM is an efficient and direct tool to examine the ferroelectric domains in ultrathin ferroelectric materials and reveals the existence of ferroelectricity in 2D ferroelectric thin films. Generally, a sharp conductive tip is utilized to scan over the sample surface under contact mode. An AC voltage is applied to the sharp tip to induce a strain to the surface of a piezoelectric material, resulting in periodic deflection of the cantilever by

the inverse piezoelectric effect. The inverse piezoelectric effect shall induce changes the amplitude of the driving signal, but the piezo-induced signals can be very weak with just a few picometers per volt. Thus, a frequency near the contact resonance of the conductive probe and the sample surface is used for amplifying the weak piezo signals. When ferroelectric materials are examined, the spontaneous polarization will induce a change in the phase of the signal depending on the orientation of the ferroelectric polarization and the ferroelectric domain structures can be observed.

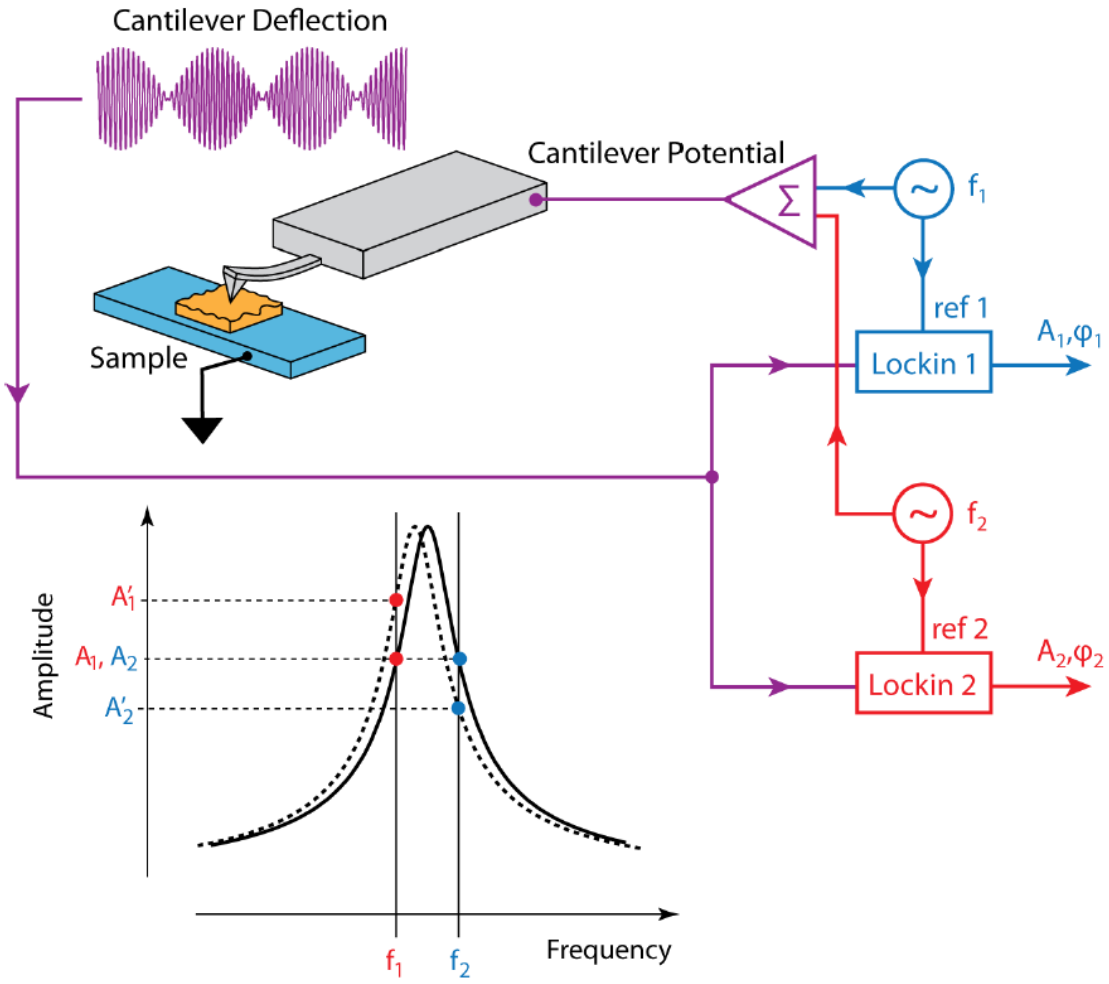


**Figure 2.7** Setup of the DART- PFM operating mode.

In this study, the PFM measurements were acquired through a scanning probe microscopy (Asylum MFP-3D Infinity) in the dual AC Resonance-tracking (DART) mode (Figure 2.7). By tracking the frequencies on two sides of the contact resonance frequency peak, the driving frequency can be efficiently maintained near the contact resonance frequency, and the response signals can be significantly amplified. With the use of lock-in amplifiers, the amplitude and phase of the signal are measured simultaneously, and the topography, piezoelectric responses, and ferroelectric domains of the sample can be imaged at once.

### 2.2.10 Theoretical calculations

The charge density and electronic characteristics were calculated using CAmbridge Serial Total Energy Package (CASTEP) simulation code at a plane-wave energy cutoff of 700 eV[101]. Perdew-Burke-Ernzerhof (PBE) generalized gradient approximation (GGA) was used as the exchange-correlation functional, and a set of norm conserving pseudopotentials was adopted for the calculations[102]. The CASTEP algorithm was employed to optimize the cell, lattice parameters, and atomic coordinates of all metal thiophosphate conventional unit cells. The geometry optimization convergence energy tolerance and the Self-consistent field (SCF) for regulation of the electronic minimization technique was set to $1.0 \times 10^{-9}$ eV/ atom and $1.0 \times 10^{-9}$, respectively. Broyden-Fletcher-Goldfarb-Shanno (BFGS) approach was used, and a force and stress

convergence tolerance of 0.01 eV $Å^{-1}$ and 0.02 GPa were adopted for geometry optimization. Moreover, a 12×12×1 Monkhorst pack *k*-mesh sampling with a separation of 0.0023 $Å^{-1}$ was utilized to sample the Brillouin zone. The obtained simulation outcomes were visualized by the VESTA software[103].

# Chapter 3 Strong Piezoelectricity in 2D Layered CIPS for Piezoelectric Nanogenerators

## 3.1 Introduction

In the future nano era, two-dimensional (2D) van der Waals (vdW) layered materials exhibit great potential as multifunctional electronic materials owing to their outstanding characteristics, including superior mechanical flexibility and carrier mobility as compared to their bulk counterparts[8,104,105]. Many remarkable properties, including topological, photovoltaic, ferroelectric, piezoelectric, and superconducting features, have been realized in 2D layered materials through intensive theoretical and experimental investigations performed in recent years[3,23,24,27,67,106-108]. Particularly, 2D materials with piezoelectricity, that are commonly used in energy harvesters, actuators, sensors, are relatively rare. 2D piezoelectric materials are promising for use in nanoscale devices with high performance and low power consumption because of their atomically thin dimension and exceptional mechanical endurance under large strain. This has encouraged researchers to search for new low-dimensional piezoelectric materials with high electromechanical effects[15,51,54,61,64,68,109-113].

Intensive theoretical and experimental studies in recent decade have given rise to

the discovery of new members of the 2D piezoelectric family. While most of them only exhibit in-plane piezoelectricity, restricting their ability to be incorporated into vertical nanoelectronic device systems. Besides, many of the new vdW 2D piezoelectric materials show layer-dependent piezoelectric behaviors in which the strength of the piezo-polarization declines with layer thickness and piezoelectric effect can only be identified in odd-numbered layers. Consequently, considerable efforts have been invested into discovering new 2D layered materials exhibiting vertical piezoelectricity. However, 2D materials exhibiting out-of-plane piezoelectricity usually possess rather small piezoelectric coefficients in comparison to typical piezoelectric perovskite materials, hence the exploration of new 2D candidates with strong piezoelectric effect is highly desired for the development of efficient piezotronic nanodevices.

Recently, a layered metal thiophosphate material $CuInP_2S_6$ (CIPS) has been demonstrated to exhibit room-temperature ferroelectricity down to the ultrathin thickness of ~4 nm[92]. Later, You et al. indicated the origin of the negative out-of-plane piezoelectricity in CIPS which is rarely identified in the piezoelectric family[93]. Quantitative measurements revealed that the electrostriction and piezoelectric coefficients of CIPS were significantly higher when compared to that of the majority of intrinsic vdW layered piezoelectric materials currently reported. Nonetheless, the prospective applications in nanoelectronic field exploiting their piezoelectric

characteristics are lacking, and the piezoelectric strength of CIPS when approaching the 2D limit has still not been thoroughly understood. Through detailed piezoelectric force microscopy (PFM) analysis, the thickness-dependent high out-of-plane piezoelectric coefficient in 2D CIPS nanoflakes was quantitatively and systemically evaluated down to approximately 3.5 nm. Furthermore, the piezotronic effect in CIPS nanoflakes under compressive stresses is illustrated. 2D CIPS-based vertical piezoelectric nanogenerators were fabricated and their device performances towards practical piezoelectric applications were examined, which have not yet been addressed in previous studies. These findings indicate the strong piezoelectricity along vertical direction in 2D CIPS nanoflakes, highlighting its potential for use in nanoscale energy harvesting and piezotronic applications on rigid substrates including silicon wafers.

## 3.2 Structural characterization of CIPS nanoflakes

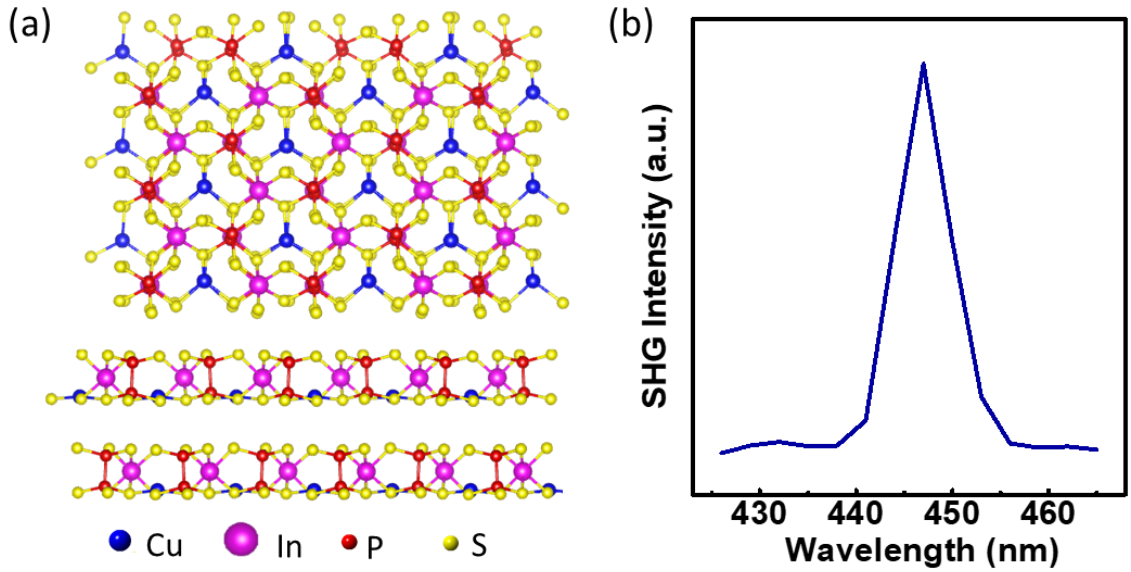


**Figure 3.1** (a) Illustration of the atomic configuration from both the top and side perspectives of the CIPS crystal with non-centrosymmetric nature. (b) SHG response from CIPS under ambient conditions, excited by a laser with a 900 nm wavelength.

In this study, bulk CIPS single crystal was purchased from the 2D Semiconductors USA company. To assess the crystal structure and quality of the CIPS crystal, techniques such as Raman spectroscopy, XRD, TEM, and EDX were adopted. For Raman analysis and PFM characterizations, ultrathin CIPS nanosheets were prepared through nanoflakes were prepared through typical mechanical exfoliation approach onto various substrates. For TEM investigation, CIPS nanoflakes were prepared by liquid-phase exfoliation approach onto TEM copper grid. In the liquid-phase exfoliation process, bulk CIPS single crystal was dispersed in a water and ethanol mixture of ratio

1:1 and treated with ultrasound operating at 120 W for 3 hours. After the sonication process, the dispersion was centrifuged at 1000 rpm for 5 minutes to extract the supernatant containing ultrathin CIPS nanoflakes. The collected supernatant was then centrifuged at 10000 rpm for another 5 minutes for precipitation purpose. Finally, the obtained CIPS nanosheets were drop-casted onto the copper grid by micropipette.

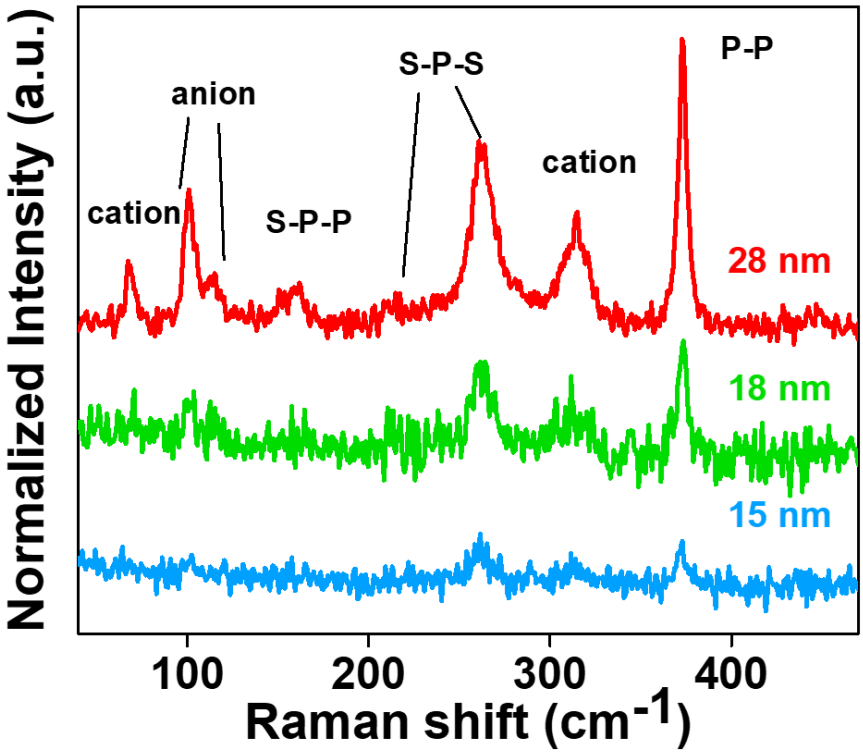


**Figure 3.2** Raman spectra for CIPS nanoflakes of varying thicknesses under ambient conditions, by utilizing a 532 nm laser for excitation.

The crystal structure of CIPS comprises octahedral voids formed by sulfur atoms, which are occupied by P-P pairs, In, and Cu atoms. Each CIPS layer is linked by weak vdW interactions. At room temperature, the CIPS exhibits a monoclinic *Cc* structure which is noncentrosymmetric and transforms into symmetric *C*2/*c* structure in

paraelectric phase above Curie temperature[114]. An illustration of the atomic arrangement of CIPS from the top and side views (Figure 3.1a) highlights its asymmetrical structure which contributes to the piezoelectric and ferroelectric properties in CIPS. SHG microscopy is conducted to examine the crystal's symmetry, where a dominant SHG signal from CIPS nanoflakes at the half wavelength of the excited laser can be detected (Figure 3.1b), indicating the absence of central symmetry.

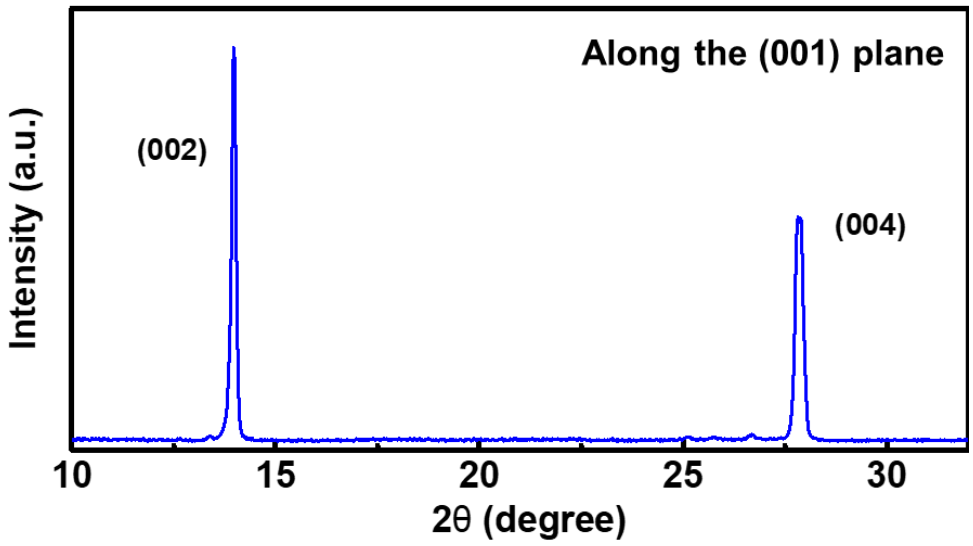


**Figure 3.3** XRD analysis of CIPS crystal measured under ambient conditions.

Raman spectroscopy was also utilized to identify the CIPS crystal phase at room temperature, and the Raman spectra of CIPS nanosheets of varying thicknesses from 15 to 28 nm are presented in Figure 3.2. The positions of the Raman peaks measured from the exfoliated CIPS samples are in good agreement with the vibrational modes of the bulk CIPS crystal in its ferroelectric phase as previously reported. The broad peaks in the 60 to 80 $cm^{-1}$ and 300 to 325 $cm^{-1}$ ranges are associated with the vibrations of the

$Cu^{+}$ and $In^{3+}$ cation oscillation modes, while that in the 90 to 120 $cm^{-1}$ range correspond to the stretching mode of the anion ($P_2S_6^{4-}$). The numerous peaks in 145 to 285 $cm^{-1}$ range are ascribed to the S-P-P and S-P-S stretching and the distinct sharp peak at 375 $cm^{-1}$ is attributed to the P-P stretching.

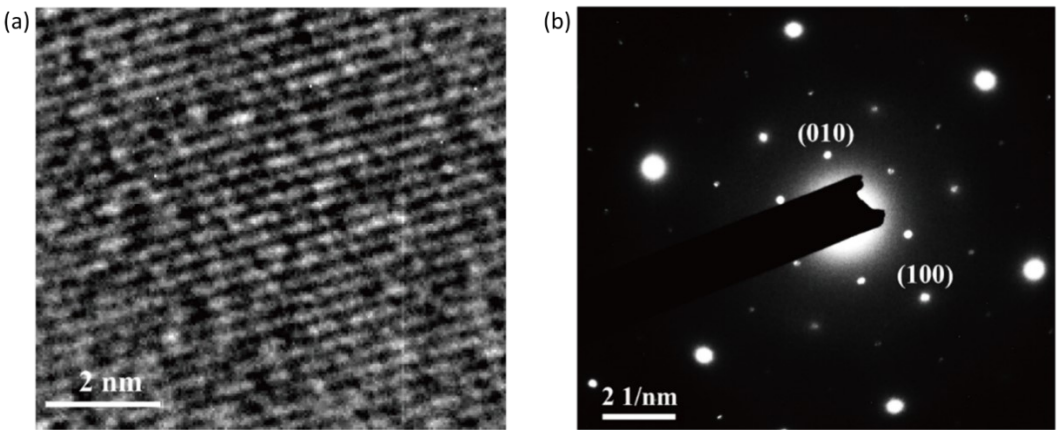


**Figure 3.4** (a) A high-resolution TEM image of a mechanical exfoliated CIPS flake, and (b) the associated SAED pattern.

The XRD pattern as shown in Figure 3.3 exhibits two distinct and sharp peaks at around 13.9° and 27.8°, correspond to the (002) and (004) planes, matching the reported ferroelectric phase CIPS. A high-resolution TEM image in Figure 3.4a shows the atomic-scale crystal structure of single-crystalline CIPS with uniform and periodic lattices. The corresponding SAED pattern in Figure 3.4b reveals the hexagonal structure, indicative of the high quality and single-crystalline nature of the CIPS crystal used in the study.

## 3.3 Piezoelectric and ferroelectric characterizations

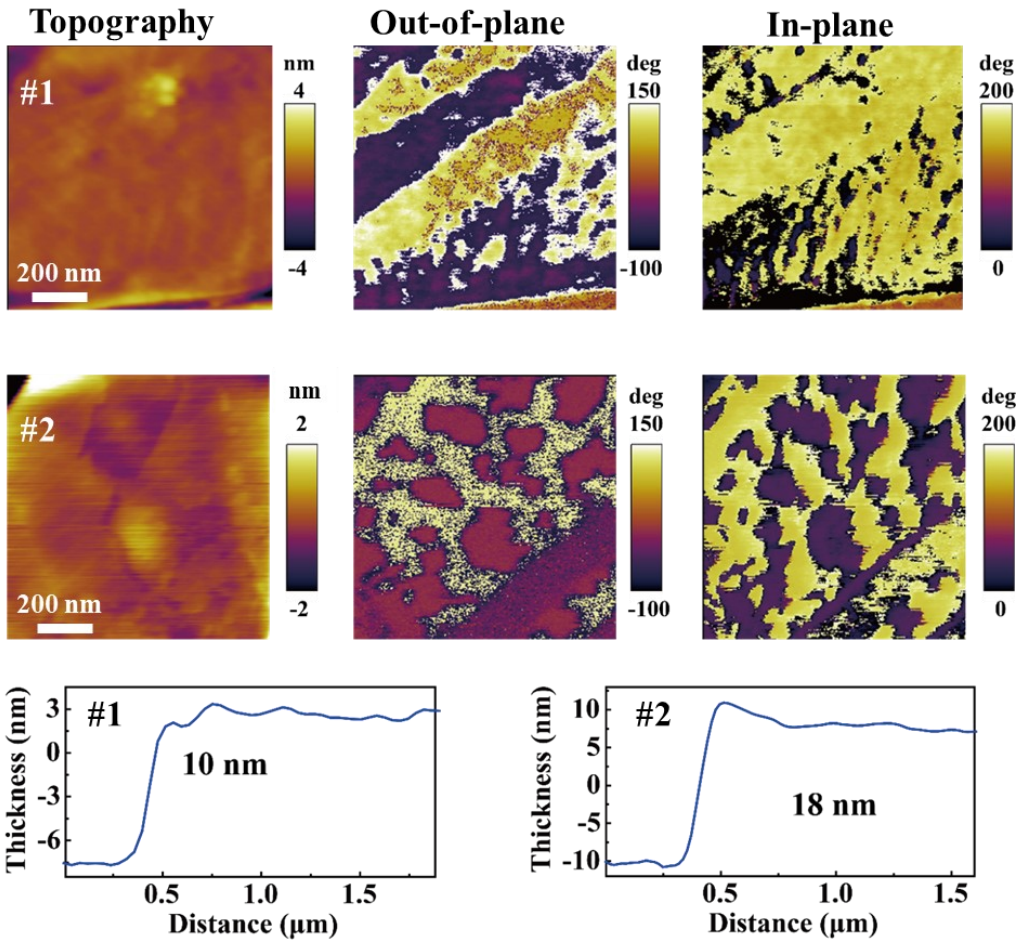


**Figure 3.5** Topography and PFM phase images showing clear ferroelectric domains in both out-of-plane and in-plane direction, and the height profiles of the characterized CIPS samples.

In order to investigate comprehensively the piezoelectric and ferroelectric properties in ultrathin CIPS nanosheets, detailed PFM analysis was conducted in the DART-PFM operation mode. For all PFM characterizations, a conductive tip coated with platinum/iridium (Pt/Ir) with a spring constant of 2.8 $Nm^{-1}$ was employed. Ultrathin CIPS samples were exfoliated onto a conductive Pt substrate and identified

under optical microscopy before PFM measurements. An AC voltage ranging from 1 to 4 V was applied while carrying out the ferroelectric and piezoelectric assessments.

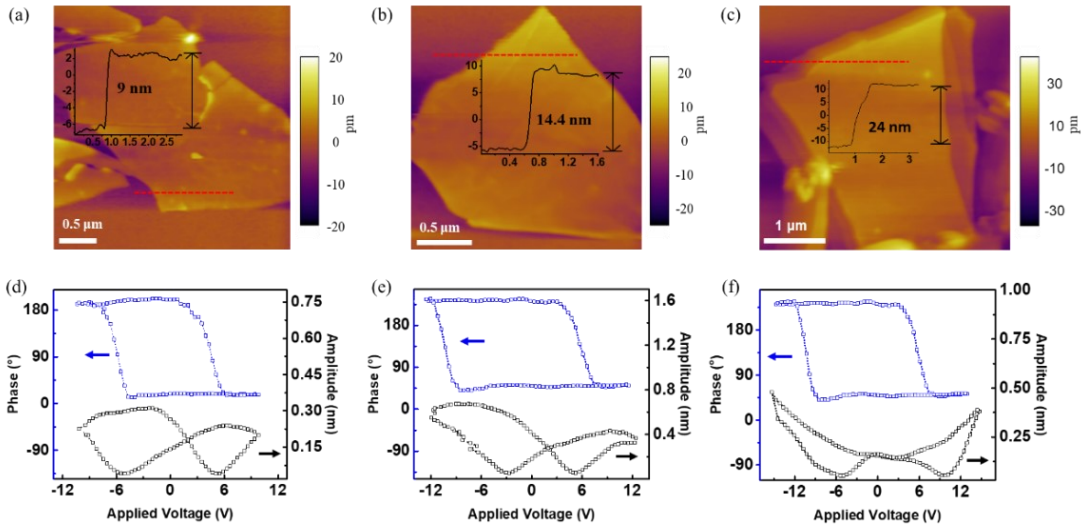


**Figure 3.6** (a)-(c) Images depicting the surface topography and height profiles. (d)-(f) The respective out-of-plane ferroelectric hysteresis loops for CIPS nanoflakes of varying thicknesses at 9 nm, 14.4 nm, and 24 nm, respectively.

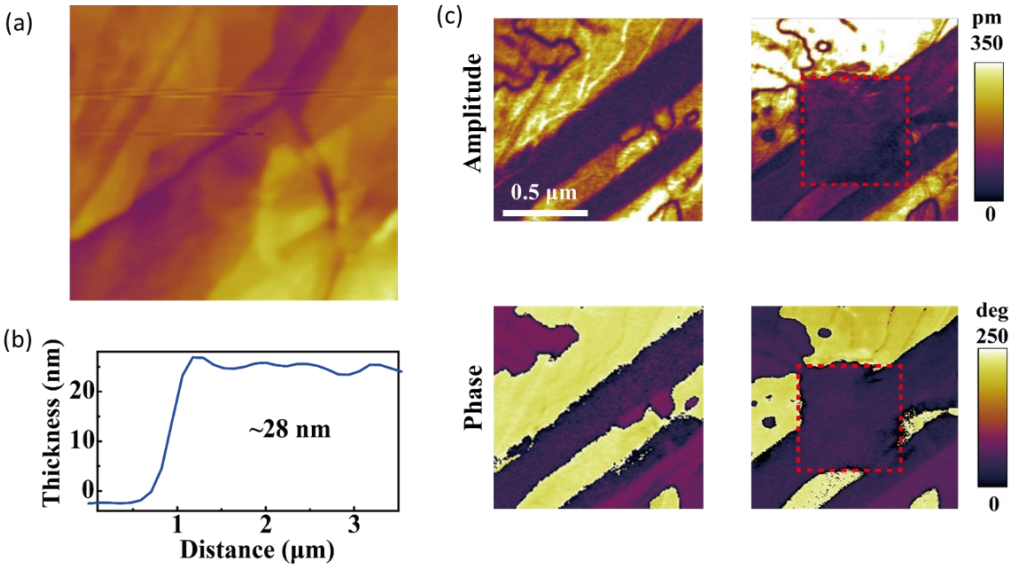


**Figure 3.7** (a) Morphography and (b) height profile of a 28 nm CIPS nanoflake. (c) PFM amplitude and phase images before and after domain modification with box pattern.

Figure 3.5 demonstrates the in-plane and out-of-plane PFM phase mappings of CIPS nanoflakes with the thicknesses of 10 nm (sample #1) and 18 nm (sample #2). Distinct ferroelectric domains can be observable in both the in-plane and out-of-plane directions in ultrathin CIPS samples, indicating and verifying the existence of multidirectional piezoelectricity and ferroelectricity in our CIPS samples used in this study. Then, local off-field PFM hysteresis measurements were conducted on CIPS nanoflakes with different thicknesses of 9 nm, 14.4 nm, and 24 nm, respectively, and the results are displayed in Figure 3.6. Typical butterfly-shaped amplitude loops and 180° phase switching between two discrete polarization states are illustrated, which are characteristic features of ferroelectric materials. Moreover, the ferroelectric domain pattern was modulated by applying a DC tip bias to the CIPS nanoflakes, showing the reversible polarization at a larger scale. Figure 3.7 displays the initial out-of-plane PFM phase and amplitude images and the corresponding modified ferroelectric domain before and after writing box patterns with external voltages.

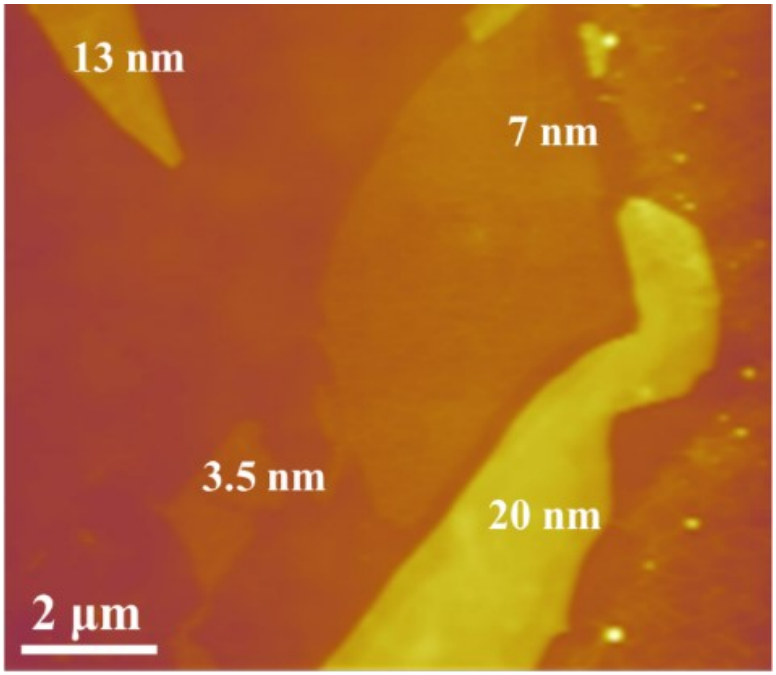


**Figure 3.8** AFM topographic image of mechanically exfoliated CIPS nanoflakes with different thicknesses.

In order to delve deeper into the piezoelectric characteristics of CIPS, ultrathin CIPS nanoflakes were prepared onto an insulating $SiO_2$ substrate to eliminate any potential non-piezoelectric interactions between the PFM probe and substrate. The topography of exfoliated CIPS nanoflakes at various thicknesses ranging from 3.5 to 20 nm is shown in Figure 3.8. Figures 3.9 and 3.10 demonstrate the amplitude and phase images recorded under different driving voltages from 1 V to 4 V, consistently displaying distinct and observable amplitude and phase contrasts. Robust electromechanical responses, even down to 3.5 nm (corresponding to five CIPS layers), are still obvious. Also, the PFM amplitude signal gradually increases as the voltage applied to the CIPS nanoflakes increases, suggesting that ultrathin CIPS samples

still possess strong intrinsic out-of-plane piezoelectricity. Here, varying thicknesses of CIPS nanoflakes generate varied electromechanical signal magnitudes, which decreases as the thickness reduces. Similar phenomena have been observed in different traditional and new vdW layered ferroelectric and piezoelectric materials[68,115,116]. This suggests that the increased substrate clamping effect and the enhanced depolarization field in ultrathin vdW layered ferroelectric materials are responsible for the decreasing trend in the piezoresponse concerning the decreased film thickness below 100 nm.

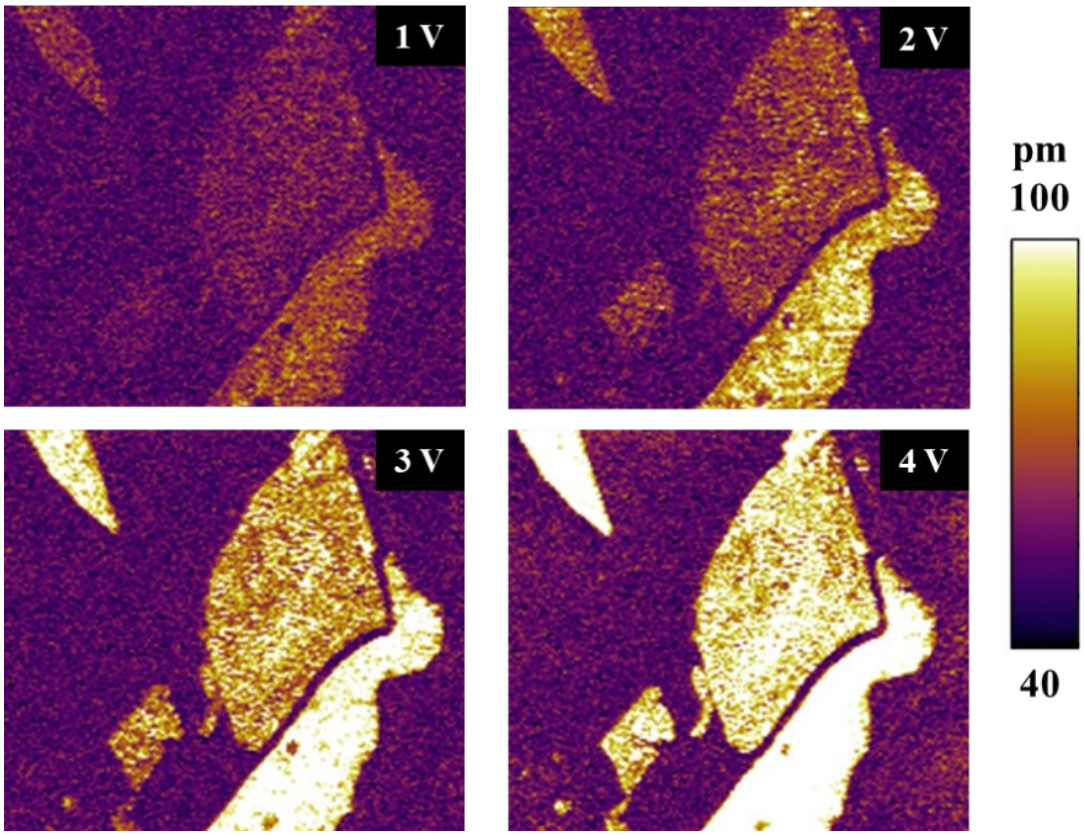


**Figure 3.9** Out-of-plane PFM amplitude images of CIPS nanoflakes exfoliated on $SiO_2$ substrate measured under different bias from 1 V to 4 V, respectively.

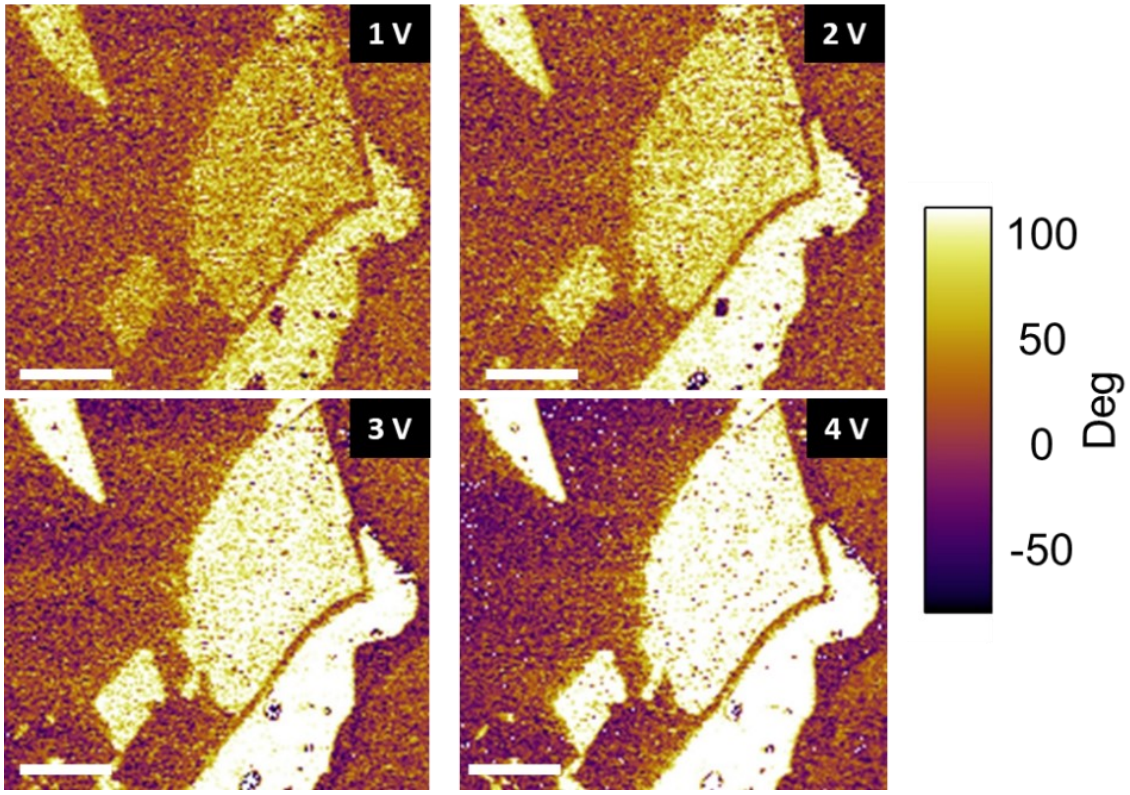


**Figure 3.10** Out-of-plane PFM phase images of CIPS nanoflakes exfoliated on $SiO_2$ substrate conducted under tips voltages from 1 V to 4 V, respectively. Scale: 2 μm.

Figure 3.11 shows the schematic of the PFM technique used for quantifying the piezoelectric response. The plot in Figure 3.11b indicates that the deflection signal of the conductive AFM tip increases with the driving voltage, thus the relationship between the piezoelectric amplitude and the applied voltage can be utilized to calculate the piezoelectric coefficient of the CIPS samples. The $d_{33}$ coefficient of 2D CIPS nanoflakes is plotted as a function of sample thickness and depicted in Figure 3.12a. From the CIPS sample of 3.5 nm thick, a high $d_{33}$ coefficient of up to 17.4 pm $V^{-1}$ is

quantitatively determined. The piezoelectric coefficient gradually enhances as the sample thickness increases and reaches 83 4 pm $V^{-1}$ when the thickness reaches 82 nm. As summarized in table 1, the measured piezoelectric response from CIPS is superior to most of the previously reported 2D layered piezoelectric materials and is in consistent with earlier studies[64,68,71,72,109,117].

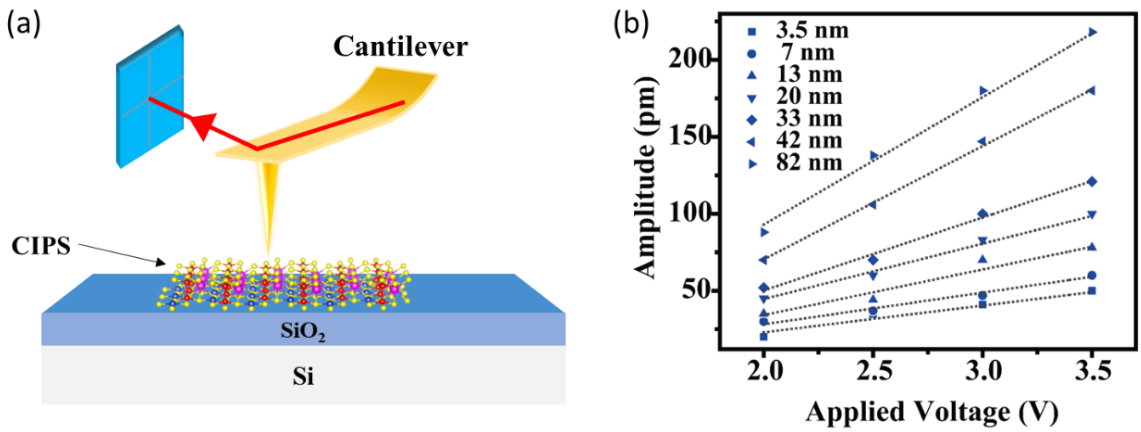


**Figure 3.11** (a) A schematic diagram illustrating the PFM set-up employed in this study to evaluate the out-of-plane piezoelectric response of CIPS nanoflakes. (b) A depiction showing the correlation between the vertical amplitude responses and the voltage that the conductive AFM tip applied to the CIPS flakes.

In traditional three-dimensional piezoelectric materials, the piezoelectric coefficient is usually positive in magnitude and the induced electric polarization always increases in response to a tensile strain. Piezoelectric coefficient can be divided into the clamped-ion and internal-strain factors[118]. The substantially weaker and softer interlayer vdW interactions than the intralayer chemical bonding enable a significant

suppression of the internal-strain term for low-dimensional vdW layered piezoelectric materials. Furthermore, in ultrathin layered piezoelectrics, the clamped-ion term is usually negative because of the "lag of Wannier center" effect[119]. In 2D layered CIPS, the interlayer vdW gap accounts for the majority of the dimension change upon application of external stress, while the change in the intralayer thickness and the associated dipole is rather insignificant. In CIPS system, the contribution of internal-strain to piezoelectricity is too weak to offset the negative clamped-ion term, resulting in the negative piezoelectricity in CIPS[119]. Therefore, when compressive stress is applied, the electric polarization in CIPS is more likely to increase.

On the other hand, as described in previous studies, the weak interlayer vdW interactions accompanied by the high displacive instability of the Cu atoms across the vdW gap are the main contributors to the significant out-of-plane piezoelectric strength in ultrathin CIPS nanoflakes[93,119,120]. The Cu atoms can hop across interlayer sites at ambient temperature as there is enough thermal energy to overcome the relatively small energy barrier. Most of the dimensional changes upon compressive stress occur with the soft vdW gap, which also promotes the hopping of Cu atoms between interlayer sites. As the occupancy of Cu in the interlayer site increases, the electric polarization strength of CIPS is also enhanced, thus leading to strong electromechanical responses in CIPS.

**Table 2.** Comparison of the experimental piezoelectric coefficient of 2D CIPS with the currently reported 2D vdW layered materials.

| **2D layered materials** | **Polarization direction** | **Piezoelectric coefficient** | **Ref. #** |
|---|---|---|---|
| Monolayer $WSe_2$ | In-plane | $d_{11}$ : 5.2 pm $V^{-1}$ | 121 |
| Monolayer 2H-$MoS_2$ | In-plane | $d_{11}$ : 3.78 pm $V^{-1}$ (armchair direction), 1.38 pm $V^{-1}$ (zigzag direction) | 61 |
| SnSe | In-plane | $d_{11}$ : 23 pm $V^{-1}$ (190 nm) | 110 |
| $SnS_2$ | Out-of-plane | $d_{33}$ : 2.2 pm $V^{-1}$ (4 nm mechanical exfoliated)<br>$d_{33}$ : ~5 pm $V^{-1}$ (2.5 nm CVD-grown) | 71,72 |
| SnS | Out-of-plane | $d_{33}$ : ~1.85 pm $V^{-1}$ (5 nm) | 109 |
| Janus MoSSe monolayer | Out-of-plane | $d_{33}$ : 0.1 pm $V^{-1}$ | 117 |
| α-$In_2Se_3$ | Out-of-plane | $d_{33}$ : 0.34 pm $V^{-1}$ (monolayer) to 5.6 pm $V^{-1}$ (bulk) | 68 |
| α-$In_2Se_3$ | Out-of-plane | $d_{33}$ : 0.53 pm $V^{-1}$ (4.4 nm) | This work |
| 3R-$MoS_2$ | Out-of-plane | $d_{33}$ : 0.9 pm $V^{-1}$ (18 nm) | 64 |
| CIPS | Out-of-plane | $d_{33}$ : -95 pm $V^{-1}$ (bulk) | 93 |
| CIPS | Out-of-plane | $d_{33}$ : 17.4 (3.5 nm) to 83 pm $V^{-1}$ (82 nm) | This work |

Moreover, unlike conventional ferroelectrics, the migration of Cu across the vdW gap gives rise to the quadruple-well energy potential in CIPS[122]. The hoping of Cu atoms across the vdW gap under external bias also contributes to a negative capacitance in CIPS, where the polarization change is opposite to the electric field, as shown in Figure 3.13[123].

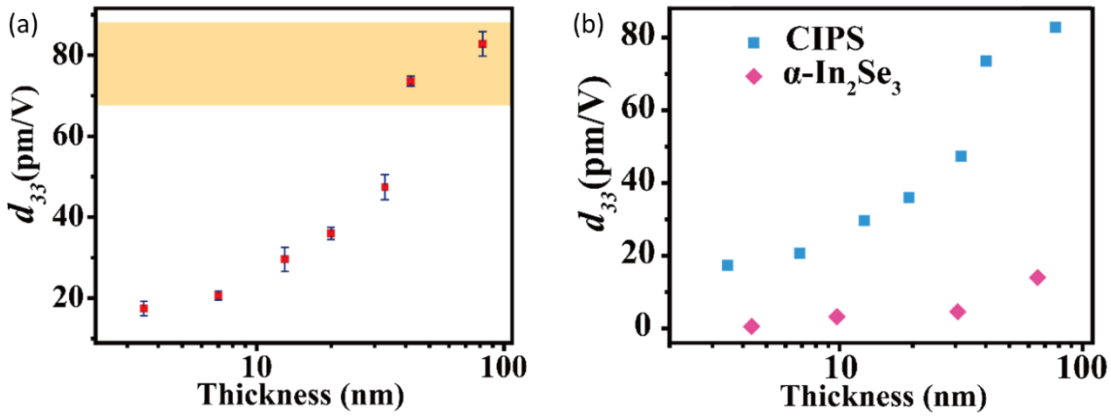


**Figure 3.12** (a) The relationship between the $d_{33}$ piezoelectric constant and the thickness of the CIPS nanoflakes. (b) Comparison of the $d_{33}$ coefficient of CIPS and α-$In_2Se_3$ nanoflakes under identical measurement conditions.

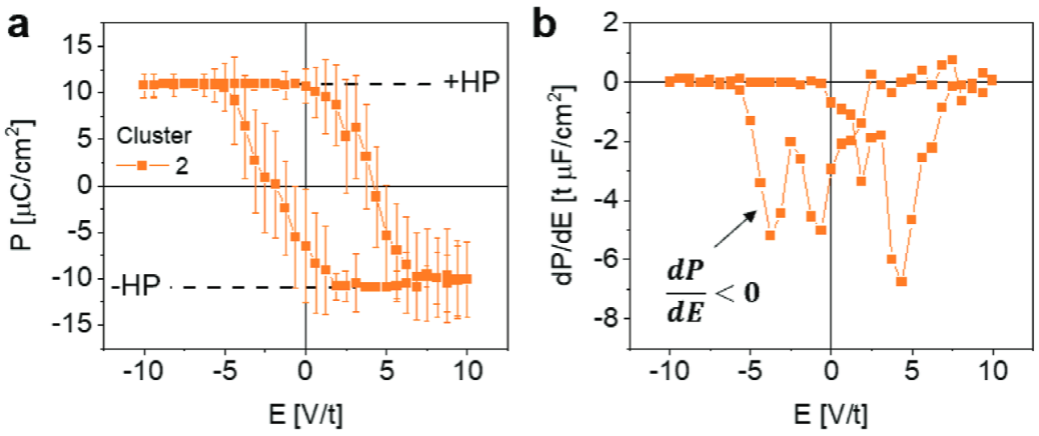


**Figure 3.13** (a) Polarization hysteresis loop and (b) capacitance-electric field curve of CIPS[123].

In order to provide a direct and reliable comparison, we additionally quantified the piezoelectric coefficient of α-$In_2Se_3$, which is a well-studied 2D layered ferroelectric and piezoelectric semiconductor, under the same measurement settings using our test system. In the present study, the estimated piezoelectric coefficient of few-layer CIPS is almost 30 times greater than that of few-layer α-$In_2Se_3$ (0.53 pm $V^{-1}$) and nearly 6 times higher for thicker nanoflakes. Based on earlier theoretical and experimental works on the piezoelectricity of CIPS and α-$In_2Se_3$, bulk CIPS possesses far higher $d_{33}$ piezoelectric coefficient than that of bulk α-$In_2Se_3$ crystal [68,120,124,125]. The findings in this study are in accord with the previous studies. The significant difference in the magnitude of the piezoelectric coefficient is resulting from the difference in the crystal structures of the two vdW layered piezoelectric materials. The crystal structure of both α-$In_2Se_3$ and CIPS is intrinsically non-centrosymmetric. In α-$In_2Se_3$, the vertical piezoelectricity originates from the off-centering Se atoms causing electric dipoles, whereas the intralayer atoms are stably bound together by strong chemical bonding. In contrast to α-$In_2Se_3$, the out-of-plane piezoelectricity is mainly contributed from the Cu atoms, in which the highly unstable displacement of Cu atoms can substantially boost the electric polarization under stress. Therefore, CIPS has a significantly larger magnitude of the piezoelectric coefficient at an identical thickness. In addition, from a technological perspective, the $d_{33}$ coefficient of 2D CIPS is comparable to those

high-performance inorganic piezoelectric thin films[93,113,126,127], thus rendering it an appealing candidate material for developing piezotronic nanotechnology.

## 3.4 Piezotronics effect in 2D CIPS-based nanodevices

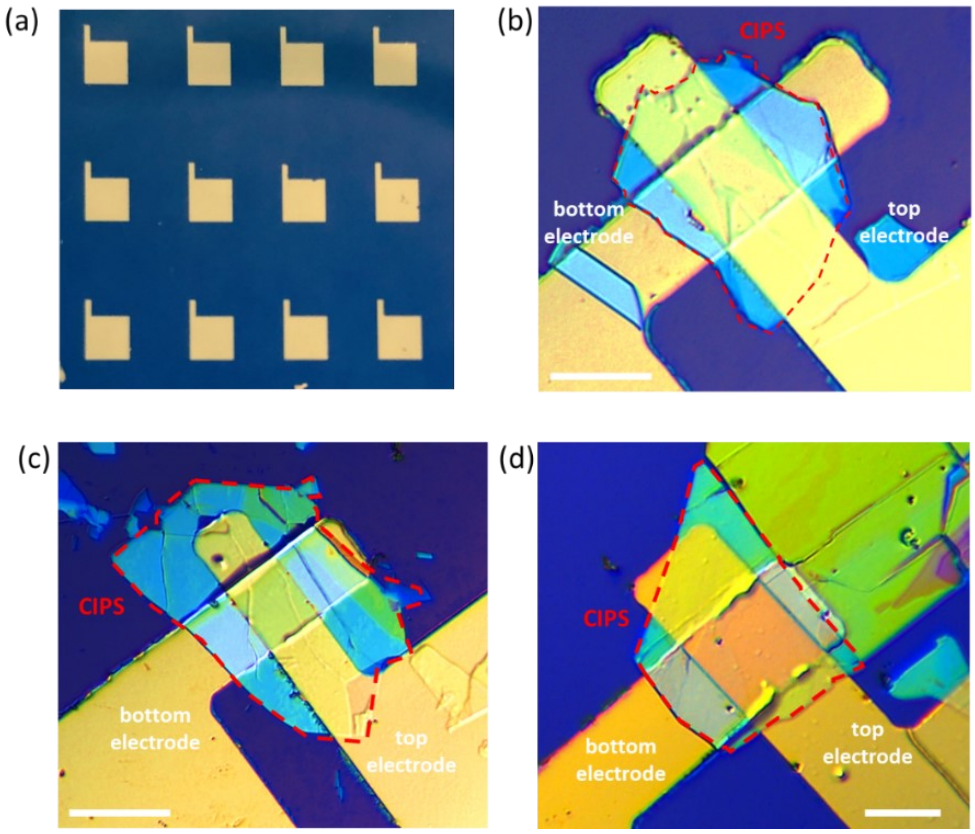


**Figure 3.14** (a) An array of patterned Au electrodes. (b)-(d) Optical images of several fabricated vertical CIPS devices on $SiO_2$ substrates. Scale bar:10 μm.

2D vdW piezoelectrics display significant advantages over traditional perovskite oxide-based materials for the development of miniature device configurations. Conventional perovskite oxides show poor complementary compatibility in metal-oxide-semiconductor structures as they approach to atomically thin thicknesses,

requiring specific substrates or specialized synthesis methods. This constrains their potential utilization in nanoscale piezoelectric devices. In contrast, 2D vdW piezoelectric materials-based nanodevices show excellent compatibility with a variety of substrates, including silicon and polymers, while preserving their piezoelectric properties in ultrathin thickness. In this work, CIPS-based nanodevices were successfully fabricated on silicon substrates, validating their high compatibility with the existing semiconductor industry. Utilizing the pronounced vertical piezoelectricity of CIPS, the room-temperature transfer characteristics of CIPS-based nanodevices were investigated to demonstrate possible applications.

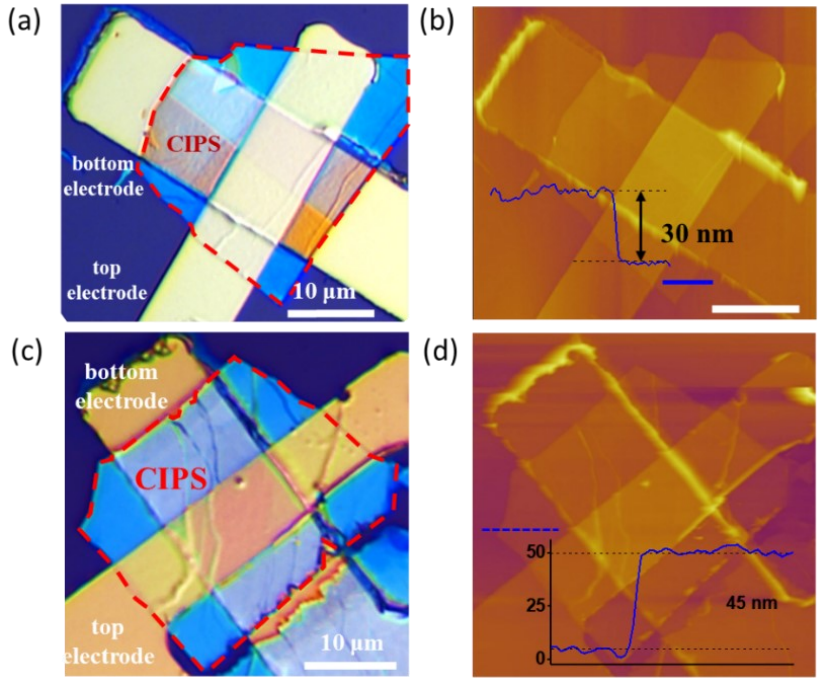


**Figure 3.15** (a)(c) Optical images and (b)(d) the corresponding AFM images and height profiles of typical vertical CIPS devices with symmetric top and bottom Au electrodes.

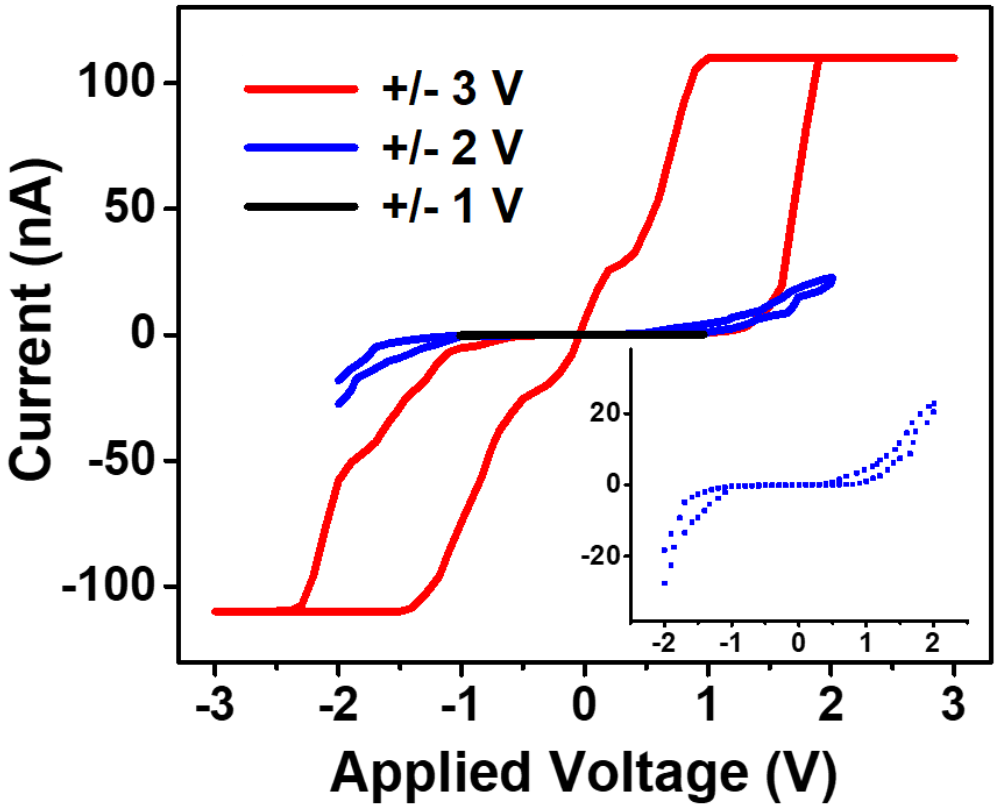


**Figure 3.16** Electrical characteristics of the ferroelectric CIPS sample when the applied bias V<$V_C$ (Schottky junction behavior) and V>$V_C$ (resistive switching behavior). Inset: enlarged view of the *I-V* curve.

The structure of the piezotronic devices includes two Schottky contacts (Au-CIPS interfaces) and a semiconducting channel (CIPS layers). For the construction of CIPS-based devices, standard photolithography and E-beam evaporation were applied to prepare arrays of electrodes on silicon substrates. These pre-deposited Au electrodes could be easily picked up and stamped onto different surfaces while maintaining their atomically smooth surfaces (see Figure 3.14a). Following this, a layer of mechanically

exfoliated CIPS nanoflake was positioned on top of the pre-fabricated Au electrode on $SiO_2$/Si substrate. Lastly, another pre-deposited Au electrode was mechanically exfoliated, aligned, and attached on top of the CIPS/Au stack using typical dry transfer method with the assistance of an optical microscope, resulting in precise and clean vdW metal-semiconductor contacts. The method of fabricating metal-semiconductor junction devices using pre-fabricated metal electrodes followed by mechanical transfer process offers significant benefits compared to the directly deposition of metal electrodes onto 2D semiconducting materials. Especially, traditional metal evaporation techniques through direct chemical bonding can introduce defects, trapped states, and polymer residues at the metal-semiconductor interfaces. These imperfections can lead to the pinning of the Fermi level, modification in band structures, changes in Schottky barrier height, and charge transfer characteristics. Additionally, the high-energy metal bombardment during the evaporation procedure can degrade or even damage the crystal structure of the ultrathin materials. For the case of the vertical device structures constructed in this study, the influence is more dominant that metal could diffuse into the CIPS layer and potentially penetrating the ultrathin semiconducting channel, causing a short circuit with the bottom electrode during electrical measurements. In contrast, vdW integration is a gentle and non-destructive method for assembling metal electrodes onto 2D materials to fabricate various device structures. By avoiding direct

chemical deposition, the associated interfacial defects, trap states, and problems related to metal diffusion are minimized. This approach helps to maintain the crystal quality and the intrinsic properties of the 2D materials and significantly reduce the effect of Fermi level pinning. Figures 3.14 and 3.15 display the optical microscopy images of various constructed vertical CIPS-based devices and it is observable that the smooth and flat surfaces of the transferred top metal electrodes are preserved.

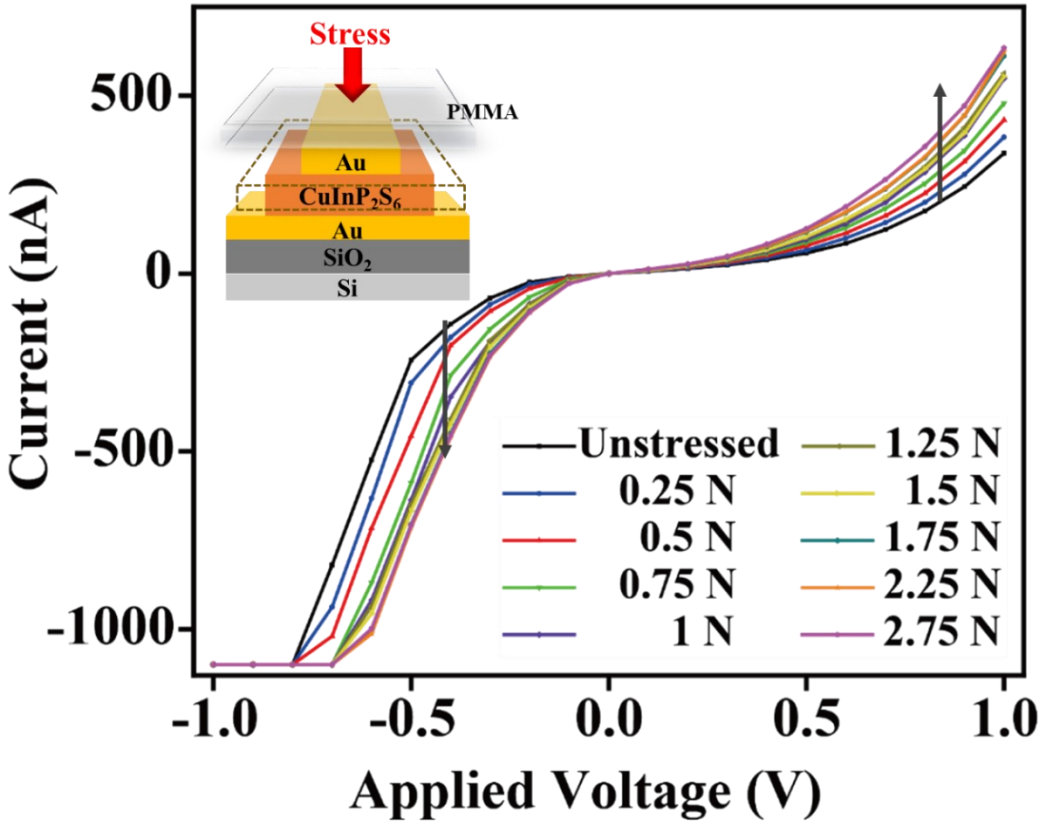


**Figure 3.17** *I-V* characteristics of the fabricated CIPS device on rigid $SiO_2$ substrate subjected to varying degrees of compressive stress.

The *I-V* characteristics of the CIPS device in an unstressed situation are presented in Figure 3.16. Typical behavior of Schottky contacts can be observed when the external

voltage is less than the coercive voltage ($V_c$), suggesting that good Schottky contacts are established between the two vertical metal-semiconductor junctions, which is advantageous for performing electrical measurements. The *I-V* curve shows the representative resistance switching characteristic of the ferroelectric CIPS when the applied voltage $V>V_c$. The large hysteresis loop indicates that the two resistance states shall result from the switching of ferroelectric polarization states, rather than the movement of residues and/or defects introduced during the vdW assembly procedure. Besides, the piezoelectric-regulated electrical transfer behavior of the CIPS-based devices under varying mechanical stresses was examined. The constructed metal-semiconductor-metal (M-S-M)-structured devices are enclosed by a thin layer of polymethylmethacrylate (PMMA), as shown schematically in the inset of Figure 3.17. This configuration allows the external mechanical stress to be delivered uniformly throughout the active area of CIPS nanoflake, and the piezoelectric polarization charges to be evenly distributed on the sample surfaces. To ensure that the ferroelectric polarization in CIPS was not influenced by the applied mechanical stress and external bias, the piezo-induced electrical responses of the CIPS-based devices were recorded under vertically applied compressive force ranging from 0.25 N to 2.75 N with a small voltage ($V \ll V_c$). In order to prevent excess current from passing through the ultrathin 2D semiconducting channel and damaging the CIPS piezotronic devices, the maximum

detectable output current is capped at 1.1 μA. Application of stress can manipulate the output current in both forward and reverse conditions, with an apparent growing trend in the current magnitudes. With a 1.75 N compressive force and an external voltage of -0.5 V, the current rises from 243.3 nA to 704.7 nA, and it begins to saturate when subjected to a higher compressive force (Figures 3.17 and 3.18b).

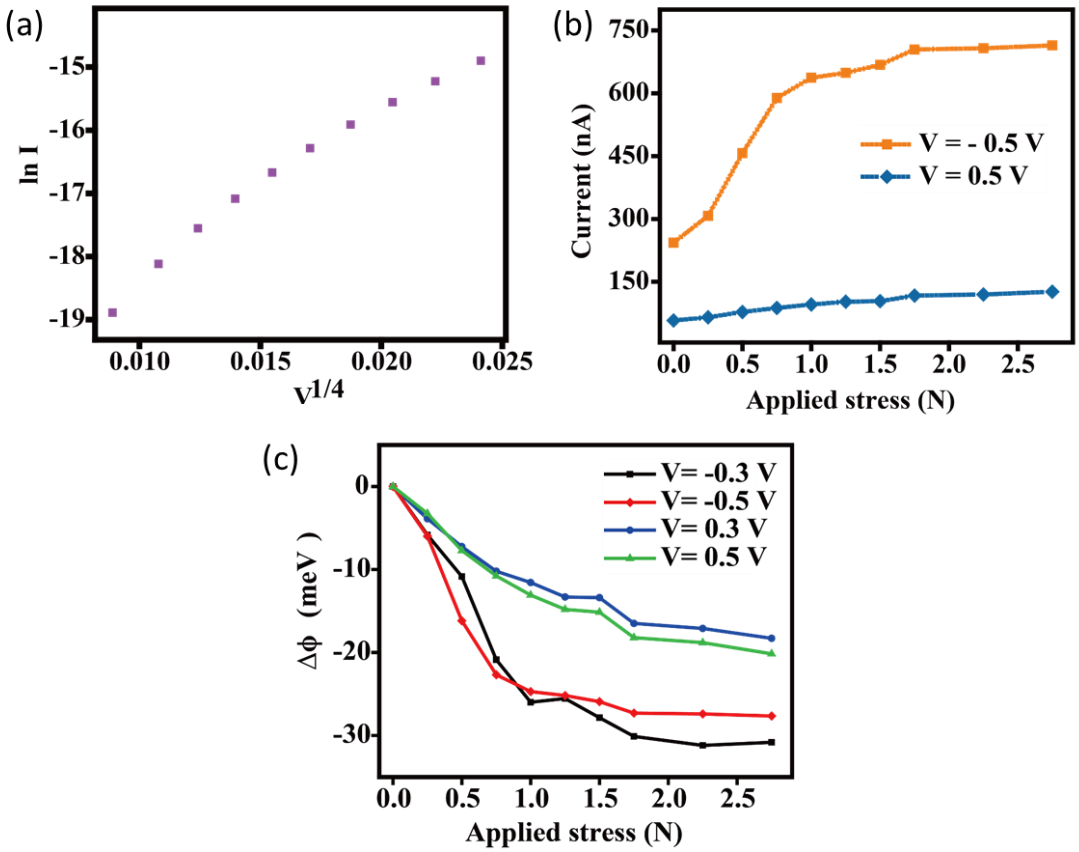


**Figure 3.18** (a) The value of ln $I$ as a function of $V^{1/4}$ based on the experimental data from Figure 3.17. (b) Output current under different stressed conditions with an external voltage of ± 0.5 V. (c) The estimated variation in Schottky barrier height corresponding to the compressive force exerted, extracted at external voltages of ± 0.3 V and ± 0.5 V, respectively.

Based on the experimental data presented in Figure 3.16, the stress-induced Schottky barrier height change (ΔΦ) is quantitatively determined. As discussed previously, the unstressed *I-V* curve (Figure 3.15) indicates the presence of Schottky contacts at the two metal-semiconductor interfaces, hence the CIPS device can be considered as a single piezoelectric layer (CIPS) sandwiched between two opposing Schottky barriers. Since all the electrical characterizations were achieved at ambient temperature, the thermionic emission and diffusion processes were mainly responsible for regulating the electrical transfer behavior at the metal-semiconductor junctions. Classic thermionic emission-diffusion theory can be adopted to describe the current flowing through the Schottky barrier at temperature $T$ and constant voltage $V$ ($V >> 3kT/q$, ~77 mV) with the following equation [128],

$$I = S_s A^{**} T^2 \exp\left(-\frac{\phi_s}{kT}\right) \exp\left(\frac{\sqrt[4]{q^7 N_D (V + V_{bi} - \frac{kT}{q})/(8\pi^2 \varepsilon_s{}^3)}}{kT}\right) \quad (1)$$

where $S_S$ represents the area of the source Schottky barrier, $A^{**}$ refers to the effective Richardson constant, $q$ is the electron charge, $k$ is Boltzmann constant, $N_D$ is the donor impurity density, $V_{bi}$ refer to the build-in potential, and $\varepsilon_s$ is the permittivity of CIPS. The value of ln $I$ as a function of $V^{1/4}$ are plotted in Figure 3.18a using the data extracted from the unstressed *I-V* curve of Figure 3.17, and the linear relation between ln $I$ and $V^{1/4}$ verifies the thermionic emission–diffusion model dominant the transfer process. The $S_S$, $A^{**}$, $N_D$, and $T$ terms are assumed to be independent under a small stress. The

stress-induced change in the Schottky barrier height can be derived by the following equation,

$$\ln\left[\frac{I_\varepsilon}{I_0}\right] \sim -\Delta\phi_s/kT \quad (2)$$

where $I_\varepsilon$ and $I_0$ are the current measured with and without stress application at a fixed voltage $V$, respectively, and $\Delta\phi$ is the change in Schottky barrier height under stress.

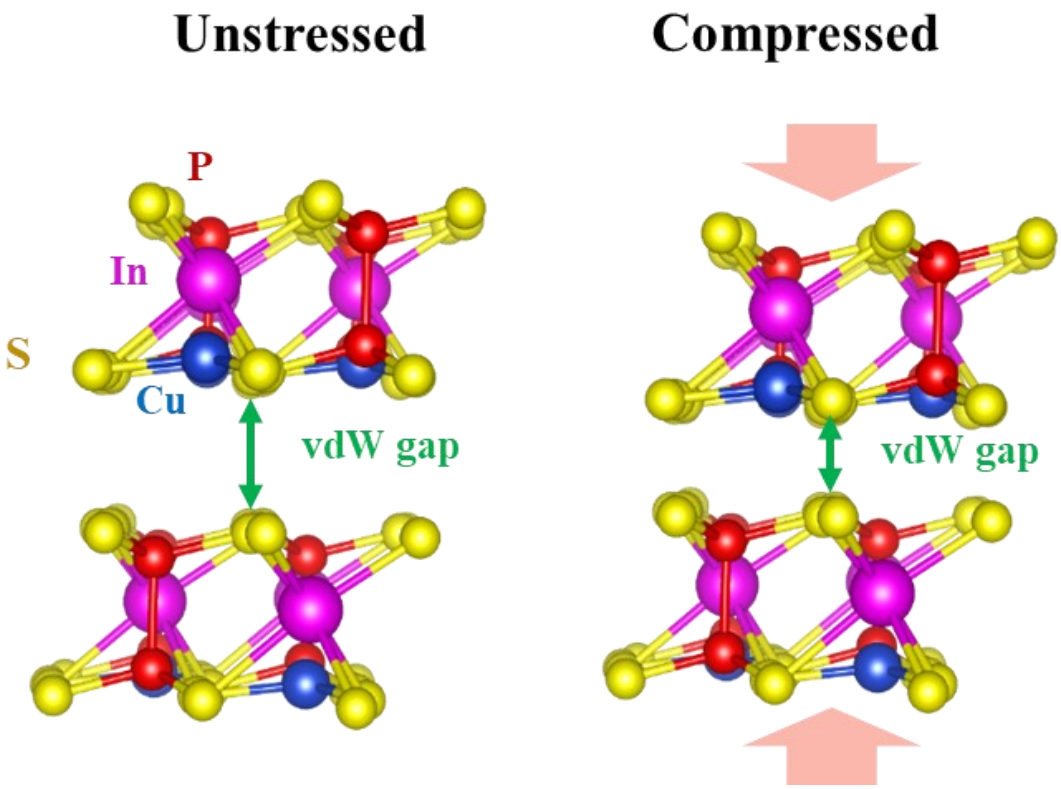


**Figure 3.19** Schematic of the structure of bilayer CIPS under unstressed and compressed conditions.

The results are presented in Figure 3.18c at two fixed voltages of ± 0.3 V and ± 0.5 V, demonstrating that increasing compressive stress reduces both the barrier heights at the source and drain contacts. Furthermore, the trend in the change of Schottky barrier

height is rather constant under different biases, showing that the voltage applied to the piezotronic device has little effect on the variation in barrier height. The stress-induced modification of electrical properties of the CIPS-based junction devices is consistent with the piezotronic effect reported previously in other 2D piezoelectric semiconductors, in which the external mechanical stimulus acts as a "gate" to regulate the carrier transport processes of piezotronic devices[29,108].

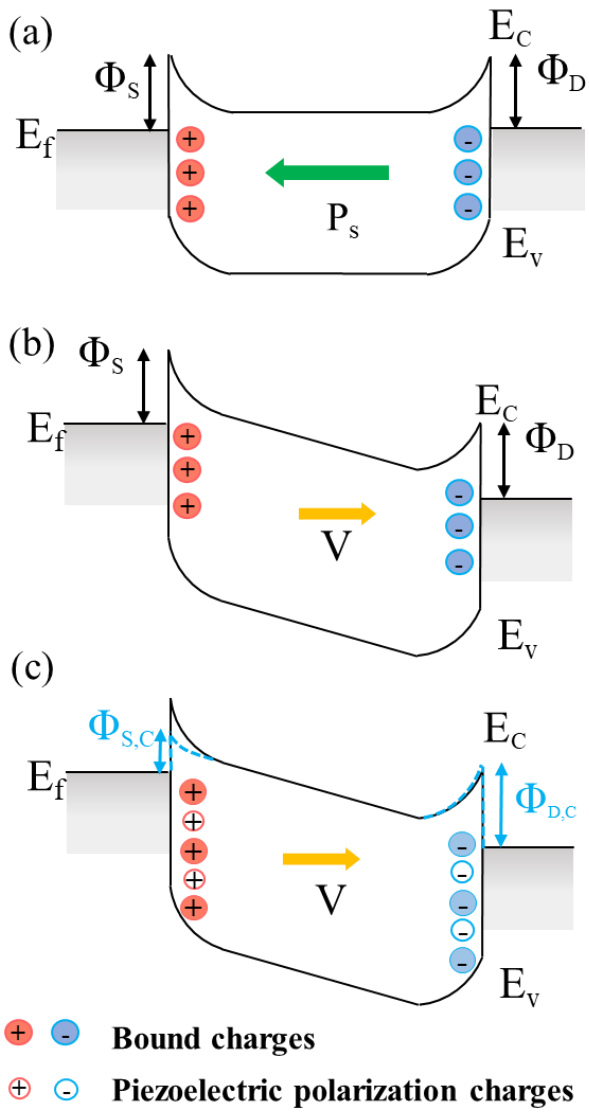


**Figure 3.20** Band diagrams under different situations: (a) no external voltage and unstressed; (b) a non-zero external voltage is applied to unstressed CIPS flake causing the energy bands to tilt; (c) with the application of compressive stress along with a non-zero external voltage, which results in the generation of a piezopotential at the metal-semiconductor interfaces. $\Phi_S$ and $\Phi_D$ represent the initial heights of the Schottky barriers at the source and drain contacts, and $\Phi_{S,C}$ and $\Phi_{D,C}$ denote the changes in barrier heights at the source and drain modulated due to the piezoelectric polarization charges, respectively.

The current modulation of CIPS nanosheets can be explained through the piezotronic effect. The crystal structures under unstressed and compressed conditions are depicted in Figure 3.19. In the absence of mechanical stress and external voltage, intrinsic ferroelectric polarization charges are present on both surfaces of the CIPS flake, as indicated in Figure 3.20a. When mechanical stress is applied, piezoelectric polarization charges emerge on the surfaces of the CIPS, which can influence the metal-semiconductor junctions. The piezopotential that arises from the applied stress can alter the heights of the Schottky barriers. As shown in Figure 3.20b, at an unstressed state, applying a small voltage (significantly less than $V_c$) causes the energy bands of the semiconducting CIPS to tilt. If compressive stress is applied while a small external voltage is present, the piezoelectric polarization charges at the interfaces modify the Schottky barrier heights, leading to improved electrical performance. The generation of positive piezoelectric polarization charges results in a positive piezopotential, which reduces the Schottky barrier at the semiconductor-metal interface. Conversely, negative piezoelectric polarization charges generate a negative piezopotential, which increases the barrier height, as illustrated in Figure 3.20c. The modulations in the energy bands at the metal-semiconductor junctions are asymmetric, leading to changes in the charge transfer. As a result, the current can be controlled by using the induced piezopotential as a gating source. In this study, over 20 two-terminal CIPS nanodevices have been

constructed and their piezotronic performance was examined. The majority displayed consistent transfer characteristics with a dominant piezotronic effect at room temperature, indicating high reliability and consistency in the findings. This opens up significant opportunities for the integration of CIPS in nanoscale energy harvesting applications.

## 3.5 Performance of CIPS-based piezoelectric nanogenerators

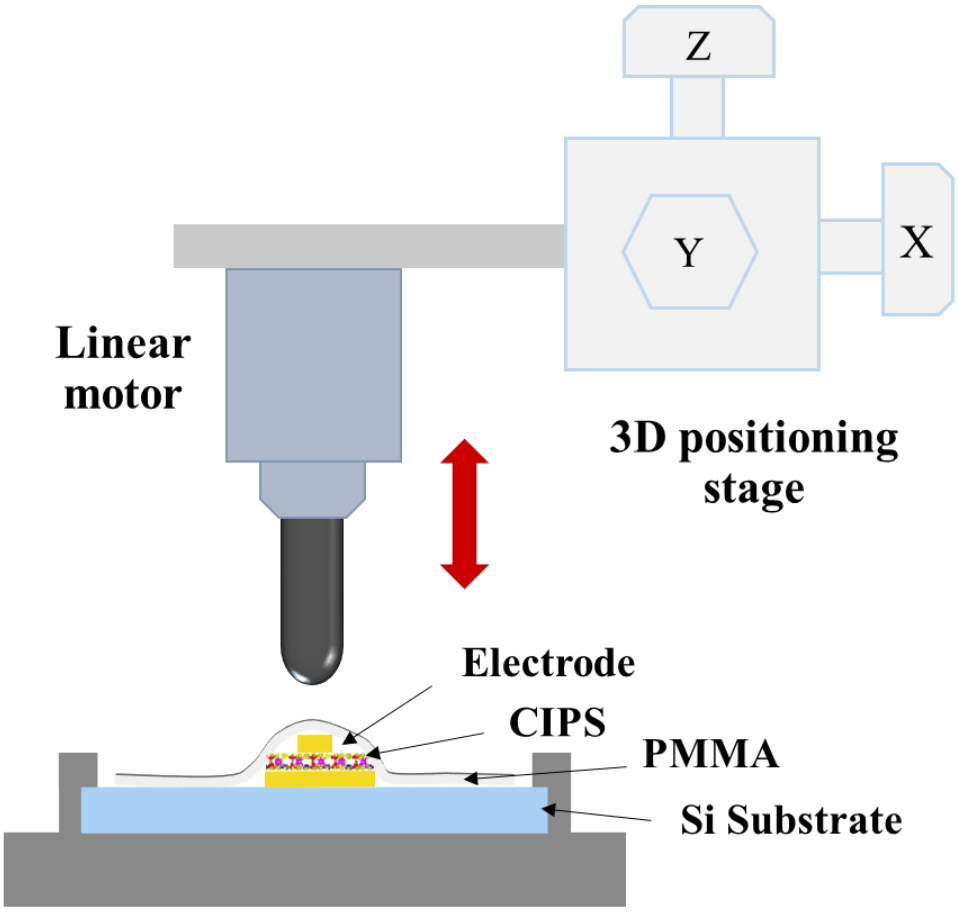


**Figure 3.21** A schematic diagram demonstrating the experimental setup to analyze the 2D CIPS PENGs in this work.

To broaden the exploration of the piezotronic effect in 2D CIPS and further

demonstrate its potential to incorporate into devices, CIPS-based piezoelectric nanogenerators (PENG) were constructed and their performances were evaluated under home-built experimental system as schematically illustrated in Figure 3.21. Piezoelectric responses from the CIPS PENG, where piezoelectric CIPS nanoflake was embedded between two Au electrodes on $SiO_2$/Si substrate, were recorded under continuous vertical periodic compression and release motions. When employing thinner CIPS samples, the current density can be improved; however, the polarization strength is also increasingly suppressed by the depolarization field effect. Therefore, the CIPS nanoflakes was chosen to be within 20 to 50 nm in thickness, with energy-harvesting active areas of approximately 100 to 140 $\mu m^2$. Under compressive stress, piezo-polarized charges were generated at the two surfaces of the CIPS nanoflakes and regulated the barrier height on the metal-semiconductor interfaces, leading to an electrical output peak. When the mechanical force was removed, opposite-sign piezoelectric polarization charges were produced, causing an electrical signal in the reverse direction.

Figures 3.22 and 3.23 display the corresponding piezoelectric voltage and current outputs that are repeatedly produced from PENG based on CIP nanosheets of different thicknesses under periodic compression and release forces. The generated piezoelectric voltage and current from a typical PENG device, based on a 2D CIPS flake with the

thickness of approximately 45 nm, are around 8 mV and 1.15 nA, respectively (Figure 3.22). While utilizing a thinner CIPS nanoflake of approximately 15 nm thick, the peak piezoelectric voltage and current outputs from the PENG device increase to 12 mV and 1.7 nA, respectively, as shown in Figure 3.23. These results signify the superior piezoelectric characteristics of 2D CIPS nanoflakes.

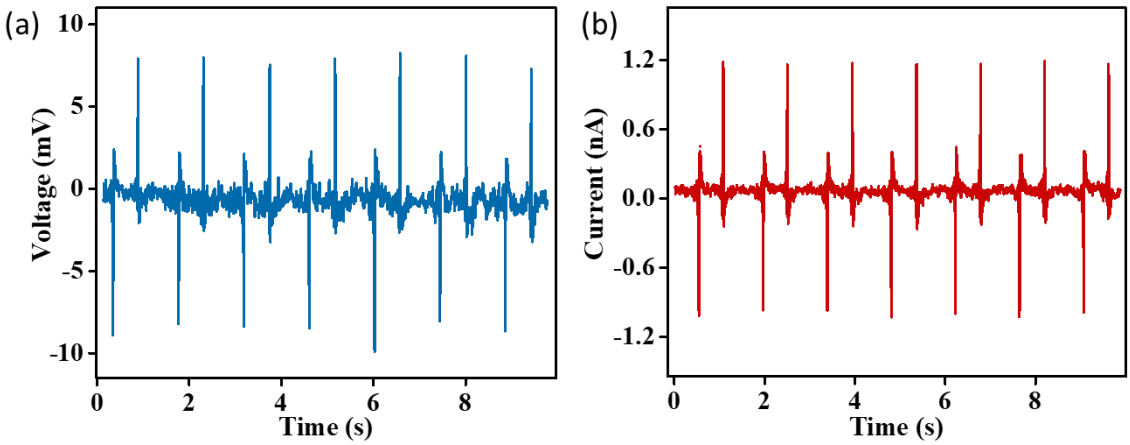


**Figure 3.22** The (a) voltage and (b) current output of a 45 nm CIPS PENG device induced by periodic longitudinal compression.

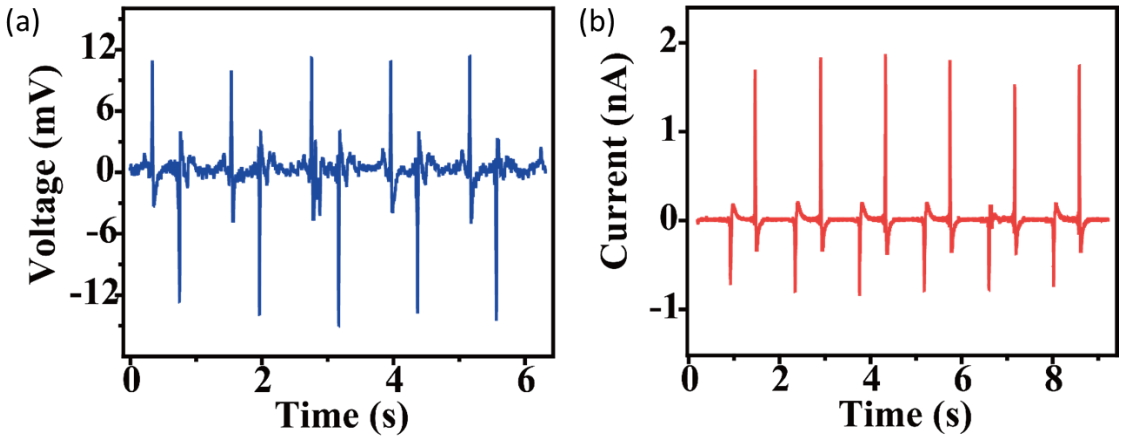


**Figure 3.23** The (a) voltage and (b) current output of a 15 nm CIPS PENG device under the application of periodic longitudinal compression.

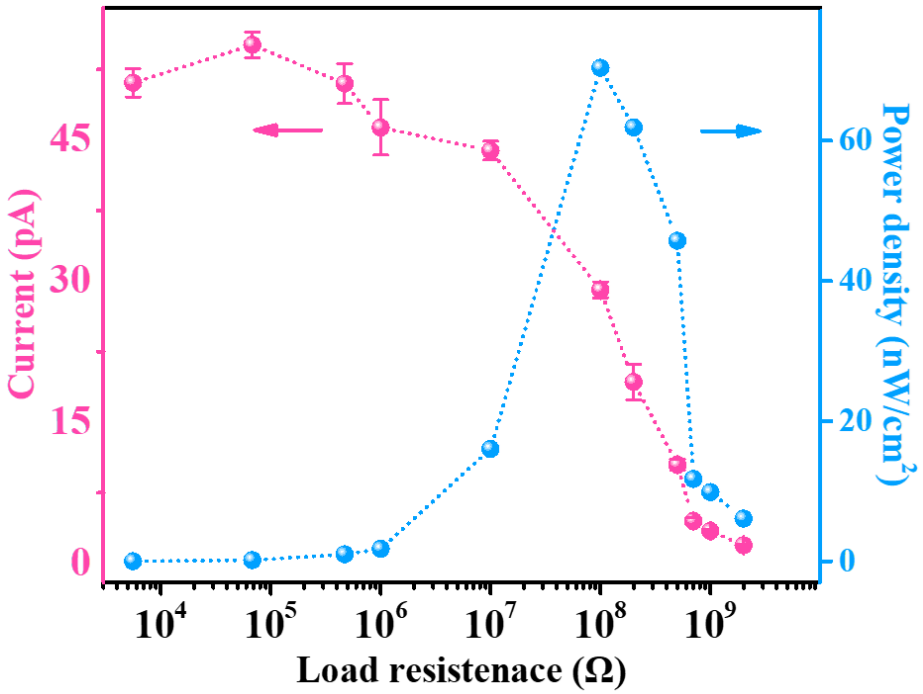


**Figure 3.24** The peak output piezoelectric current and power density of a 2D CIPS PENG device under different loading resistances.

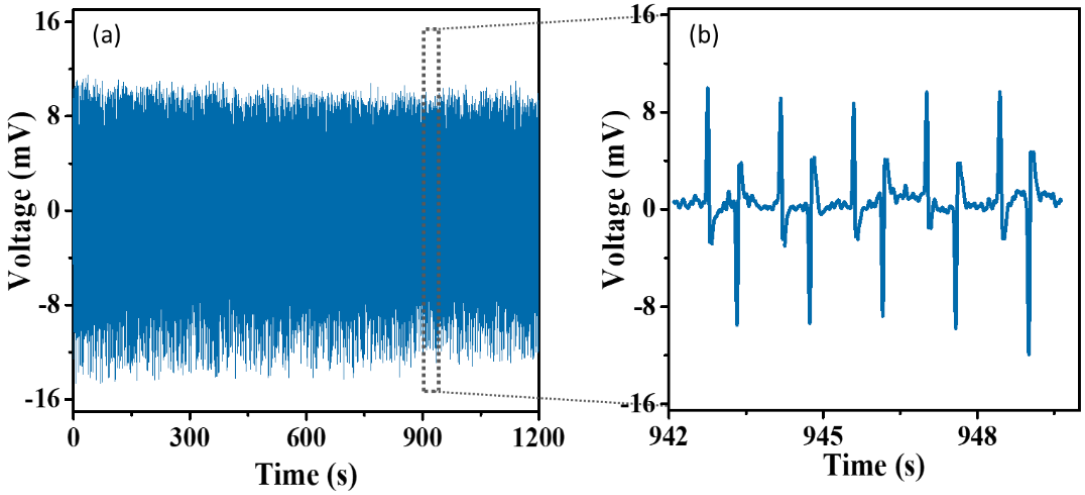


**Figure 3.25** Endurance test of a prototype 2D CIPS PENG under periodic compression and relax over 1200 seconds.

A wide range of external load resistances were used for evaluating the piezoelectric current outputs in order to derive the output power of the CIPS PENG.

Figure 3.24 shows the power density and current outputs as a function of the employed load resistance. When the loading resistance is less than 10 MΩ, the piezoelectric peak current generally stays constant; when the external load resistance further increases, it starts to decrease significantly. With a load resistance of 100 MΩ, the single CIPS nanoflake-based PENG device, having an effective energy harvesting area of around 120 $\mu m^2$, demonstrating a maximum power density of approximately 70.4 nW $cm^{-2}$. In addition, the piezoelectric output stability and mechanical durability were tested by applying continuous and cycled compressive stress to the CIPS PENG device over a long operation time of longer than 1200 s, as shown in Figure 3.25. Throughout the testing period, the measured voltage outputs are nearly consistent with no discernible fluctuations, indicating the stability of the output piezoelectric signals and the good mechanical endurance of the PENG device.

To further assure that the electrical outputs were generated due to the piezoelectric effect in CIPS rather than from any non-piezoelectric aspects such as the testing system, a connection polarity switching analysis was also performed. Figure 3.26 depicts the voltage output signals from the CIPS PENG, indicating that when the connection polarity is switched, the direction of the output voltage is also reversed as anticipated. The voltage output from a bare substrate coated with PMMA layer (Figure 3.27) also validates the origin of the piezoelectric signals from the CIPS PENG devices.

The piezoelectric current responses of the PENG in response to various applied stresses are shown in Figure 3.28. The distinctive out-of-plane piezoelectric features of CIPS are demonstrated by the increasing magnitude of the piezoelectric current with increasing stress.

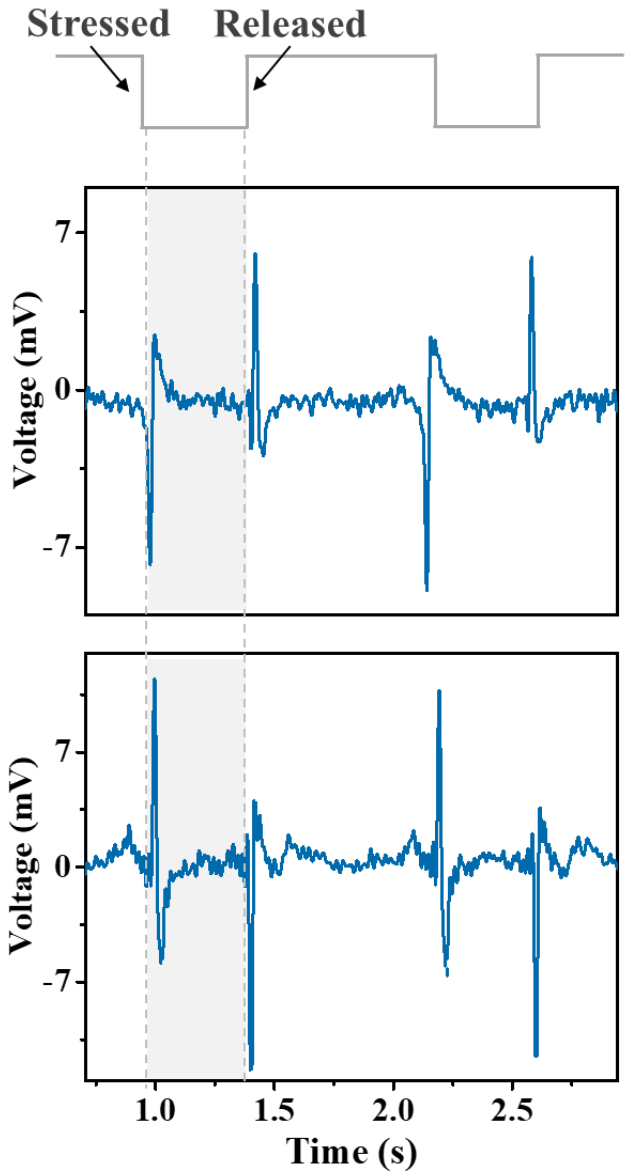


**Figure 3.26** The piezoelectric output voltages generated by the CIPS PENG in the forward and reverse connections, respectively.

Considering the vertically stacked structure, the thickness of the CIPS nanoflakes employed in the PENG devices is equivalent to the piezoelectric channel length. Because of the nanometer-sized channel length, the CIPS PENG devices exhibit a high output piezoelectric current that is one to two orders of magnitude higher than that of the reported 2D in-plane PENGs based on a single nanoflake such as $MoS_2$, $WSe_2$[54,61,112], and layered metal dichalcogenide[72]. Also, the piezoelectric voltage output of the vertical CIPS PENG is comparable to that of other 2D in-plane PENGs. These findings reveal that 2D CIPS nanoflakes offer immense potential for implementation in high-performance, nanoscale energy harvesting applications.

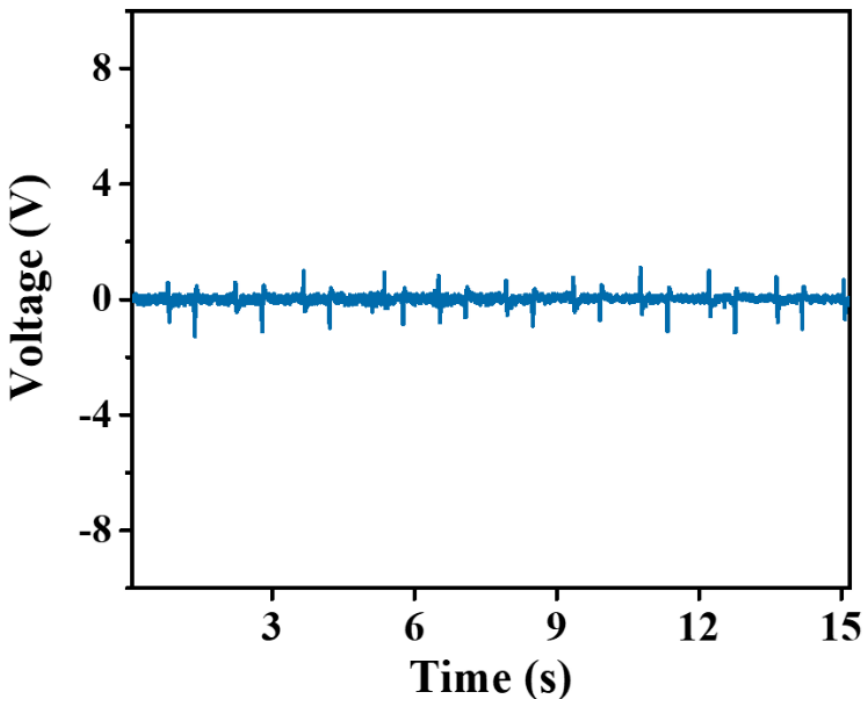


**Figure 3.27** Voltage output recorded from PMMA-coated bare $SiO_2$ substrate.

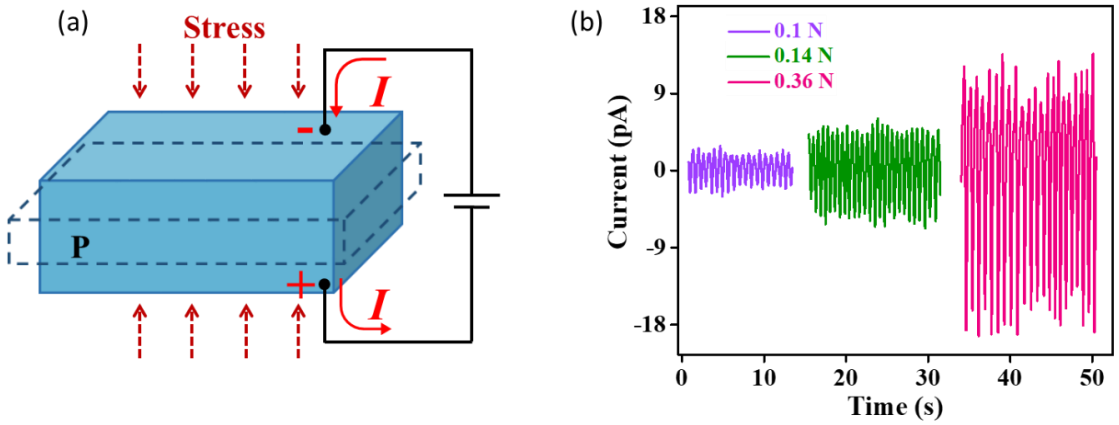


**Figure 3.28** (a) Schematic of the energy harvesting device based on piezoelectric CIPS and (b) the generated piezoelectric currents when subjected to different levels of compressive stress.

## 3.6 Summary

In summary, quantitative analysis of the layer-dependent out-of-plane piezoelectric response of CIPS nanosheets in the 2D regime was conducted and the piezotronic effect in CIPS-based devices was demonstrated. PFM measurement reveals that the vertical piezoelectric signals of CIPS substantially enhance as sample thickness increases. In particular, the few-layer CIPS exhibits a remarkable piezoelectric $d_{33}$ coefficient of 17.4 pm $V^{-1}$, which is superior to the values reported in other 2D vdW piezoelectric materials that have been investigated currently. Furthermore, a simple and non-destructive vdW integration strategy was employed to construct 2D CIPS-based PENG. Under uniform compression, the output piezoelectric

current and voltage of the CIPS nanogenerator reach a maximum of 1.7 nA and 12 mV, respectively, with a peak power density of 70.4 mW $cm^{-2}$. The robust out-of-plane piezoelectricity in 2D CIPS nanosheets endow them with great promise for incorporation into nanoscale energy storage and conversion, and piezotronic devices.

# Chapter 4 Direct Observation of Intrinsic Room-Temperature Out-of-plane Ferroelectricity in vdW Layered CCPS Nanoflakes

## 4.1 Introduction

Smart materials possess a variety of intriguing properties, including ionic conductivity, ferroelectricity, and magnetic polarization, which are of great technical significance for information storage and synapse applications[129,130]. The coexistence of ferroelectric and ferromagnetic characteristics in multiferroic materials is more promising and demanding for fundamental research and various technological applications[131,132]. However, it is challenging to achieve both ferromagnetic and ferroelectric ordering simultaneously in single-phase materials, making multiferroic materials rather uncommon. Furthermore, the problems of size effects, dangling bonds, and interface effects of traditional multiferroic materials, such as $BiFeO_3$, render them difficult to comply with the development demand for device miniaturization while maintaining satisfactory device performance, greatly restricting their practical applications[133].

Emerging two-dimensional (2D) van der Waals (vdW) layered materials with unprecedented physical attributes have sparked tremendous research interest in exploring and investigating new 2D materials with multifunctional features for device fabrication. Several studies in recent years have reported the presence of ferromagnetic[134,135], ferroelastic[136], ferroelectric[23,30,65,67], and coexisting ferroelastic-ferroelectric orderings[137,138] in various 2D materials. These findings suggest the potential for developing low-dimensional multiferroicity, particularly the coexistence of ferromagnetic and ferroelectric orders, which is very appealing from the perspective of both fundamental research and practical applications. Considerable efforts have been made to explore novel 2D multiferroic materials, and theoretical studies have predicted multiferroicity at the atomic thickness in numerous vdW materials[139,140]. The metal thiophosphate material family has garnered significant interest recently due to its ability to offer a stable framework for introducing diverse functional transition metal ions into the structure and the potential utilization of its desirable material properties for a wide variety of applications[91,122,141]. As discussed in the previous chapter, the most investigated layered metal thiophosphate material $CuInP_2S_6$ (CIPS) exhibits Cu-ion migration effect and robust room-temperature ferroelectricity[110,142]. However, no ferromagnetic property is expected to arise in CIPS since neither the Cu nor the In cations own a partially filled *d* orbital. Notably, introducing magnetic Cr cations to the

metal thiophosphate system offers the possibility of achieving low-dimensional multiferroicity in $CrCuP_2S_6$ (CCPS). Similarly, the structure of CCPS consists of an octahedral framework defined by sulfur atoms and filled by P-P pairs, Cu, and Cr atoms. It has been proposed by earlier theoretical studies that ferromagnetic order could exist in 2D CCPS as the ferromagnetic state of monolayer CCPS is always more stable than the antiferromagnetic and paramagnetic states[143]. CCPS was shown to exhibit in-plane electrical and magnetic anisotropies and also the coexistence of antiferromagnetic and antiferroelectric orderings below the Néel temperature (32 K)[95,96,144,145]. According to Cajipea et al.[146], depending on the temperature, the Cu cations can occupy different sites including the center and off-centered sites within the sulfur octahedral and even the sites into the interlayer spacing. At T>190 K, CCPS features a nonpolar paraelectric configuration with an even distribution of Cu ions at the up and down positions within the sulfur framework. Lai et al.[97] reported modest ferroelectric behaviors in CCPS flakes at room temperature, and they proposed that the polarization might originate from the electrical-driven Cu ions on the same side of the CCPS layers. Nevertheless, there is limited evidence to support the existence of ferroelectric properties at room temperature, and the origin of this emerging ferroelectricity has not yet been identified.

Prior experimental findings on metal thiophosphate materials motivated the

exploration and verification of the presence of robust ferroelectricity in ultrathin CCPS layers. Therefore, it is crucial to delve into the nature of ferroelectric ordering in intrinsic vdW layered CCPS to fully comprehend the underlying physical mechanism and explore novel opportunities for implementing the multiple properties of CCPS in a variety of applications.

## 4.2 Crystal structure characterization of CCPS nanoflakes

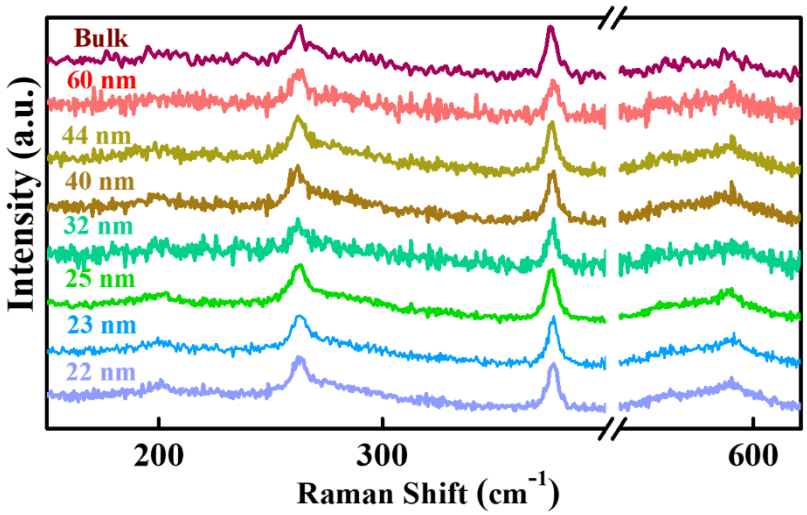


**Figure 4.1** Raman spectra of exfoliated CCPS samples with different thicknesses, measured under ambient conditions.

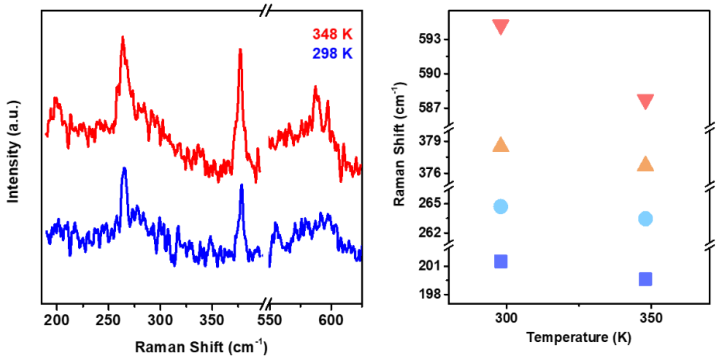


**Figure 4.2** Raman spectra of exfoliated CCPS at the temperature of 298 K and 248 K, respectively.

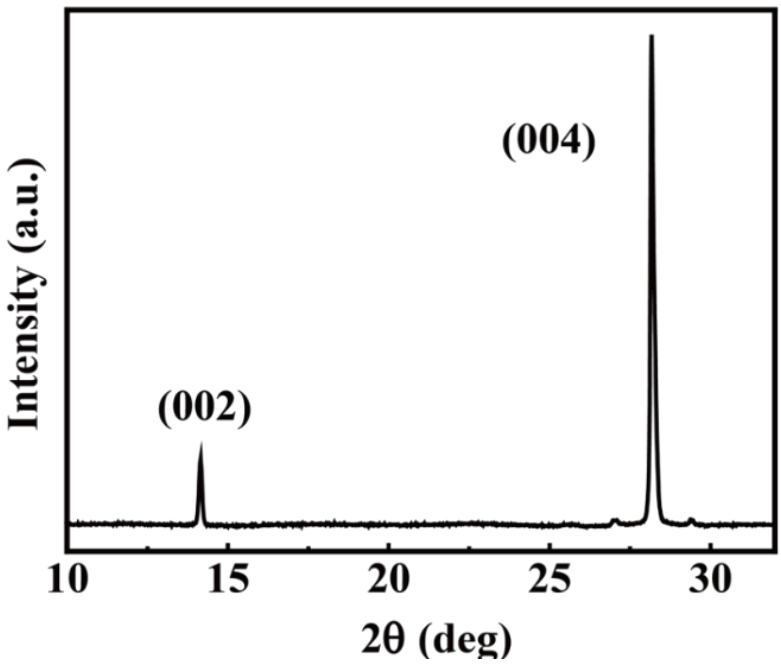


**Figure 4.3** XRD spectrum of CCPS single crystal, conducted under ambient conditions.

To investigate the quality and crystal structure of CCPS utilized in this study, Raman spectroscopy, XRD, and TEM techniques were employed. The Raman spectra of exfoliated CCPS nanoflakes measured at ambient temperature with thicknesses ranging from 22 nm to bulk crystal are shown in Figure 4.1[147]. The thickness of the CCPS nanoflakes selected for Raman analysis is larger than 20 nm since the samples with thicknesses below 20 nm illustrate a weak and indistinguishable Raman peak intensity, while increasing the integration time and/or laser power would cause damage to the ultrathin CCPS samples. From the Raman spectra of CCPS, four dominant peaks are observed that correspond to the numerous vibration modes of the $[P_2S_6]^{4-}$ anion framework. The position of the Raman peaks of the CCPS nanosheets at different

thicknesses show no obvious variations, in good agreement with the vibration modes of CCPS reported previously[148]. Furthermore, the Raman spectra of CCPS nanoflakes at ambient temperature and above their Curie temperature were also measured and plotted in Figure 4.2. The four distinguishable vibration modes reduce slightly in frequency when the temperature increases from 298 K to 333 K. This observation is in good agreement with other conventional materials in which the of the Raman peak frequency decreases with increasing temperature[149].

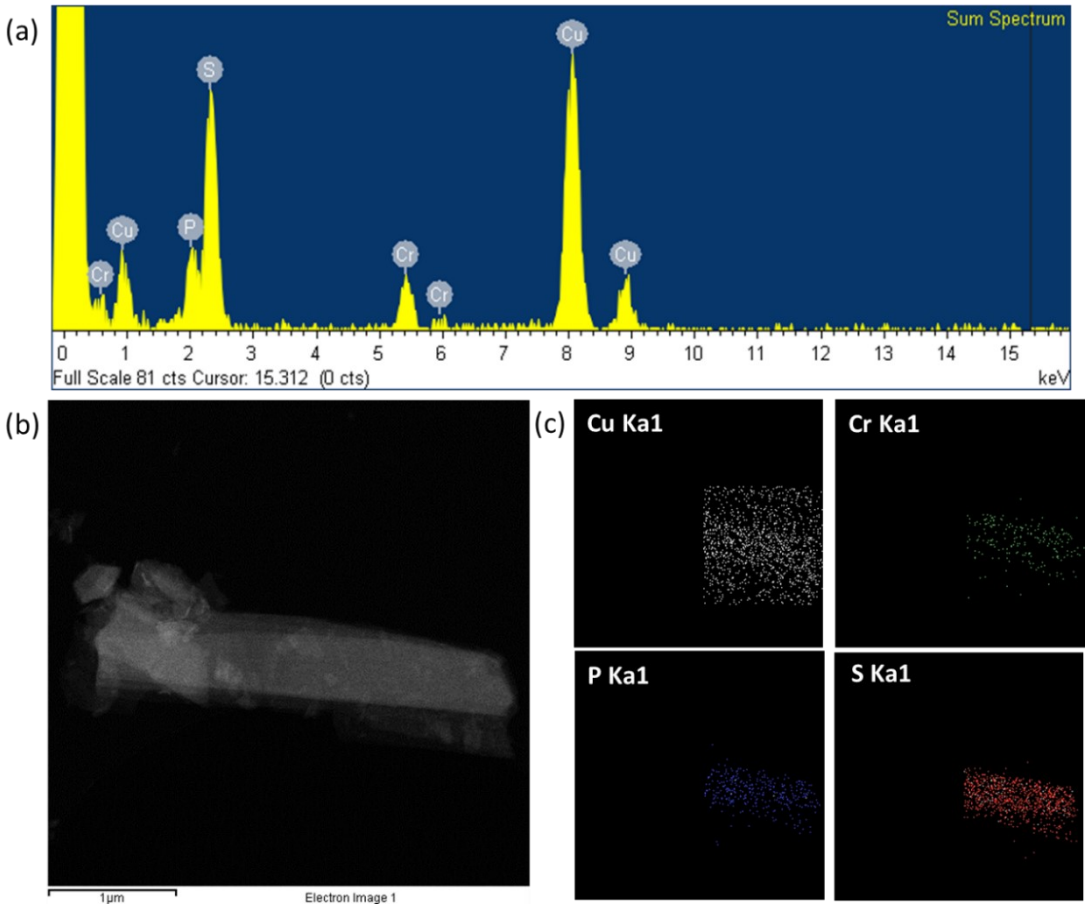


**Figure 4.4** EDX spectrum and elemental mapping of mechanically exfoliated CCPS sample.

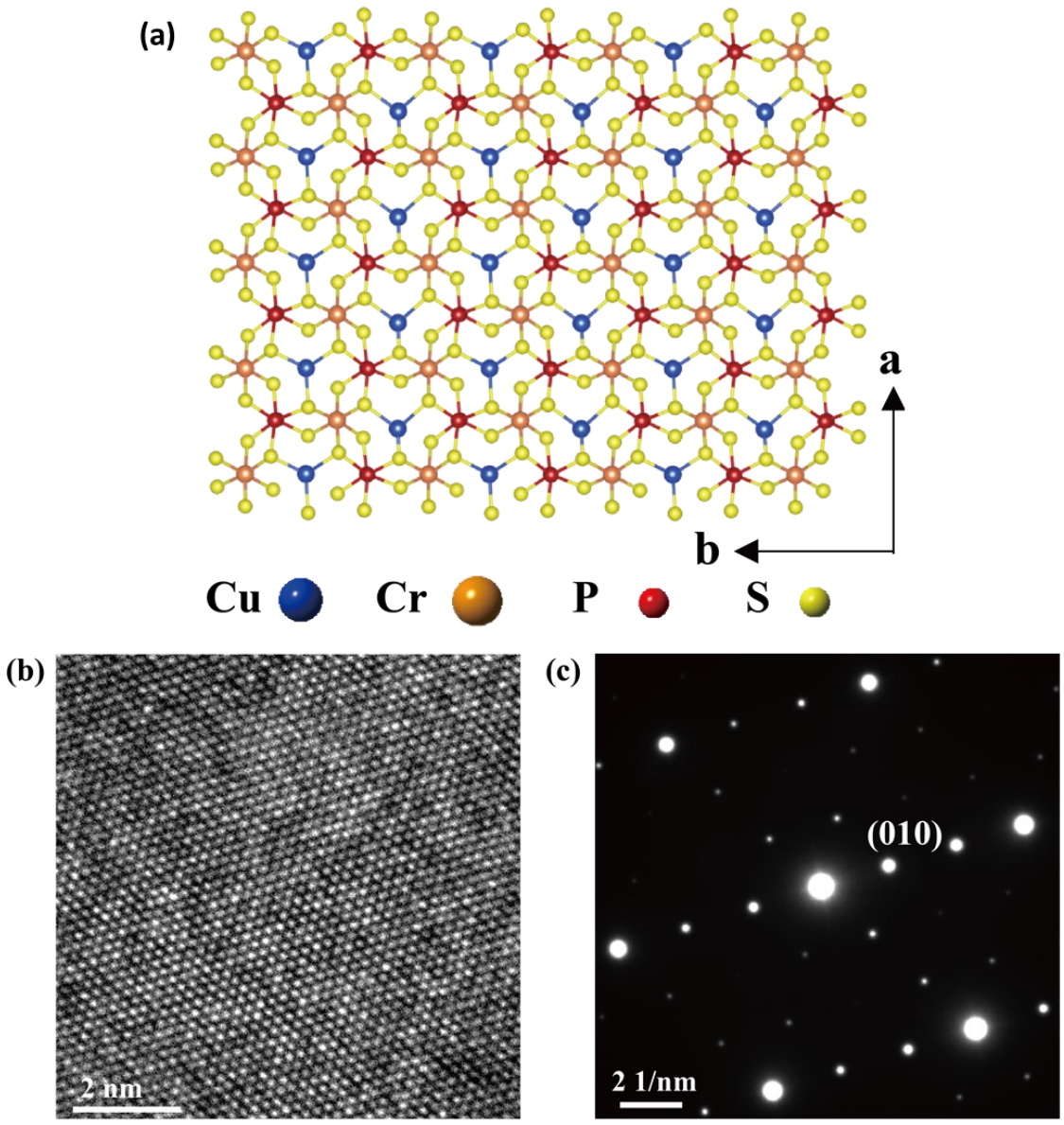


**Figure 4.5** (a) Top-view atomic structure of CCPS. (b) HRTEM image and (c) corresponding SAED pattern of CCPS.

The XRD spectrum of CCPS crystal of Figure 4.3 shows two sharp peaks at 14.35° and 28.35°, corresponding to the (002) and (004) planes, respectively, and denoting a high single crystallinity along the c-axis. Figure 4.4 presents the EDX analysis and elemental mapping of CCPS, verifying the four elements existing in CCPS. Figure 4.5a

shows the schematic top-view atomic structure of CCPS. The CCPS consists of hexagonal sulfur frameworks where the octahedral centers are occupied by Cu, Cr cations, and P-P pairs forming periodic triangular patterns. The HRTEM image of CCPS in Figure 4.5b displays the in-plane lattice structure with uniform and periodic crystal lattices along identical orientations, with a lattice spacing of approximately 0.58 nm. The SAED pattern in Figure 4.5c signifies the large-scale single crystallinity of the CCPS crystal utilized in this work.

## 4.3 Room-temperature ferroelectricity 2D CCPS nanoflakes

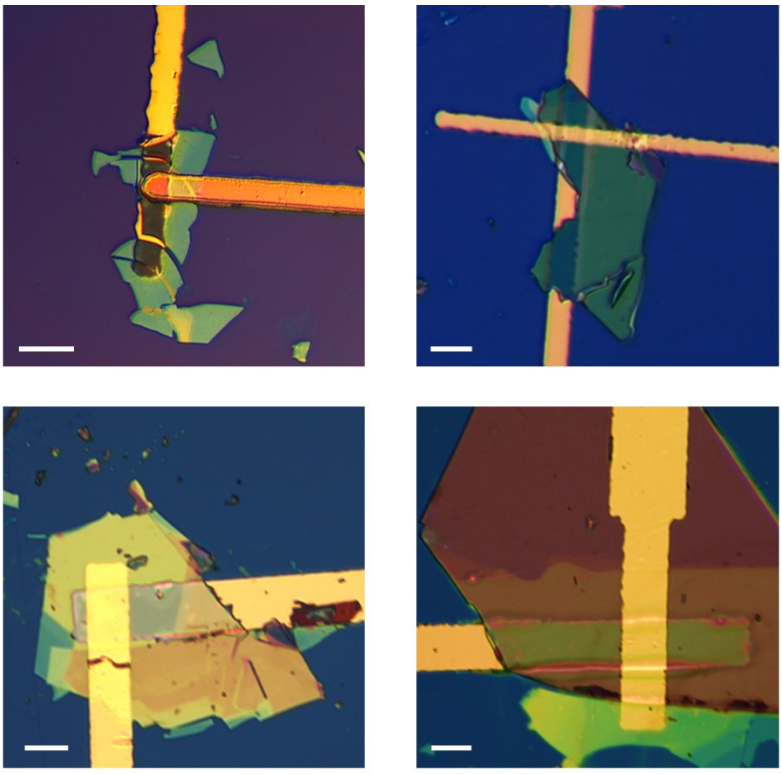

**Figure 4.6** Optical microscopy images of several prototype vertical Au/CCPS/Au device structures.

To examine the inherent ferroelectric properties of CCPS, experiments were conducted to measure the polarization-electric field (*P-E*) hysteresis. Figure 4.6 displays the optical images of some two-terminal Au/CCPS/Au vertical junction devices constructed for *P-E* hysteresis measurements. The *P-E* hysteresis loops of the exfoliated CCPS nanoflakes were performed through standard Positive-Up Negative-Down (PUND) approach, and he voltage pulse and current output in the PUND measurement are shown in Figure 4.7a. The *P-E* hysteresis loop in Figure 4.7b quantitatively examined the macroscopic spontaneous polarization of a 0.2 μm CCPS flake. A typical ferroelectric *P-E* hysteresis loop was obtained, revealing moderate remnant polarization and saturation polarization of approximately 14.97 and 16.05 μC $cm^{-2}$, respectively. Intriguingly, the measured spontaneous polarization of CCPS at room temperature was found to be higher than that of CIPS in previous studies [92,107].

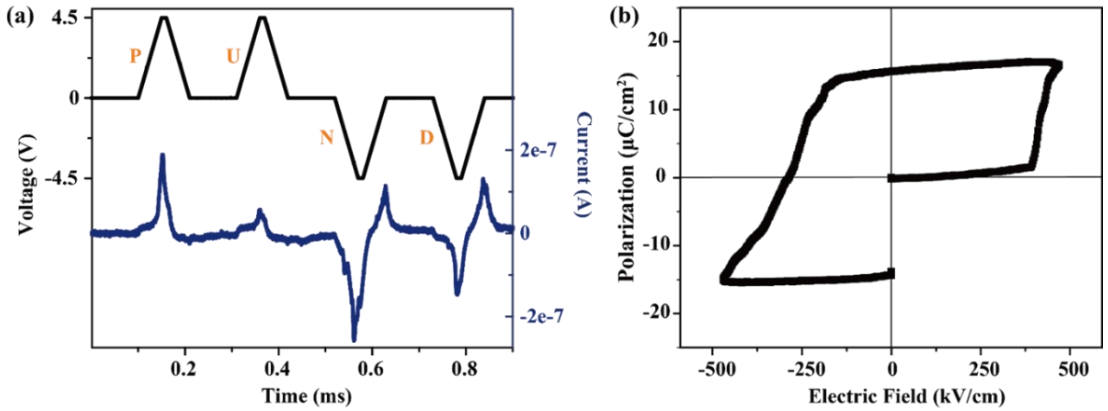


**Figure 4.7** *P-E* hysteresis measurement of CCPS**.** (a) Voltage pulses (black) and current output (blue) in the PUND measurement. (b) Calculated *P-E* hysteresis loop of 0.2 μm CCPS.

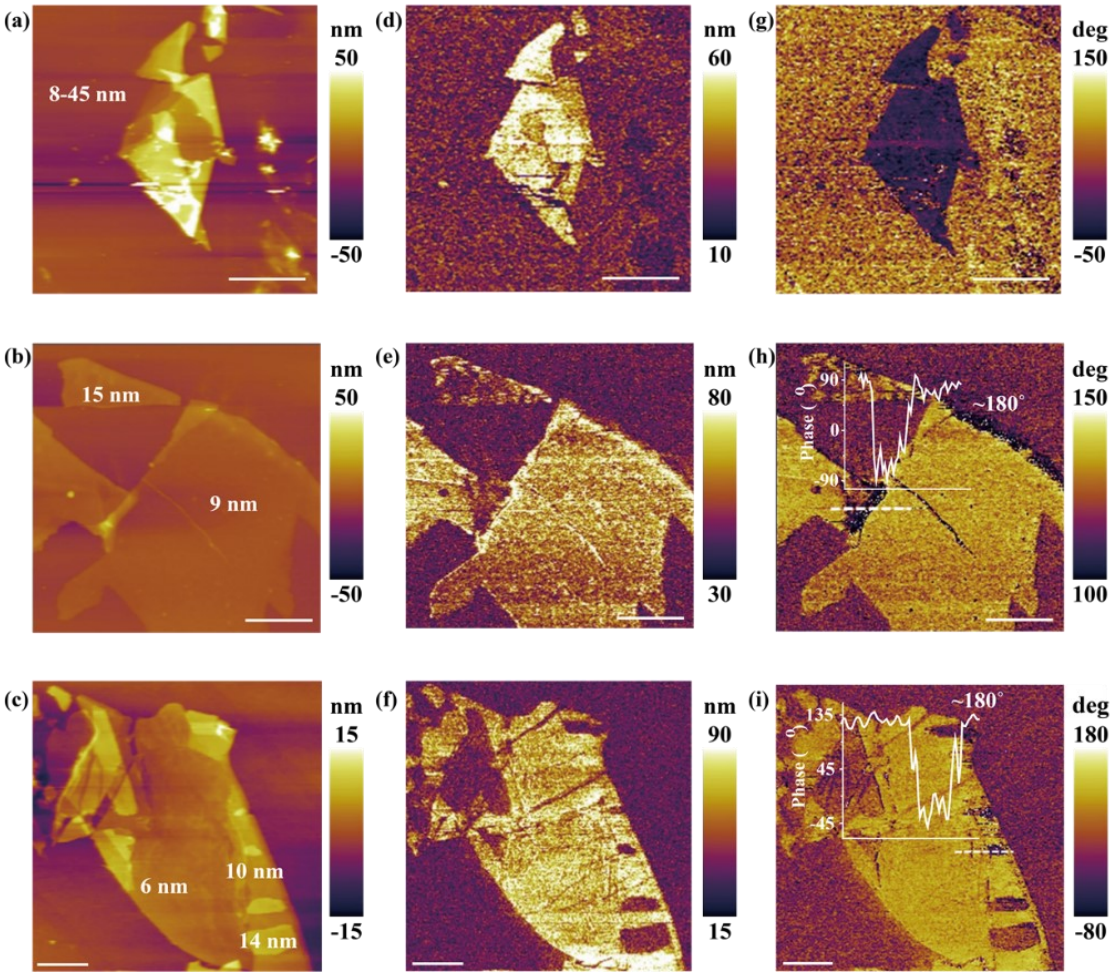


**Figure 4.8** (a)-(c) Topography of CCPS nanoflakes and the corresponding (d)-(f) amplitude and (g)-(i) phase images illustrating the ferroelectric domains as visualized by vertical PFM. Scale bar: 10 μm, 2 μm, and 1 μm, respectively.

To further investigate the ferroelectric polarization in ultrathin CCPS nanoflakes, vertical piezoelectric force microscopy (PFM) measurements were employed. These measurements allow for the examination of local electromechanical responses and the observation of different out-of-plane polarization orientations within ferroelectric

domains. Consequently, the presence of ferroelectricity at the nanoscale can be directly observed and confirmed. In order to comprehensively study the material, AFM surface topography and PFM out-of-plane piezoresponses were recorded for exfoliated CCPS nanoflakes with varying thicknesses on conductive Pt substrates. The PFM phase image in Figure 4.8g reveals that the CCPS nanoflakes exhibit the same polarization direction despite having different thicknesses. While in the other two randomly selected CCPS samples (Figure 4.8h-i), distinct areas with 180˚ phase difference can be observed across regions of varying thicknesses in the PFM phase mappings, which correspond to two vertical ferroelectric domains with opposite polarizations. These observations suggest that when CCPS nanoflakes are vertically stacked, regions with opposite polarizations can be formed, providing preliminary evidence for the existence of ferroelectricity in ultrathin CCPS.

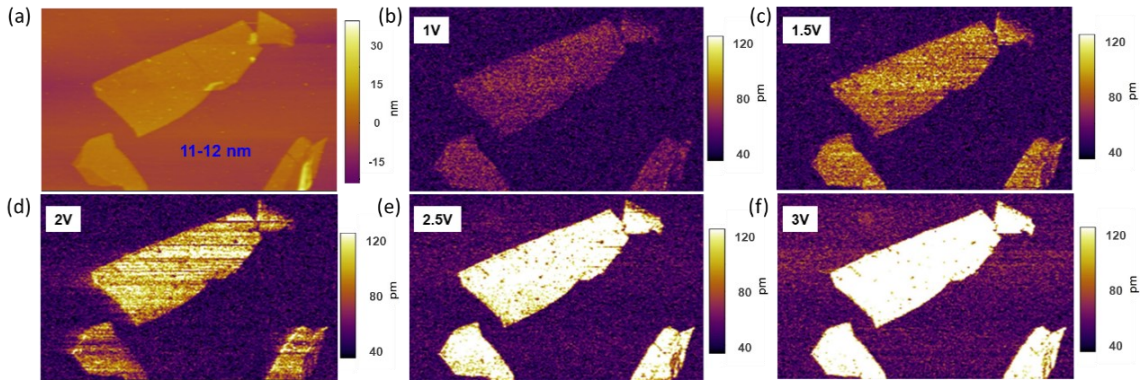


**Figure 4.9** (a) Topography (b)-(f) and out-of-plane amplitude images of CCPS nanoflakes under various AC voltages from 1 V to 3 V.

In addition, the out-of-plane piezoelectricity of ultrathin CCPS nanoflakes is primarily demonstrated by measuring the PFM amplitude responses under different driving voltages ranging from 1 V to 3 V, as shown in Figure 4.9b-f, respectively. A dominant enhancement in the piezoelectric response can be clearly observed with the increase in the driving voltage, signifying the piezoelectricity of 2D CCPS in vertical direction.

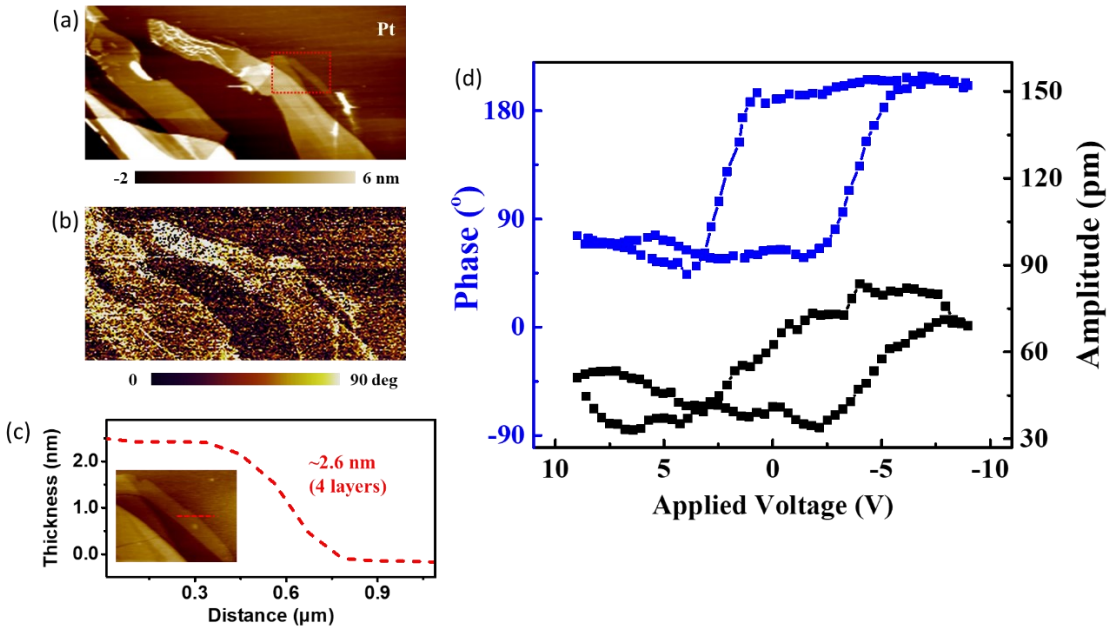


**Figure 4.10**. (a) Surface topography and (b) corresponding PFM phase images of ultrathin CCPS samples. (c) AFM height profile of a CCPS nanoflake with the thickness of ~2.6 nm, corresponding to 4 CCPS layers. (d) Off-field PFM phase and amplitude hysteresis switching of the 2.6 nm CCPS nanoflake.

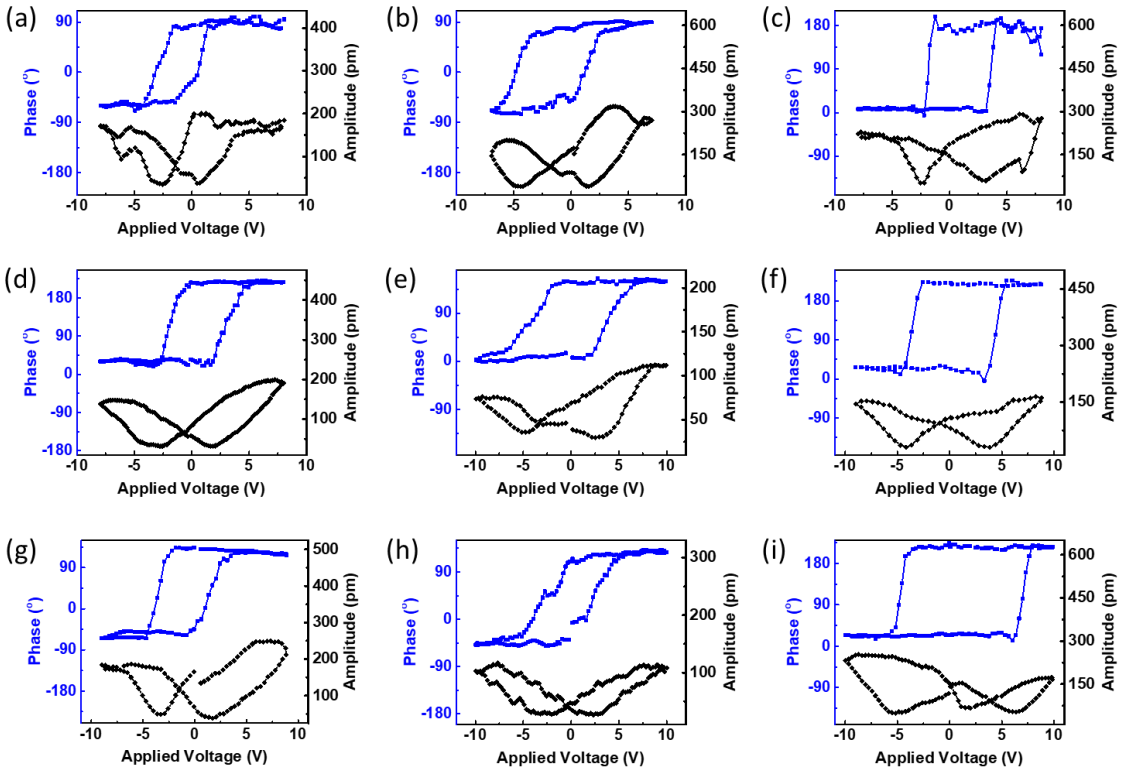


**Figure 4.11** Out-of-plane off-field PFM amplitude (black) and phase (blue) hysteresis loops of CCPS nanoflakes with the thicknesses of (a)-(i) 3.3, 5, 6, 8, 15, 20, 79, 171, and 286 nm, respectively.

It is a defining characteristic of ferroelectric materials that they exhibit a switchable polarization in response to an external electric field. Hence, local PFM switching spectroscopy measurements were conducted using conductive PFM probes to confirm the ability of electric polarization to switch with an external bias. Figures 4.10a and 4.10c present the AFM topographic image and the corresponding height profile (along the red line) of ultrathin CCPS nanoflakes, down to a thickness of approximately 2.6 nm (equivalent to 4 atomic layers). The PFM phase image in Figure

4.10b clearly shows a phase contrast between the ultrathin CCPS and the Pt substrate. PFM off-field hysteresis loops were measured on the quadruple-layer CCPS nanoflake (Figure 4.10d), illustrating typical ferroelectric responses characterized by a butterfly-shaped amplitude loop and a phase switching of 180° difference. Figure 4.11 displays additional out-of-plane PFM off-field phase (blue) and amplitude (black) responses of the CCPS samples with respect to the applied sweeping voltages, covering a range of sample thicknesses from a few nanometers to a few hundred nanometers. In these local hysteresis measurements, distinct 180° phase differences and asymmetric butterfly-shaped hysteresis loops were consistently observed in the off-field PFM phase and amplitude responses, respectively. These findings indicate that out-of-plane ferroelectricity in CCPS is maintained even down to few-layer thickness. In order to exclude any possible non-ferroelectric signals that could appear during the local PFM measurements, the off-field hysteresis loops were investigated under different sweeping voltages and different measuring frequencies, as displayed in Figures 4.12a and 4.12b, respectively. The local off-field PFM amplitude and phase loops verify the existence of coercive voltage for switching the polarity of CCPS nanoflakes. While the coercive voltage is not affected by the driving frequency of the sweeping voltages applied during the hysteresis measurements.

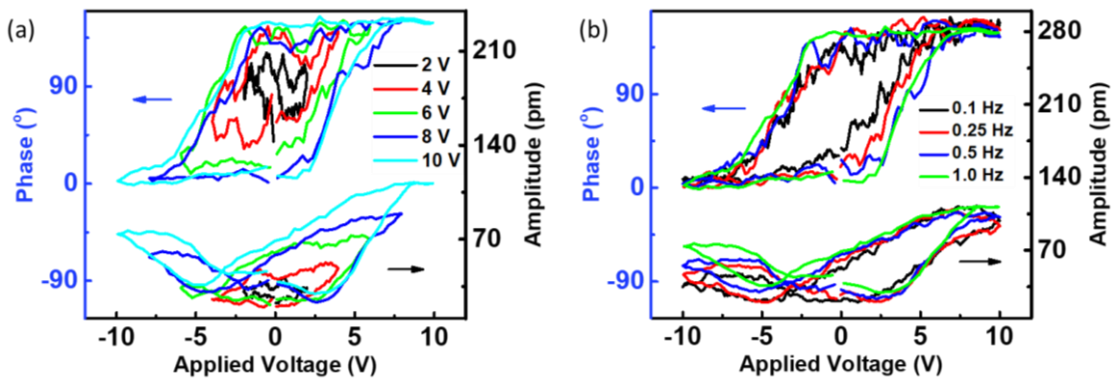


**Figure 4.12** Out-of-plane off-field PFM hysteresis loops with (a) different DC voltage sweeps and (b) different measuring frequencies.

The coercive field ($E_C$) for polarization switching was determined from the PFM off-field hysteresis loops of the CCPS samples and plotted against the film thickness in Figure 4.13. The coercive field decreases proportionally, following a double logarithmic scale, as the sample thickness (t) increases, whereas the relationship between $E_C$ and t can be described by the equation $E_C \propto t^{-0.929}$. Notably, the experimental scaling exponent value deviates from the Janovec–Kay–Dunn (JKD) scaling ($E_C \propto t^{-2/3}$), while similar deviations have also been reported in other ferroelectric thin films[150,151]. Several studies also suggested a more general inverse power-law relationship between $E_C$ and t[152]. For example, the coercive field can be influenced by factors such as interfacial "dead layers" and the depolarization field effect, in which the coercive field can enhance as the thickness decreases[153,154].

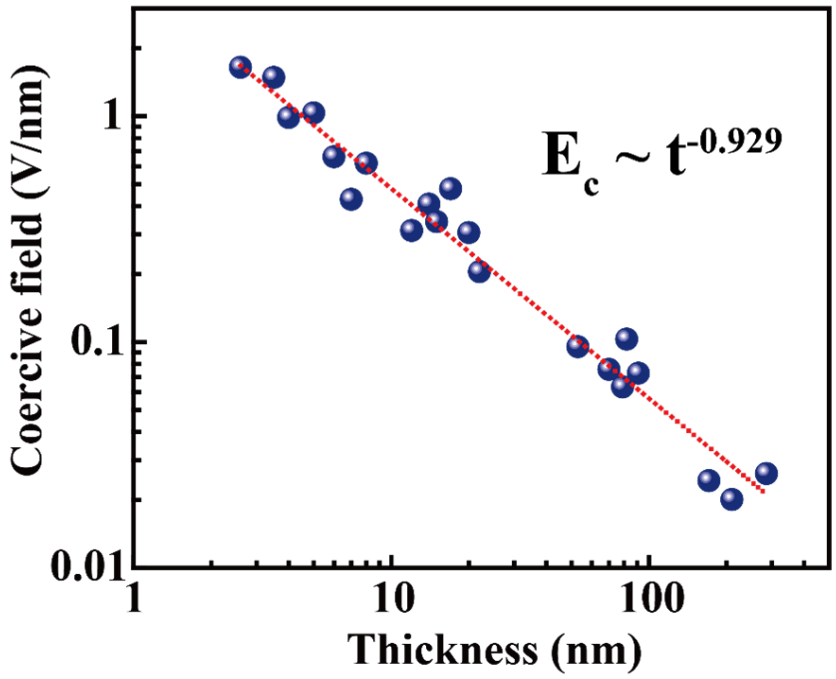


**Figure 4.13** Thickness dependence of the ferroelectric coercive field of CCPS nanoflakes in double logarithmic scale.

It's worth noting that all PFM measurements in this study were conducted under ambient conditions, and certain factors including potential parasitic capacitance could lead to undesired voltage drops at the interface between the conductive PFM tip and CCPS, thereby increasing the coercive field. Also, the effect of ion migration in CCPS may also impact on the thickness dependence of the coercive field, potentially resulting in a larger exponent value in the scaling of the coercive field. A more detailed explanation of these phenomena would require further investigation, which is crucial for exploring and comprehending the underlying physical mechanisms of newly discovered 2D ferroelectric materials.

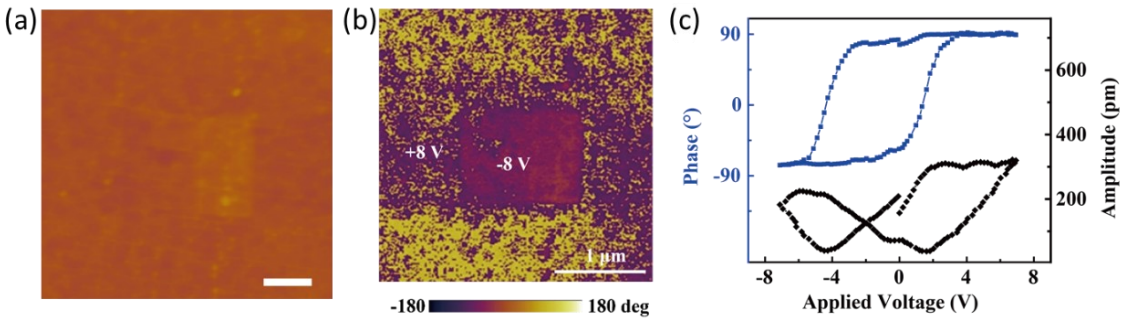


**Figure 4.14** (a) AFM topography, (b) ferroelectric domain modification imaged by PFM phase mapping by writing box patterns with ± 8 V, and (c) the corresponding PFM off-field phase and amplitude hysteresis loops of a 12 nm CCPS nanoflake.

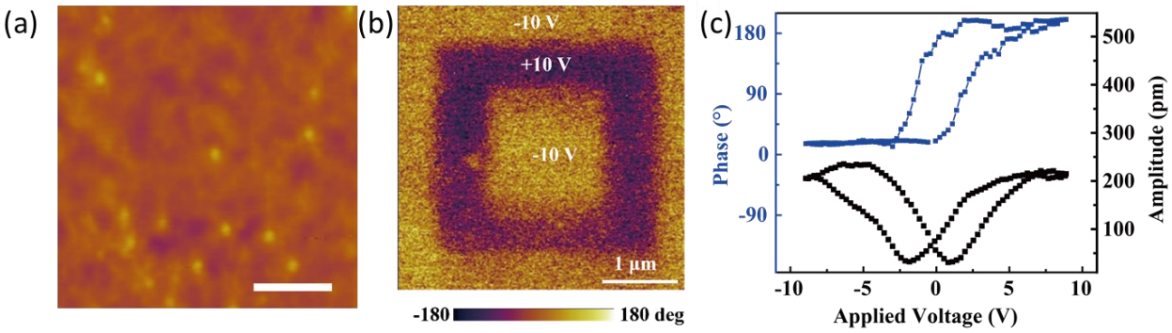


**Figure 4.15** (a) AFM topography, (b) ferroelectric domain modification imaged by PFM phase mapping by writing box patterns with ± 10 V, and (c) the corresponding PFM off-field phase and amplitude hysteresis loops of a 25 nm CCPS nanoflake.

Furthermore, the verification of intrinsic ferroelectricity on a large scale is extended by modifying the ferroelectric domain pattern of CCPS nanoflakes. By applying an external electric field using conductive PFM tips, square patterns with a phase contrast of 180° are successfully written on CCPS nanoflakes of varying

thicknesses, as depicted in Figures 4.14, 4.15, and 4.16. The corresponding off-field PFM phase (blue) and amplitude (black) hysteresis responses of these CCPS nanoflakes were also recorded and presented. It should be noted that the extraction of Cu ions and their deposition on the sample surface can cause morphology changes, which may result in small fluctuations in the PFM phase responses[144]. As shown in Figures 4.14a, 4.15a, and 4.16a, no significant damage or surface protrusions are identified in the topography of these nanoflakes after the domain modification test. During the characterization process, all samples were grounded, thereby eliminating potential contributions from non-ferroelectric artifacts including ion migration and surface charges.

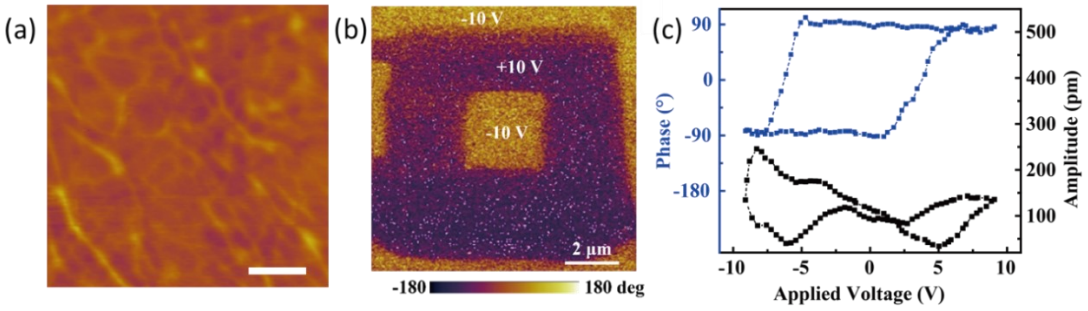


**Figure 4.16** (a) AFM topography, (b) ferroelectric domain modification imaged by PFM phase mapping by writing box patterns with ±10 V, and (c) the corresponding PFM off-field phase and amplitude hysteresis loops of an 82 nm CCPS nanoflake.

Furthermore, the PFM technique was employed to directly observe the variations in the ferroelectric domain of CCPS nanoflakes at different temperatures. A

representative 2D CCPS nanoflake with a thickness of 15 nm (Figure 4.17) was selected for the temperature-dependent investigation and was heated from room temperature up to 338 K. As shown in Figure 4.18, the contrast in the PFM phase slightly reduces as the CCPS nanoflake was heated to 318 K. When the temperature surpasses 333 K, which is above the Curie temperature of CCPS, the ferroelectric domain vanishes completely. When the temperature decreases below the Curie temperature ($T < 333$ K), the ferroelectric domain reappears. Such experimental observation of ferroelectric domain changes at different temperatures provides strong evidence for the reversible transition between the ferroelectric and paraelectric phases of 2D CCPS.

To explore the non-centrosymmetric structure of the CCPS crystal, effective and non-destructive SHG technique was employed. The spectra depicted in Figure 4.19a, exhibit distinct SHG peaks at half the wavelength of the 900 nm excitation laser, denoting the non-centrosymmetric nature of CCPS for its intrinsic ferroelectricity. As shown in figure 4.19b, the intensity of the SHG signal decreases significantly as the temperature rises above room temperature, with the intensity at 328 K dropping to less than 10% relative to that at room temperature. This suggests a gradual loss of spontaneous polarization in CCPS and a possible transition from a ferroelectric to a paraelectric phase near the Curie temperature, which is a characteristic feature of ferroelectric materials[92].

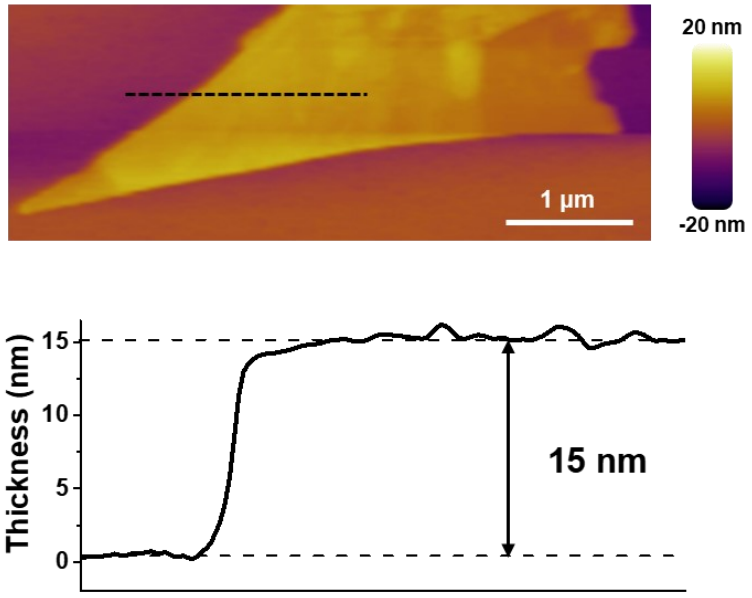


**Figure 4.17** AFM topography and height profile of the CCPS sample for temperature-dependent ferroelectric domain observation.

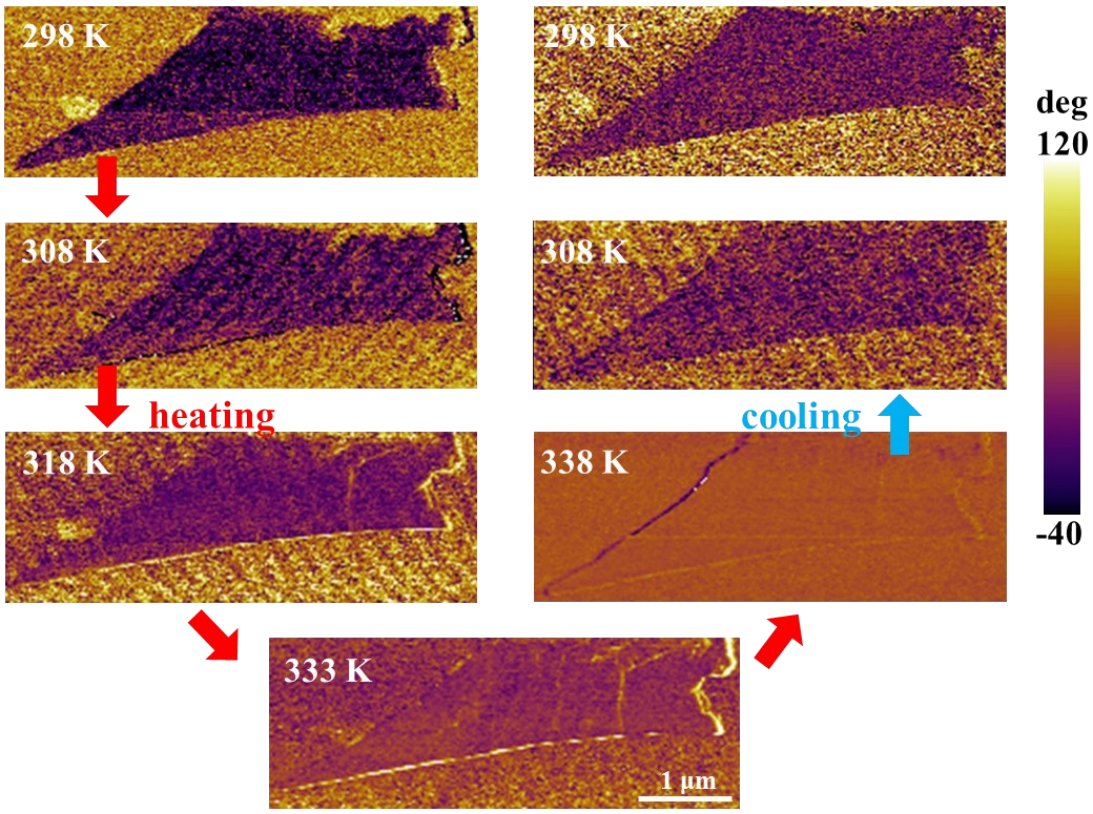


**Figure 4.18** Temperature-dependent observation of the ferroelectric domain in CCPS nanoflake from room temperature to 338 K and returns to room temperature.

Importantly, it should be emphasized that all the *P-E* hysteresis measurements, PFM, and SHG analyses were performed under ambient conditions. These investigations, using both macroscopic and microscopic approaches, consistently reveal the presence of spontaneous electric polarization along the vertical direction in CCPS from bulk crystal to few-layer thickness. The results confirm the existence of stable out-of-plane ferroelectricity in single-crystalline vdW CCPS layers at room temperature.

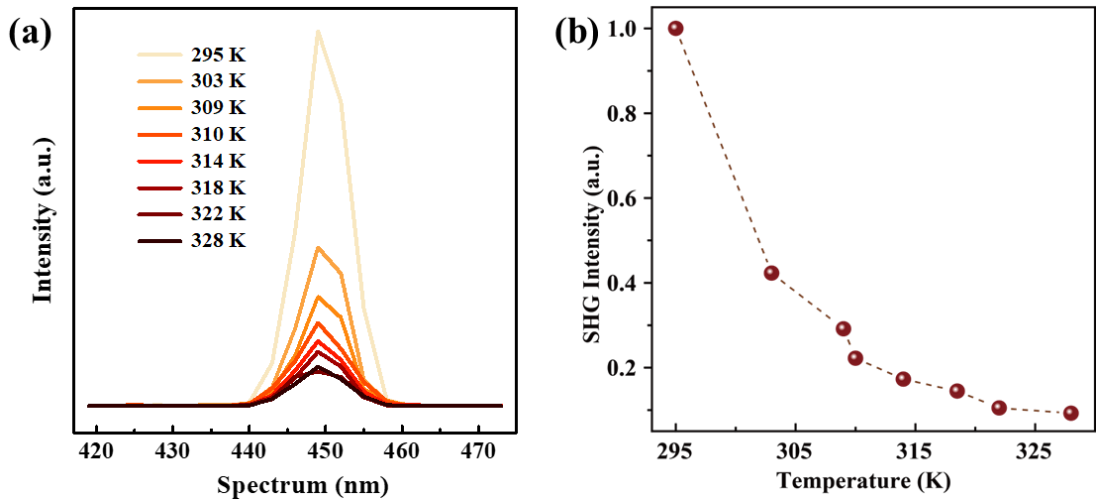


**Figure 4.19** (a) SHG signals measured from exfoliated CCPS samples at various temperatures and (b) the temperature-dependent SHG peak intensities.

## 4.4 Origin of the intrinsic out-of-plane ferroelectricity in CCPS

Previous studies on CCPS have suggested that the ferroelectric behavior may be primarily attributed to the arrangement of Cu ions within the CCPS layers[95,97,143].

However, direct microscopic evidence supporting the ferroelectric mechanism have been lacking. In this study, aberration-corrected STEM was employed to examine the atomic structure of pristine CCPS direct prepared through mechanical exfoliation from the parent crystal. The focus of the STEM investigation was on identifying the locations of Cu ions within the CCPS layers and exploring the origin of the room-temperature ferroelectricity.

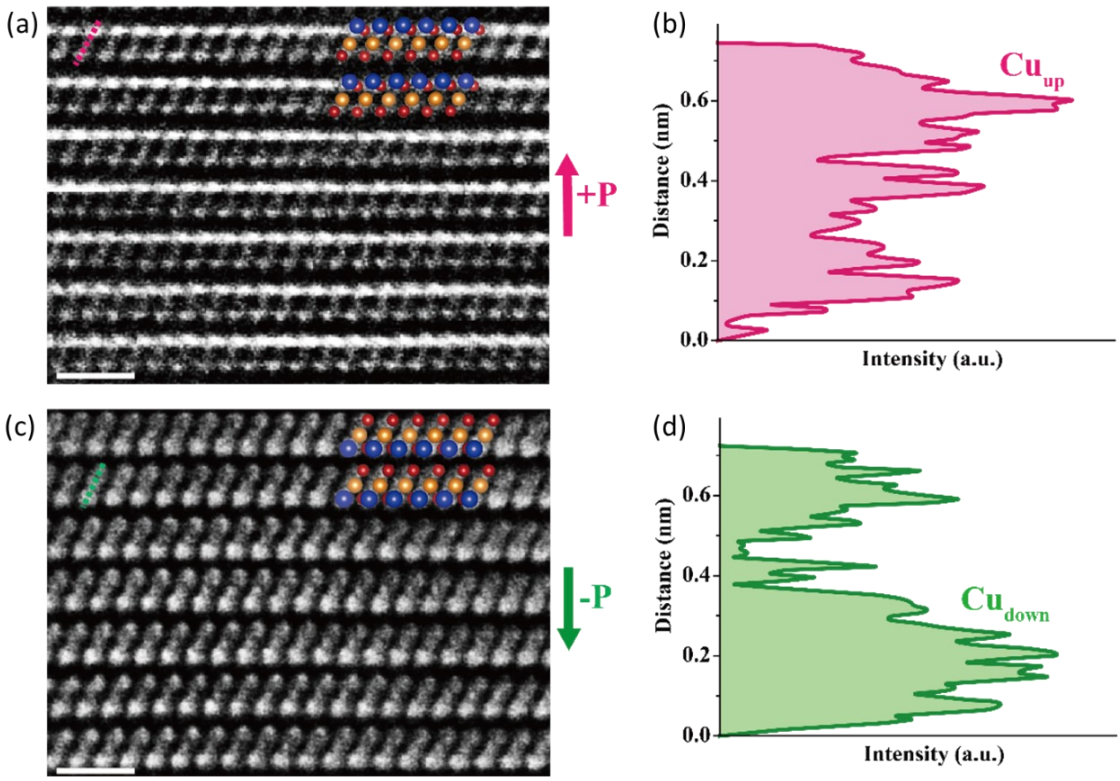


**Figure 4.20** Atomically resolved HAADF-STEM images of the cross-section of CCPS with (a) positive and (c) negative spontaneous polarization, respectively. Scale: 1 nm. (b)-(d) Z-contrast intensity profiles along the dashed lines corresponding to (a) and (c), respectively.

High-angle annular dark-field (HAADF) imaging technique was mainly utilized to achieve atomic-resolution cross-sectional imaging of the crystal structure. HAADF imaging is highly sensitive to the variations in the atomic number (Z) of elements in a material, thus Cu element in CCPS with the highest atomic number should appear the brightest with most intense signals in the HAADF-STEM images. The HAADF-STEM images presented in Figures 4.20a and 4.20c provide direct evidence of the two opposite ferroelectric polarizations in CCPS, in which the brightest Cu atoms are consistently observed to be located at the up (down) sites of each vdW CCPS layer. This arrangement induces a non-zero electric polarization in the upward (downward) direction. The corresponding intensity profiles along the dashed lines in Figures 4.20a and 4.20c are shown in Figures 4.20b and 4.20d, respectively, further confirming the positioning of Cu atoms at the up/down sides within one CCPS layer. According to previous literature and our optimized structural model, ferroelectric CCPS monolayer crystallizes in the P1 symmetry[155]. The HAADF-STEM results are consistent with our proposed structural model as illustrated in Figure 4.23a and provide convincing evidence for the intrinsic ferroelectricity originating from the different off-center orderings of Cu ions in CCPS.

Furthermore, the temperature of the CCPS sample was raised above its Curie temperature to observe the arrangement of Cu ions in the paraelectric phase. In atomic-

resolution HAADF-STEM image of Figure 4.21, paraelectric phase CCPS is demonstrated while the intensity of the Z-contrast reveals the Cu ions to be partially occupied evenly at both the up and down sites of the CCPS layer, leading to a zero net spontaneous polarization. This finding is well-agreed with the structural characteristics of CCPS in the paraelectric phase reported previously, with the space group of *Pc*[146,148].

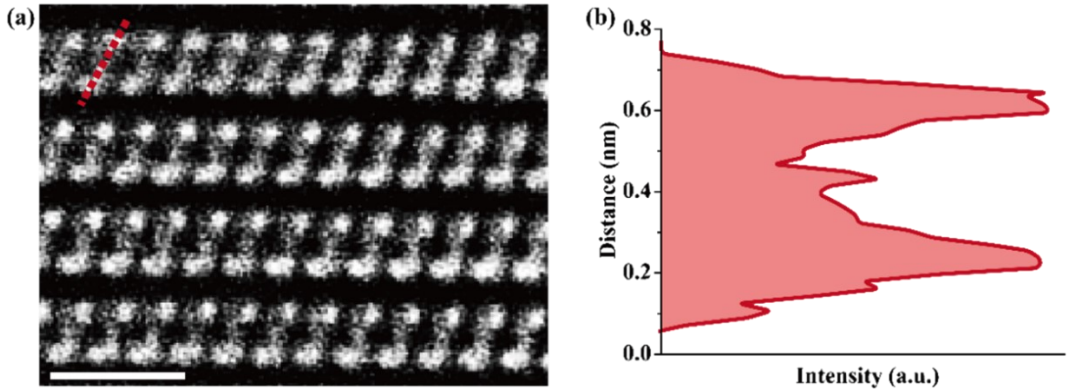


**Figure 4.21** (a) Atomic resolution HAADF-STEM image of paraelectric phase CCPS and (b) the corresponding intensity profile along the dashed line. Scale: 1 nm.

The estimated average thickness of a single-layer CCPS is approximately 6.34 Å, which is smaller than that of the paraelectric phase CCPS at room temperature, as noted in previous literature[148]. The similarities between CCPS and CIPS, including their identical $[P2S6]^{4-}$ anion frameworks and Cu cations, allow us to compare and understand the structural characteristics of CCPS by referring to the more extensively studied ferroelectric CIPS. According to the literature, the transition to the ferroelectric phase in CIPS is accompanied by a contraction of the lattice, which can be attributed to

the positioning of Cu cations on only one side of the ferroelectric CIPS layer, thus reducing electrostatic repulsion[156]. Similarly, it is proposed that the difference in layer spacing between the ferroelectric phase CCPS in this study and the paraelectric phase CCPS reported in previous literature is due to a decrease in electrostatic repulsion resulting from the confinement of Cu cations to one side of the CCPS layers.

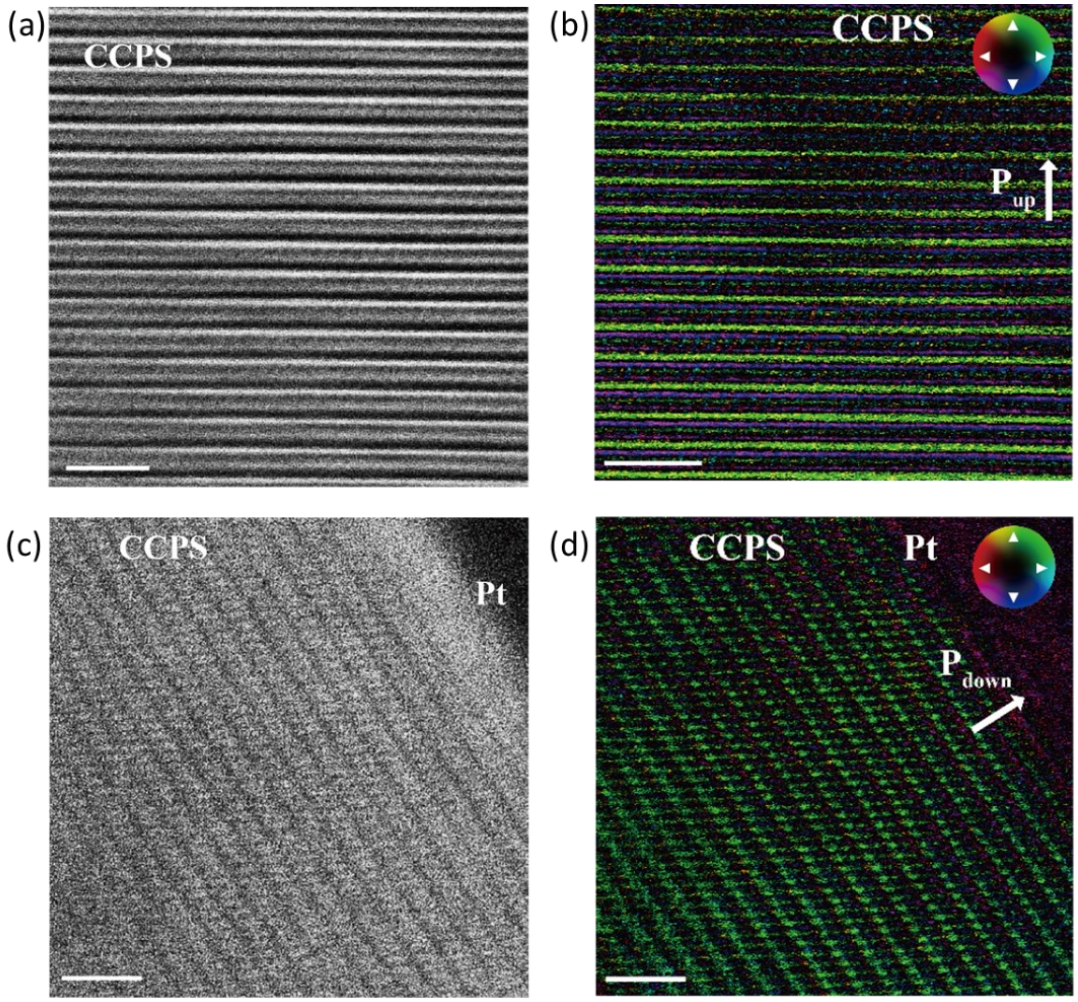


**Figure 4.22** (a) (c) HAADF-STEM images, and the corresponding colored DPC-STEM images indicating uniform (b) upward and (d) downward electric polarization fields in CCPS. Scale: 2 nm.

On the other hand, the differential phase contrast (DPC) imaging technique of STEM is sensitive to atomic-scale electric fields and can be employed to visualize the polarization field in ferroelectric materials[157]. Figure 4.22 illustrate the HAADF-STEM and corresponding colored DPC images of CCPS samples with upward and downward polarizations, respectively. The inset color wheel in the DPC images specifies the direction of local electric polarization, providing direct evidence of intrinsic ferroelectricity in CCPS. Figure 4.22b shows a uniform upward electric polarization field (green-yellowish color), while Figure 4.22d depicts a CCPS sample exfoliated on Pt substrate which clearly illustrates a polarization field directed from the CCPS layers towards Pt (blue-greenish color), representing a downward electric polarization. The microscopic characterization results indubitably validated the ferroelectric phase CCPS as a stable configuration in an ambient environment.

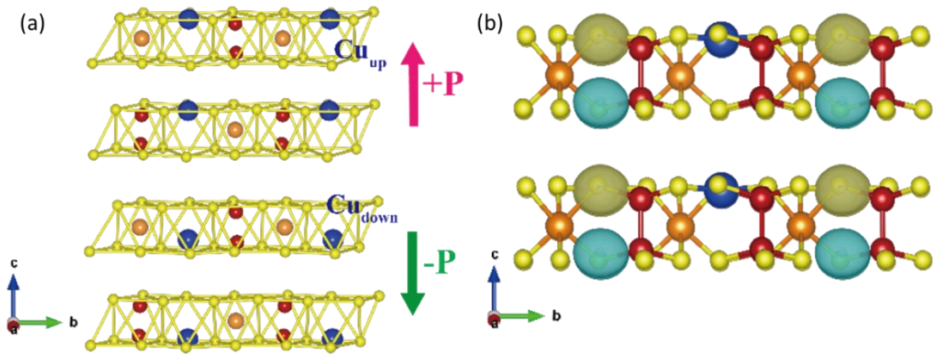


**Figure 4.23** (a) Atomic model of CCPS with out-of-plane ferroelectricity. (b) Charge density difference between the ferroelectric and the paraelectric phase CCPS, the yellow and cyan region represents excess and depletion of charges respectively.

In addition to STEM analyses, further insights into the charge density difference between the ferroelectric and paraelectric phases of CCPS were obtained through density-functional theory (DFT) simulations. Regarding the observed partial Cu occupation in the paraelectric phase CCPS by STEM, a representative atomic structure was chosen based on comparing the total energies of various possible Cu configurations. To determine the potential atomic configurations, the coordinates of the Cu ions were specified and 12 different configurations within a 2 × 2 × 1 supercell were considered. All of the simulated CCPS structures with various Cu ion orderings exhibit very similar total energies ($E_i$) of approximately -390 eV, indicating the presence of disordered partial Cu occupations. Although the differences were small, the CCPS structure with alternating off-centered Cu locations demonstrates the lowest $E_i$ value of -391.67 eV. Therefore, this structure was chosen as the representative paraelectric structure for the calculation of the charge density difference. Subsequently, the charge density difference ($\Delta\rho(r)$) between the ferroelectric and the paraelectric phase of CCPS was plotted by subtracting the charge densities: $\Delta\rho(r) = \rho_{ferro}(r) - \rho_{para}(r)$, where $\rho_{ferro}(r)$ and $\rho_{para}(r)$ represent the total charge densities of the ferroelectric and paraelectric CCPS phases, respectively[158]. In Figure 4.23b, the yellow and cyan regions refer to an excess and depletion of charges, respectively. The plot reveals a net electric dipole along the vertical direction, which is consistent with the pervious experimental findings in

this study and supports the presence of intrinsic out-of-plane ferroelectricity in the vdW layered CCPS structure.

## 4.5 Summary

To summarize, the presence of robust ferroelectricity in the 2D vdW layered CCPS at room temperature is revealed, and the origin of the ferroelectric behavior is examined from an atomic perspective. The spontaneous polarization of CCPS is quantitatively determined to be approximately 16.05 μC $cm^{-2}$, and switching of the electric polarization is demonstrated in CCPS nanoflakes with a minimum thickness of 2.6 nm. Furthermore, the out-of-plane ferroelectricity is identified to be arising intrinsically from the off-center ordering of the Cu ions to the same side within the vertical layer, resulting in a non-zero spontaneous polarization that can be modulated by an external electric field. These findings provide valuable insights into the fundamental understanding of the room-temperature ferroelectricity in vdW layered CCPS, and open up new possibilities for the development of multifunctional nanodevices.

# Chapter 5 Nanoelectronic Devices based on 2D Ferroelectric CCPS

## 5.1 Introduction

Taking advantage of dangling bond-free surfaces and weak van der Waals (vdW) interlayer interactions, two-dimensional (2D) materials can be easily integrated into vdW heterostructures and are highly promising for a variety of nanoelectronic applications. In order to demonstrate the potential of ferroelectric $CrCuP_2S_6$ (CCPS) for non-volatile memory and other nanoelectronic device integrations, different types of devices, including ferroelectric tunneling junction (FTJ), vertical ferroelectric diode (VFD), and ferroelectric field-effect transistor (FeFET), were fabricated and their performance were analyzed in this chapter.

## 5.2 Electronic structure of CCPS

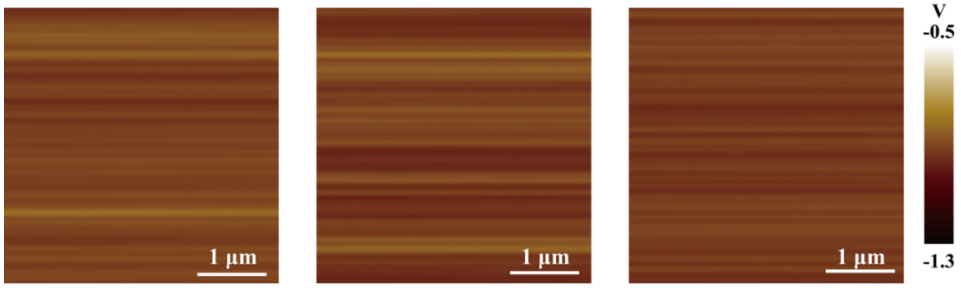


**Figure 5.1** SKPM potential mappings of freshly cleaved HOPG surface at several randomly selected areas. The $V_{CPD}$ are -0.868 V, -0.847 V and -0.870 V, respectively.

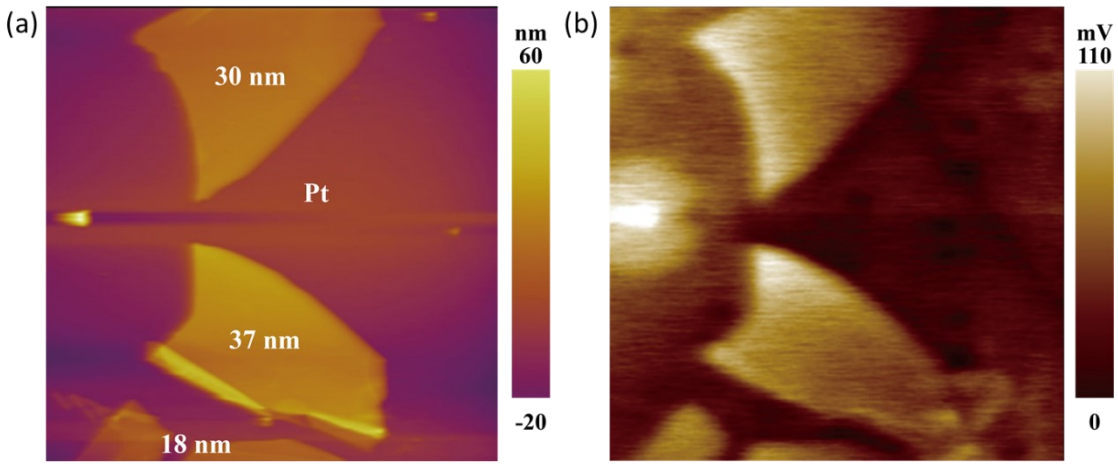


**Figure 5.2** SKPM characterization of CCPS nanoflakes. (a) Surface topography and (b) surface potential mapping of CCPS nanoflakes exfoliated on Pt substrate.

Scanning Kelvin probe microscopy (SKPM) measurements was used to determine the surface potential and estimate the Fermi level of CCPS nanoflakes. For the calculation, the work function of the conductive Pt/Ir-coated tip used during the SKPM measurement was calibrated. Figure 5.1 displays the SKPM mappings of a highly ordered pyrolytic graphite (HOPG) substrate as a reference. The contact potential differences ($V_{CPD}$) between the Pt/Ir-coated tip and HOPG were measured to be around -0.862 V on average. Since the work function of freshly cleaved HOPG is around 4.6 eV, the work function of the Pt/Ir-coated tip $\phi_{Pt/Ir}$ was calculated by $\phi_{HOPG} - eV_{CPD(HOPG)}$ to be 5.462 eV. The SKPM measurement on CCPS nanoflakes of Figure 5.2 shows a $V_{CPD}$ of about 75 mV relative to the Pt/Ir-coated tip. Therefore, the work function of the CCPS nanoflakes $\phi_{CCPS}$ was calculated as $\phi_{Pt/Ir} + eV_{CPD(CCPS)}$ to be 5.54 eV. The band structure and density of states (DOS) of CCPS were calculated by DFT

simulations, as shown in Figure 5.3. The calculations indicate that the band gap of the ferroelectric CCPS is around 1.22 eV. The ultraviolet photoelectron spectroscopy (UPS) analysis of CCPS is presented in Figure 5.4a. By combining the UPS and SKPM measurement results, the work function and valence band edge of CCPS are estimated to be about −5.54 and −6.32 eV relative to the vacuum level, respectively. Based on experimental and computational results, the energy band diagram of CCPS is constructed in Figure 5.4b.

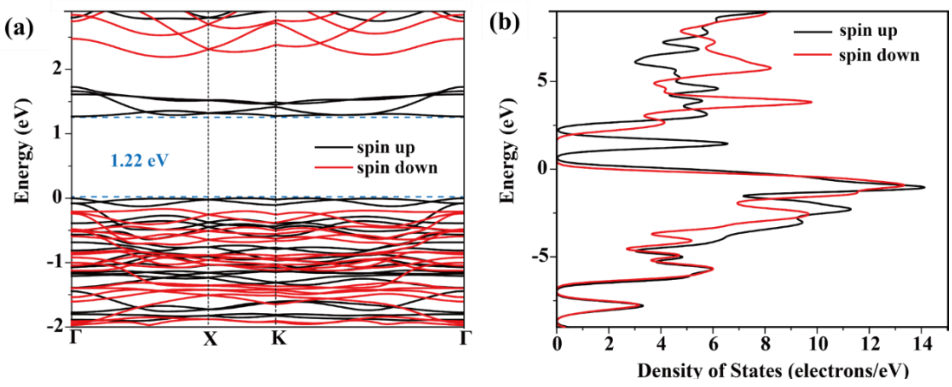


**Figure 5.3** Simulation of the (a) electronic band structure and (b) DOS of CCPS in ferroelectric phase.

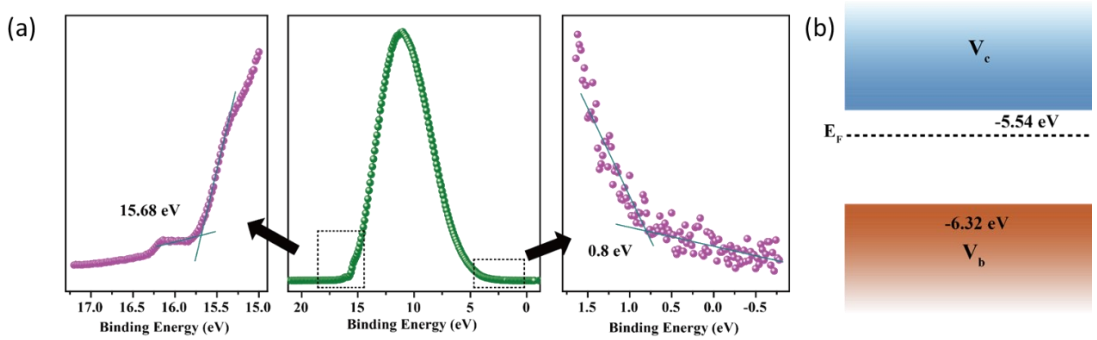


**Figure 5.4** (a) UPS study of single crystalline CCPS. (b) Energy band diagram of CCPS sketched based on theoretical and experimental data.

## 5.3 Performance of ferroelectric CCPS-based nanoelectronic devices

### 5.3.1 Ferroelectric tunneling junction

A ferroelectric tunneling junction (FTJ) is a nanoelectronic device which utilizes the unique spontaneous polarization field of ferroelectrics to regulate the electron transferring an ultrathin channel material. Typically, an FTJ device consist of vertical metal-ferroelectric layer-metal structure in which an ultrathin layer of ferroelectric material is sandwiched between two metal electrodes. The electric polarization direction of the ferroelectric channel layer can be reversed with the application of external bias. Consequently, the band alignment at the metal-ferroelectric interfaces is modified, tuning the electron transport characteristics and enhancing (suppressing) the tunneling of electron through the ultrathin ferroelectric layer. As a vdW layered ferroelectric material, ultrathin CCPS nanoflakes can be easily obtained through mechanical exfoliation and simple FTJ device can be fabricated by dry transfer method with good contact interfaces.

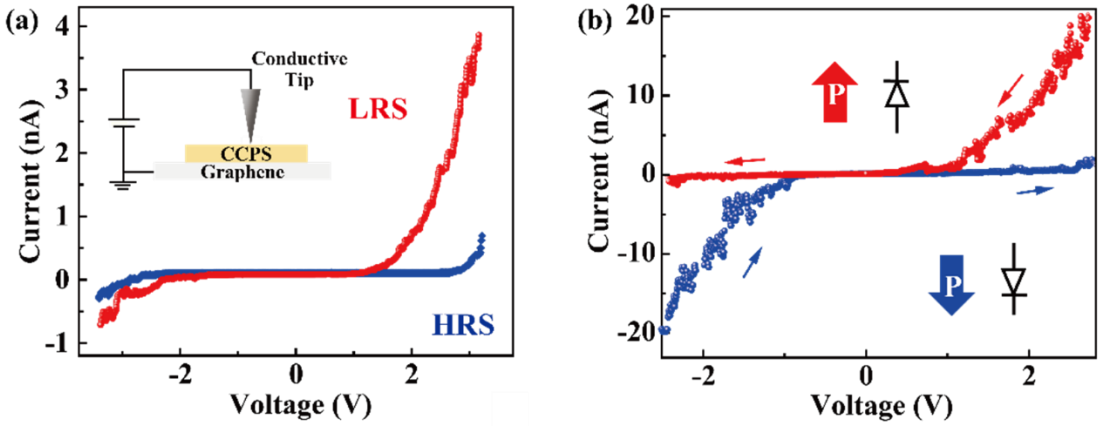


**Figure 5.5** (a) *I–V* characteristic of a vertical Pt/CCPS/MLG FTJ device with 3.3-nm-thick CCPS by voltage sweeping back and forth. (b) *I–V* characteristic of a representative Pt/CCPS/Pt resistive switching ferroelectric diode, with the channel CCPS nanoflake of 8.5 nm thick.

In order to demonstrate the potential applications of robust ferroelectric properties, vertical FTJ device based on 2D CCPS nanosheets and monolayer graphene (MLG) were constructed. The electron transfer characteristics were examined using C-AFM technique and the Pt/Ir coated conductive tip was adopted as the top electrode of the CCPS-based FTJ device, as schematically shown in the inset of Figure 5.5a. Figure 5.5a presents the *I-V* curve of a Pt/CCPS/MLG junction device with a 3.3 nm thick CCPS layer. When subjected to an external voltage of ± 4 V, respectively, polarization switching of the ferroelectric CCPS layer is induced, and the atomically thin ferroelectric channel layer is thin enough for electrons to tunnel through. Upon polarization reversal, two distinct resistance states are present, where the low-resistance state (LRS) and high-resistance state (HRS) correspond to the "ON" and “OFF “states

of a memory device, and the spontaneous ferroelectric polarization endows it with non-volatile property. The on/off ratio of the CCPS FTJ device, which refers to the ratio between in the LRS current and HRS current, is around $10^2$, comparable to the performance of FTJ devices fabricated using other conventional ferroelectric materials[159,160]. Figure 5.6 shows the schematic energy band diagram of the Pt/CCPS/MLG FTJ device, based on the theoretical calculation and experimental results in the previous section.

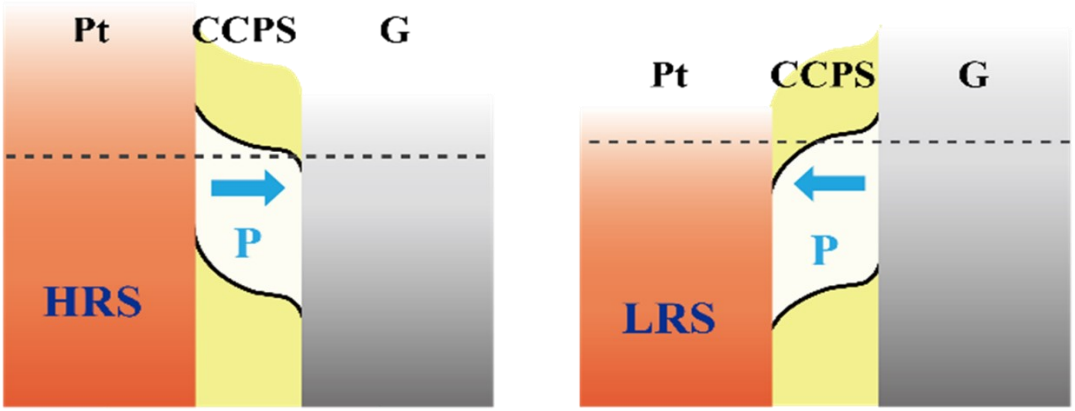


**Figure 5.6** Schematic of the band structure of the Pt/CCPS/MLG FTJ device.

## 5.3.2 Ferroelectric diode

Apart from tunneling junction device, the versatile device incorporations of ultrathin ferroelectric CCPS layers were also illustrated through vertical ferroelectric diodes. As shown in Figure 5.5b, the *I-V* characteristics of CCPS-based ferroelectric diode exhibit typical rectifying and bipolar resistive switching behaviors. The VFD

device demonstrates a similar on/off ratio of $10^2$ and the direction of the diode can be reversed by applying an external electric field. Current rectification and diode switching behaviors are always observable in VFD devices fabricated with different thicknesses of CCPS, as presented in Figure 5.7a-c, indicating good repeatability and reliability of the 2D CCPS-based VFD devices.

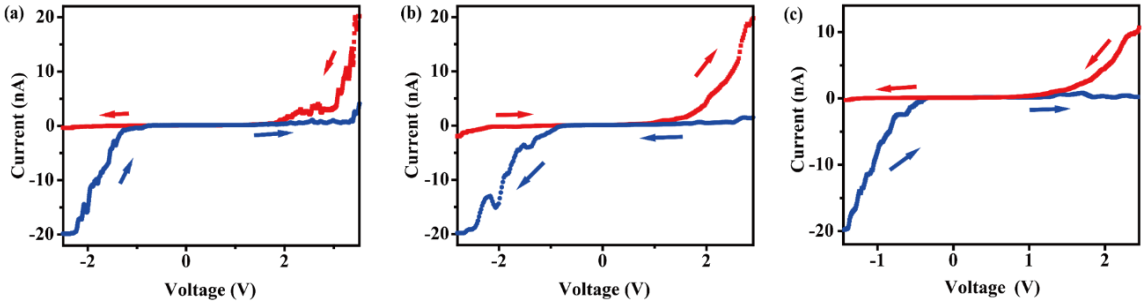


**Figure 5.7** Electrical characterization of CCPS-based VFDs. (a)-(c) Resistive switching characteristics of the Pt/CCPS/Pt-structured VFDs with CCPS nanosheets of 7.2, 9.3, and 9.9 nm thick, respectively.

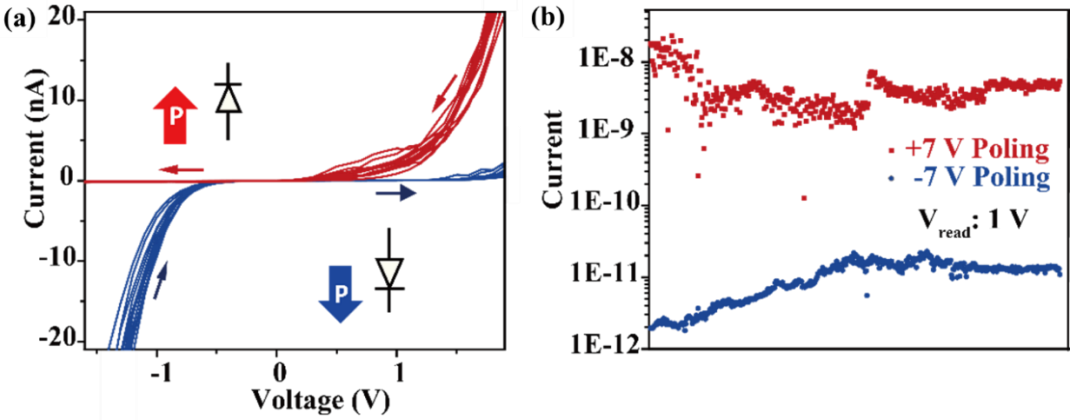


**Figure 5.8** (a) Cycling measurement of the resistive switching characteristics and (b) retention test of the HRS and LRS states of the CCPS-based VFD.

The endurance of the bipolar resistive switching in the CCPS-based VFDs was measured by repeating the *I-V* measurements for more than 20 cycles, as shown in Figure 5.8a. The result suggests that the hysteresis behavior and operation voltage of the tested ferroelectric diode remain almost unchanged, demonstrating good cycle endurance in the *I-V* characteristics of the CCPS-based VFD devices. Furthermore, Figure 5.8b shows the current output of a representative CCPS-based VFD device at a read voltage of 1 V, after writing with + 7 V (red) and - 7 V (blue), alternatively. The on/off ratio can be maintained at around $10^2$ after 1500 cycles of reading, indicating a good retention of the electric polarization state in the 2D CCPS. Figure 5.9 shows the sketched energy band diagram of the CCPS-based ferroelectric diodes, providing insights into the underlying mechanism governing the observed electrical characteristics. In addition to the 2D CCPS nanoflakes, VFD was also fabricated using thicker exfoliated CCPS flakes to illustrate the modulable ferroelectric polarization in CCPS with various sample thickness. Figure 5.10 displays the *I-V* curve measured from an Au/CCPS/Au ferroelectric diode with a 280-nm-thick CCPS. Characteristic resistance switching behavior is also clearly distinguished, and the on/off ratio is significantly enhanced, reaching up to $10^5$. Although the electric characterization results of the CCPS-based FTJ and VFD devices were obtained with simple and non-optimized device architectures, they served as a proof-of-concept demonstration for the

promising potential of 2D CCPS for device applications, utilizing their intrinsic out-of-plane ferroelectricity, as non-volatile memories operating at ambient environment.

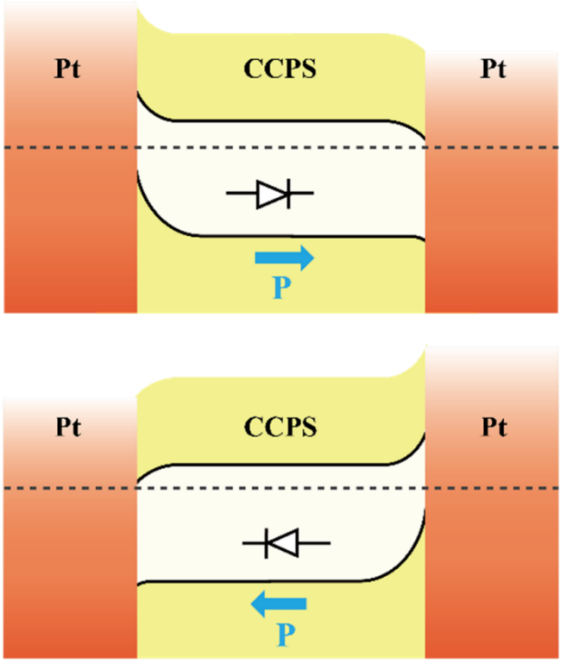


**Figure 5.9** Schematic of the band structure of the Pt/CCPS/Pt VFD.

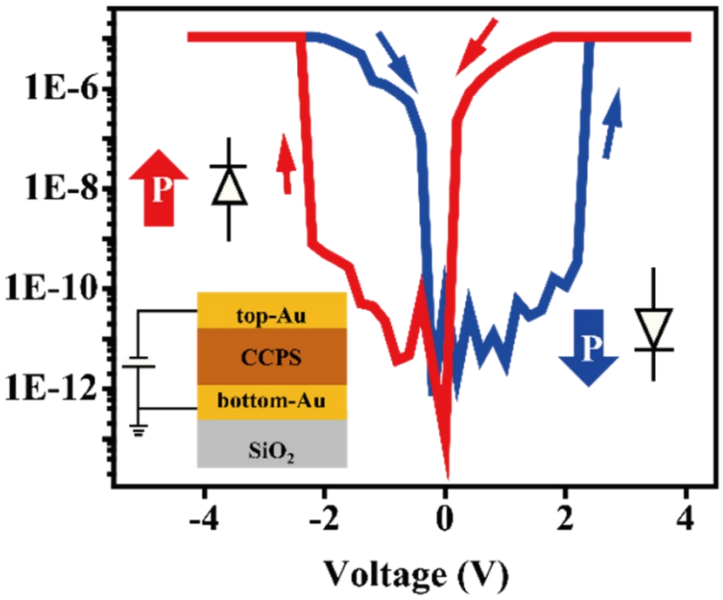


**Figure 5.10** *I-V* measurement of an Au/CCPS/Au VFD with a 280 nm thick ferroelectric CCPS flake.

### 5.3.3 Ferroelectric field-effect transistor

Ferroelectric field-effect transistor (FeFET) is one of the most common device architectures that utilize the unique characteristics of ferroelectric materials to manipulate the electrical transport properties of the semiconducting channel layer. In general, a FeFET consists of an insulating ferroelectric layer as the gate dielectric material. The electrical polarization field in the ferroelectric materials can be switched by applying sufficient gate voltage, thus regulating the electron transfer process of the semiconducting channel. Since ferroelectric polarization can be maintained when the gate voltage is removed, the FeFET can function as non-volatile storage devices. Herein, FeFET devices were constructed using 2D CCPS nanoflakes as the ferroelectric gate material and $WSe_2$ nanoflakes as the semiconducting channel. For the construction of the FeFETs, pairs of Au source and drain electrodes were pre-deposited by conventional photolithography followed by E-beam evaporation. 2D vdW layered materials $WSe_2$ and CCPS were exfoliated from bulk crystal and dry-transferred onto the pre-deposited Au electrodes subsequently. Lastly, Au gate electrode was layered onto the CCPS gate dielectric layer by dry transfer technique. It is worth-noting that the CCPS exhibits ion migration effect along the vertical direction, which can contribute to a nonneglectable leakage current in the FeFET device when certain gate voltage is applied[144]. A relatively

significant leakage current from the ferroelectric gate dielectric could degrade the device performance of the FeFETs for non-volatile storage and other applications.

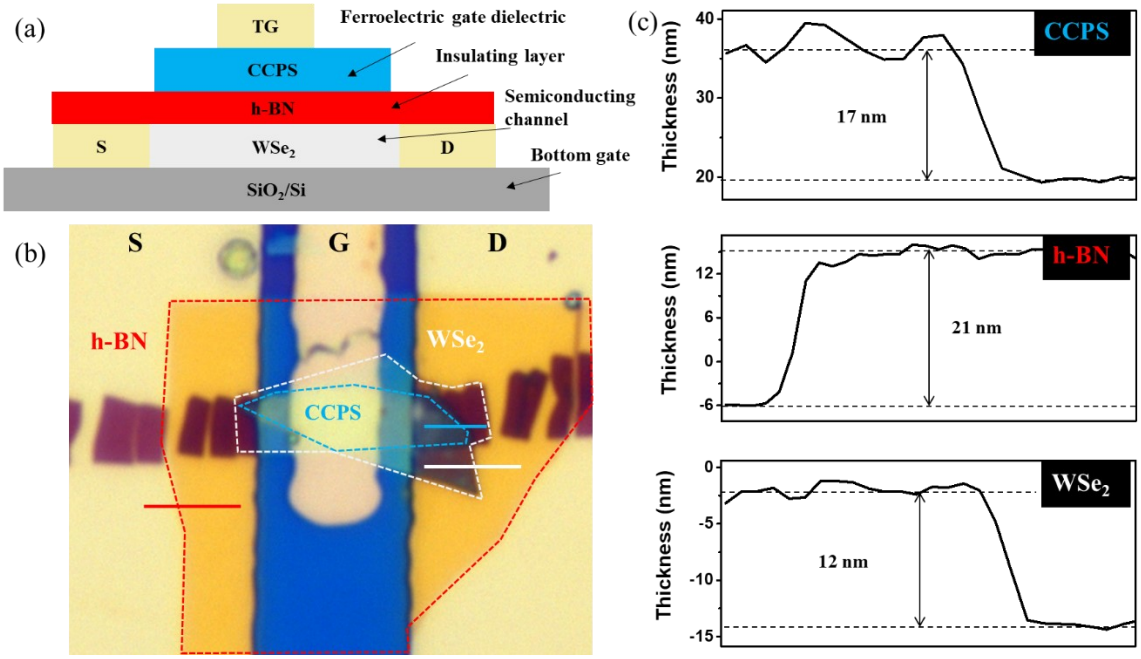


**Figure 5.11** (a) Schematic diagram of the fabricated FeFET device based on ferroelectric CCPS nanosheets. (b) Optical microscopy image of a prototype fabricated FeFET device. (c) AFM height profiles of the CCPS, h-BN, and $WSe_2$ nanosheets utilized in this FeFET device.

To enhance reliability and overall performance, it is essential to minimize the leakage current. Here, an ultrathin layer of the commonly used gate dielectric material h-BN is added in between the ferroelectric CCPS layer and the semiconducting $WSe_2$ channel. The leakage current of the FeFETs fabricated without additional insulating h-BN layers, and that with different thicknesses of 2D h-BN sheets were measured. As illustrated in Figure 5.12a and b, when no h-BN layer is used and when 7 nm thick h-

BN nanosheets is included, the gate current is rather high reaching 10 nA when gate voltage sweep of 6 V is applied. When a 20 nm h-BN is used, the gate current is significantly reduced to less than 1 pA (see Figure 5.12 c). A thicker h-BN layer can suppress the leakage current more effectively, but at the same time also requires higher gate voltage to switch the ferroelectric polarization of the CCPS and thus a higher power consumption. Therefore, h-BN nanoflakes of thickness at around 20-30 nm were selected to reduce the leakage current of the FeFET devices. Figures 5.11 b and c display the optical microscopy image and the AFM height profiles of the CCPS, h-BN, and $WSe_2$ nanosheets of a prototype fabricated 2D FeFET device. For material characterization, Raman spectra of individual exfoliated CCPS and $WSe_2$ nanosheets, and the stacked CCPS/ $WSe_2$ heterostructure are measured as shown in Figure 5.13, and are consistent with the reported Raman vibrations in previous literatures[29].

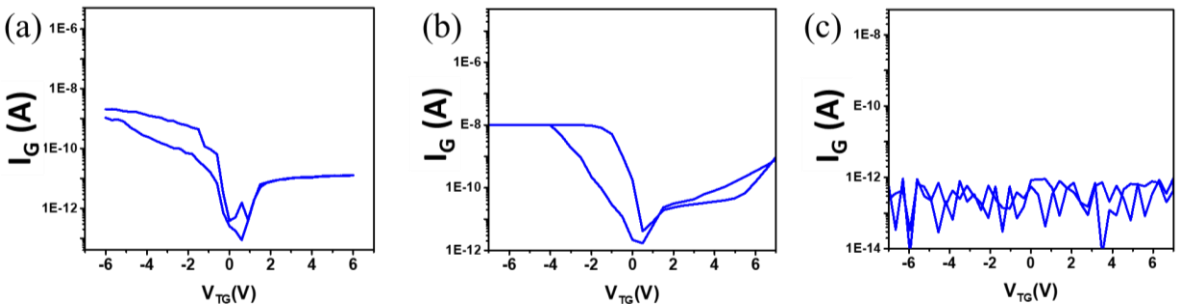


**Figure 5.12** Leakage current (gate current) measured from different FeFET devices in which (a) h-BN is not used, and (b) 7 nm h-BN and (c) 20 nm h-BN layer are utilized.

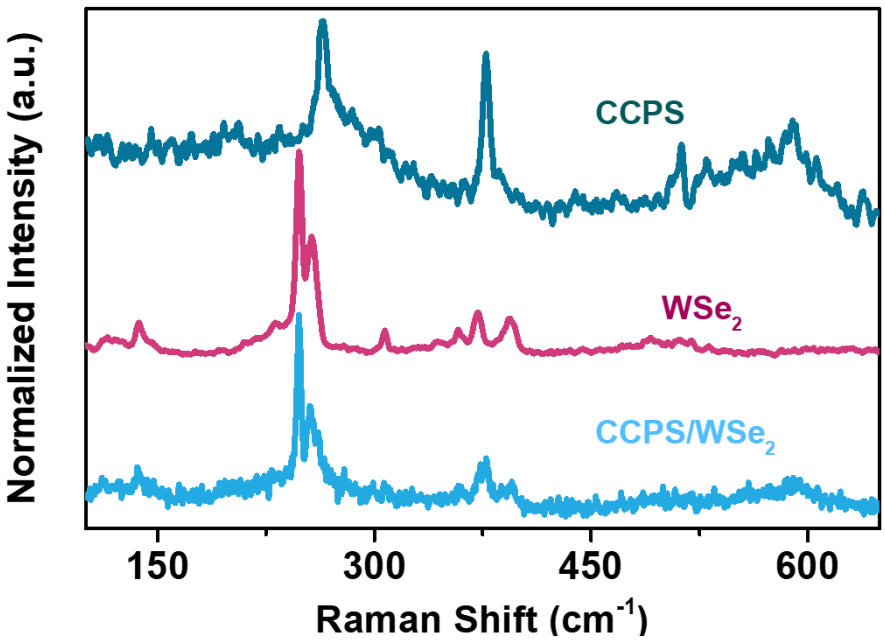


**Figure 5.13** Raman spectra of 2D CCPS, $WSe_2$, and stacked CCPS/$WSe_2$ layers.

Figure 5.14 shows the electrical characterization of a CCPS/h-BN/ $WSe_2$ 2D vdW heterostructure FeFET at room temperature. The transfer characteristic ($I_{DS}$-$V_{DS}$) of the 2D semiconducting channel $WSe_2$ is presented in Figure 5.14a. Figure 5.14b indicates the $I_{DS}$−$V_{TG}$ characteristics measured at top-gate voltage sweeping from −5 to 5 V and at drain-to-source voltage ($V_{DS}$) from 0.01 to 0.5 V. The gate leakage current measured at $V_{DS}$ of 0.1 V has a magnitude below a few pA and is always smaller than the $I_{DS}$ at all values of gate voltages (see Figure 5.14c). Therefore, the leakage current through the top ferroelectric gate shall have negligible effect on the $I_{DS}$−$V_{TG}$ characteristics of the FeFETs. The transfer characteristics exhibit an obvious ferroelectric hysteresis loop at different values of $V_{DS}$. When a higher $V_{DS}$ is applied, the difference between the LRS

and the HRS becomes larger, leading to a higher on/off ratio. Figure 5.14c shows the variations in the $I_{DS}-V_{TG}$ characteristics when the sweep gate voltage increases from ± 3 V to ± 6 V. Clear ferroelectric hysteresis loops can always be observed, and the memory window of hysteresis loops of the FeFET device can be tuned by applying different gate voltages. With a larger gate voltage sweep, a larger memory window is illustrated, suggesting that the gate voltage applied to the FeFETs can utilized for improved memory performance. The on/off ratio between the LRS and HRS of the FeFET devices reaches around $10^4$, as shown in Figure 5.14b and c. Figure 5.14d presents the source-to-drain current ($I_{DS}$) measured at $V_{DS}$ from 0 to 2 V, with gate voltage from 0 to -6 V, respectively. The $I_{DS}$-$V_{DS}$ transfer characteristics of the FeFET demonstrate typical transistor behavior, where the source-to-drain current increases when subjected to a higher magnitude of gate voltage bias. The LRS and RHS of the CCPS-based FeFET represent the on and off states for non-volatile memory storage. The endurance of the LRS and RHS of the hysteresis in the $I_{DS}-V_{TG}$ characteristics is measured over 100 consecutive polarization reversal cycles by ± 7 V gate voltage sweep, and the source-to-drain current is read at -1 V gate voltage. The magnitude of $I_{DS}$ as shown in Figure 5.14e remains almost unchanged over 100 cycles. The performance of the CCPS-based FeFETs are comparable to other 2D ferroelectrics-based FeFET devices reported previously[107].

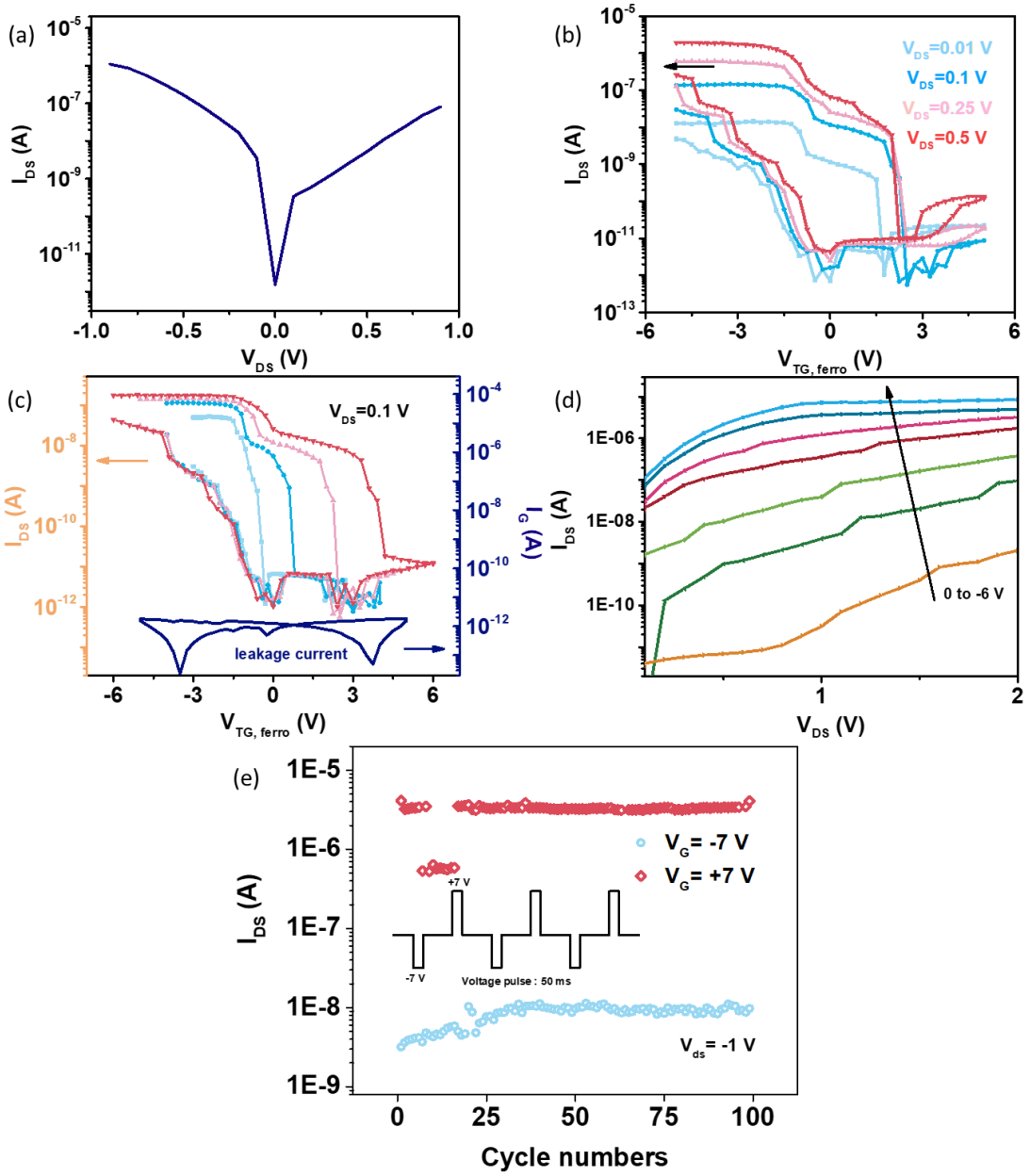


**Figure 5.14** (a) Transfer characteristic ($I_{DS}$-$V_{DS}$) of the 2D semiconducting $WSe_2$ channel when no gate voltage is applied. (b) $I_{DS}$−$V_{TG}$ characteristics of the FeFET device measured at top-gate voltage sweep from −5 to 5 V and at $V_{DS}$ from 0.01 to 0.5 V. (c) $I_{DS}$−$V_{TG}$ characteristics at different gate voltage sweeps. (d) The distribution of HRS and LRS of the CCPS-based FeFET device in 100 consecutive polarization reversal by ± 7 V gate voltage sweep and read at -1 V gate voltage.

## 5.4 Summary

In this chapter, nanoelectronic devices of different structures including ferroelectric tunneling junction, vertical ferroelectric diode, and ferroelectric field-effect transistor were fabricated, which utilize the ferroelectric properties of 2D CCPS for carious functionalities. Without any specific optimization on the ferroelectric material or device structure, the constructed CCPS-based nanodevices showed comparable device performance with other conventional and 2D layered ferroelectric materials. These experimental findings, achieved from simple and non-optimized device architectures, can serve as proof-of-concept demonstrations for the potential of harnessing the intrinsic out-of-plane ferroelectricity in 2D CCPS for use in room-temperature non-volatile data storage applications.

# Chapter 6 Conclusions and Future Prospects

## 6.1 Conclusions

The introduction of 2D vdW layered materials has shown extensive promise in overcoming the limitations of intrinsic size effect and constraints of lattice mismatch in ultrathin traditional piezoelectric and ferroelectric materials. They offer new prospects to achieve piezoelectric and ferroelectric properties at low dimensions. Although many 2D materials have been reported to exhibit intrinsic out-of-plane piezoelectricity, they generally possess lower piezoelectric coefficients than conventional piezoelectric materials. Hence, the discovery of novel 2D layered materials with strong piezoelectricity, particularly along the out-of-plane direction, would help facilitate the development and implementation of high-performance nanoscale piezotronic devices. Also, compared to the wealth of theoretical predictions of vertical ferroelectricity in various 2D layered materials, the corresponding experimental validations and investigations into the fundamental mechanisms remain relatively limited. With significant progress in the exploration from 2D materials to devices, the thesis studied further the piezoelectric and ferroelectric characteristics in vdW layered metal thiophosphates and their applications. The main findings of the thesis are summarized below.

The layer-dependent out-of-plane piezoelectric response of CIPS nanoflakes was quantitatively examined, and the piezotronic effect in CIPS-based devices was revealed. Through the PFM technique, the piezoelectric $d_{33}$ coefficient of few-layer CIPS is estimated to be 17.4 pm $V^{-1}$, larger than that of the other currently reported 2D vdW piezoelectric materials. The vertical piezoelectric response of CIPS nanosheets increases when thickness increases. Furthermore, 2D CIPS-based piezoelectric nanogenerator (PENG) devices were fabricated, exhibiting an output power density of up to 70.4 nW $cm^{-2}$. These findings enable new opportunities for CIPS to be integrated into energy harvesting devices and other piezotronic applications.

On the other hand, stable room-temperature ferroelectricity in the 2D vdW layered CCPS was discovered, and the origin of the observed ferroelectricity was studied from an atomic perspective. The spontaneous polarization of CCPS was measured to be 16.05 μC $cm^{-2}$, and electric polarization reversal was realized in CCPS nanoflakes with a thickness down to 2.6 nm. Notably, the STEM technique revealed that the out-of-plane ferroelectricity intrinsically originates from the off-center arrangement of Cu ions to the same side within the vertical layer, leading to non-zero spontaneous electric polarization modulable by external bias. Additionally, different device structures based on CCPS nanoflakes, which include FTJ, ferroelectric diode, and FeFET were

demonstrated and their performance for non-volatile memory was examined. These results provide a further understanding of the emerged ferroelectricity in this 2D layered metal thiophosphate material and demonstrate the potential for the realization of novel multifunctional nanodevices.

## 6.2 Future prospects

The vdW layered metal thiophosphates are fascinating materials which offer a rich playground for researchers in tailoring their physicochemical properties through engineering on their compositions. By incorporating diverse functional metal cations, the electronic structure and conductivity can be modulated, and functional properties such as ferroelectricity can be realized. In this work, the robust piezoelectric and ferroelectric effect in two metal thiophosphate materials, CIPS and CCPS, are sufficiently analyzed and validated. The diverse potential applications of these functional characterizations were demonstrated through device structures such as piezoelectric nanogenerators, ferroelectric tunneling junction, ferroelectric diode, as well as ferroelectric-gated FET.

Combining the unique characteristics of 2D vdW materials, 2D vdW piezoelectric and ferroelectric metal thiophosphate materials can be incorporated with other 2D

functional materials to form vdW heterostructure devices free from the restriction of lattice mismatch. These advantages enable the development of high-performance, flexible, and energy-efficient multifunctional devices ranging from piezoelectric sensors, energy harvesting devices, wearable electronics, non-volatile memory, and artificial synapses. By coupling the various intriguing functionalities of CIPS and CCPS, such as electrical anisotropy, ion migration effect, pyroelectric, piezoelectric, and ferroelectric effect at room temperature, novel devices with exceptional functionalities and performance can be conceived and achieved in the future. For example, coupling the strong piezoelectric effect in CIPS and semiconducting with excellent photoresponse in certain 2D materials, vdW heterostructures can be designed and constructed for applications as highly quality low-dimensional flexible, multifunctional sensors, self-powered and energy harvesting systems. Through specific consideration of the electrode material, matching the band gap and work function of the ferroelectric CIPS and CCPS can contribute to high-performance nonvolatile devices.

In this work, FeFETs based on non-optimized 2D CCPS were fabricated, in which the ferroelectric characteristics endorse the transistor devices with nonvolatile functionality. For nonvolatile memory applications, the performance of FeFETs, including the memory window, on/off ratio, operating voltage, power computation, and

reliability can be improved through proper device design and optimization of materials. Furthermore, different external stimuli such as light illumination and strain application have also shown the feasibility of modifying the ferroelectric polarization in 2D ferroelectrics. In recent years, with tremendous efforts in the field of 2D vdW ferroelectric materials, nanoelectronic and optoelectronic devices possessing superior performance and even unprecedented functions are highly anticipated and may give rise to extraordinary discovery.

Besides, the ability to stabilize ferroelectricity in atomically-thin layered ferroelectrics is particularly important. For instance, the practical performance of piezoelectric and ferroelectric-incorporated devices relies strongly on the polarization strength as well as the repeatability of the bipolar polarization reversal. When subjected to repeated polarization switching cycles, the overall device performance degrades with a gradual decrease in spontaneous polarization, known as ferroelectric fatigue. The phenomenon of ferroelectric fatigue generally appears in traditional ferroelectric materials which can result in a higher current leakage, reduced effective polarization, and even device failure, severely limiting their implementation into practical applications. While the fundamental research and device application of 2D vdW ferroelectrics is still in the early stage, it is highly desiring to investigate the long-term

endurance and ferroelectric fatigue, particularly in vdW layered CIPS and CCPS where prominent ion migration effect along the polarization direction is present. Further theoretical and experimental studies are necessary to obtain deeper understanding of the underlying fatigue mechanisms and develop strategies to address this challenge. For example, advanced *in-situ* atomic-resolution STEM characterization and more comprehensive analysis on the electrical properties and performance can be conducted in the future.

# References


1 Novoselov, K. S. *et al.* Electric Field Effect in Atomically Thin Carbon Films. *Science* **306**, 666-669 (2004). https://doi.org:10.1126/science.1102896

2 Changgu, L., Xiaoding, W., Jeffrey, W. K. & James, H. Measurement of the elastic properties and intrinsic strength of monolayer graphene. *Science* **321**, 385-388 (2008). https://doi.org:10.1126/science.1157996

3 Balandin, A. A. *et al.* Superior thermal conductivity of single-layer graphene. *Nano Lett.* **8**, 902-907 (2008). https://doi.org:10.1021/nl0731872

4 Nair, R. R. *et al.* Fine structure constant defines visual transparency of graphene. *Science* **320**, 1308-1308 (2008). https://doi.org:10.1126/science.1156965

5 Chen, Z., Lin, Y.-M., Rooks, M. J. & Avouris, P. Graphene nano-ribbon electronics. *Physica E Low Dimens. Syst. Nanostruct.* **40**, 228-232 (2007). https://doi.org:10.1016/j.physe.2007.06.020

6 Bonaccorso, F., Hasan, T., Sun, Z. & Ferrari, A. C. Graphene photonics and optoelectronics. *Nat. Photonics* **4**, 611-622 (2010). https://doi.org:10.1038/nphoton.2010.186

7 Lin, Y.-m., Xia, F., Valdes-Garcia, A., Mueller, T. & Avouris, P. Ultrafast graphene photodetector. *Nat. Nanotechnol.* **4**, 839-843 (2009). https://doi.org:10.1038/nnano.2009.292

8 Bolotin, K. I. *et al.* Ultrahigh electron mobility in suspended graphene. *Solid State Commun.* **146**, 351-355 (2008). https://doi.org:10.1016/j.ssc.2008.02.024

9 Wang, Q. H., Kalantar-Zadeh, K., Kis, A., Coleman, J. N. & Strano, M. S. Electronics and optoelectronics of two-dimensional transition metal dichalcogenides. *Nat. Nanotechnol.* **7**, 699-712 (2012). https://doi.org:10.1038/nnano.2012.193

10 Jariwala, D., Sangwan, V. K., Lauhon, L. J., Marks, T. J. & Hersam, M. C. Emerging device applications for semiconducting two-dimensional transition metal dichalcogenides. *ACS Nano* **8**, 1102-1120 (2014). https://doi.org:10.1021/nn500064s

11 Li, W. & Li, J. Ferroelasticity and domain physics in two-dimensional transition metal dichalcogenide monolayers. *Nat. Commun.* **7**, 10843 (2016). https://doi.org:10.1038/ncomms10843

12 Xu, X., Yao, W., Xiao, D. & Heinz, T. F. Spin and pseudospins in layered transition metal dichalcogenides. *Nat. Phys.* **10**, 343-350 (2014). https://doi.org:10.1038/nphys2942

13 Mao, J., Wu, Z., Guo, F. & Hao, J. Strain-induced performance enhancement of a monolayer photodetector via patterned substrate engineering *ACS Appl. Mater. Interfaces.* **14**, 36052-36059 (2022). https://doi.org:10.1021/acsami.2c09632

14 Kalantar-zadeh, K. *et al.* Two dimensional and layered transition metal oxides. *Appl. Mater. Today* **5**, 73-89 (2016).

15 Ma, W. *et al.* Piezoelectricity in multilayer black phosphorus for piezotronics and nanogenerators. *Adv. Mater.* **32**, e1905795 (2020). https://doi.org:10.1002/adma.201905795

16 Wu, Z. *et al.* Large-scale growth of few-layer two-dimensional black phosphorus. *Nat. Mater.* **20**, 1203-1209 (2021). https://doi.org:10.1038/s41563-021-01001-7

17 Zhao, Y. *et al.* Piezoelectric substrate-induced strain engineering on tuning polarized Raman spectra of crystalline black phosphorus. *Appl. Phys. Lett.* **122** (2023). https://doi.org:10.1063/5.0143759

18 Pang, S. Y., Io, W. F., Wong, L. W., Zhao, J. & Hao, J. Efficient energy conversion and storage based on robust fluoride-free self-assembled 1D niobium carbide in 3d nanowire network. *Adv. Sci.* **7**, 1903680 (2020).

19 Pang, S.-Y., Io, W.-F. & Hao, J. Facile atomic-level tuning of reactive metal–support interactions in the Pt QDs@ HF-free mxene heterostructure for accelerating pH-universal hydrogen evolution reaction. *Adv. Sci.* **8**, 2102207 (2021). https://doi.org:10.1002/advs.202102207

20 Mannix, A. J., Kiraly, B., Hersam, M. C. & Guisinger, N. P. Synthesis and Chemistry of Elemental 2D Materials. *Nat. Rev. Chem.* **1** (2017). https://doi.org:10.1038/s41570-016-0014

21 Pang, S.-Y. *et al.* Universal Strategy for HF-Free Facile and Rapid Synthesis of Two-Dimensional Mxenes as Multifunctional Energy Materials. *J. Am. Chem. Soc.* **141**, 9610-9616 (2019).

22 Jonathan, N. C. *et al.* Two-dimensional nanosheets produced by liquid exfoliation of layered materials. *Science* **331**, 568-571 (2011). https://doi.org:10.1126/science.1194975

23 Io, W. F. *et al.* Temperature- and thickness-dependence of robust out-of-plane ferroelectricity in CVD grown ultrathin van der Waals α-$In_2Se_3$ layers. *Nano Res.* **13**, 1897-1902 (2020). https://doi.org:10.1007/s12274-020-2640-0

24 Yang, Z. & Hao, J. Recent progress in 2D layered III–VI semiconductors and their heterostructures for optoelectronic device applications. *Adv. Mater. Technol.* **4**, 1900108 (2019).

25 Guo, F. *et al.* Achieving reinforcement learning in a three-active-terminal

neuromorphic device based on a 2D vdW ferroelectric material. *Mater. Horiz.* **10**, 3719-3728 (2023).

26 Pang, S.-Y., Io, W.-F., Wong, L.-W., Zhao, J. & Hao, J. Direct and in situ Growth of 1T′ $MoS_2$ and 1T $MoSe_2$ on Electrochemically Synthesized MXene as an Electrocatalyst for Hydrogen Generation. *Nano Energy* **103**, 107835 (2022). https://doi.org:10.1016/j.nanoen.2022.107835

27 Guo, F. *et al.* Multifunctional optoelectronic synapse based on ferroelectric van der Waals heterostructure for emulating the entire human visual system. *Adv. Funct. Mater.* **32**, 2108014 (2022).

28 Io, W. F. *et al.* Strong piezoelectric response in layered CuInP2S6 nanosheets for piezoelectric nanogenerators. *Nano Energy* **99**, 107371 (2022). https://doi.org:10.1016/j.nanoen.2022.107371

29 Zhao, Y. *et al.* Piezo-phototronic effect in 2D α-$In_2Se_3$/$WSe_2$ van der Waals heterostructure for photodetector with enhanced photoresponse. *Adv. Opt. Mater.* **9**, 2100864 (2021).

30 Han, W. *et al.* Phase-Controllable Large-Area Two-Dimensional $In_2Se_3$ and Ferroelectric Heterophase Junction. *Nat. Nanotech.* **18**, 55–63 (2023). https://doi.org:10.1038/s41565-022-01257-3

31 Whatmore, R. in *Springer Handbook of Electronic and Photonic Materials* (eds Safa Kasap & Peter Capper) 1-1 (Springer International Publishing, 2017).

32 Valasek, J. Piezo-electric and allied phenomena in Rochelle salt. *Phys. Rev.* **17**, 475 (1921).

33 Grinberg, I. *et al.* Perovskite oxides for visible-light-absorbing ferroelectric and photovoltaic materials. *Nature* **503**, 509-512 (2013). https://doi.org:10.1038/nature12622

34 Dawber, M., Rabe, K. M. & Scott, J. F. Physics of thin-film ferroelectric oxides. *Rev. Mod. Phys.* **77**, 1083-1130 (2005). https://doi.org:10.1103/RevModPhys.77.1083

35 Jie, W. & Hao, J. Graphene-based hybrid structures combined with functional materials of ferroelectrics and semiconductors. *Nanoscale* **6**, 6346-6362 (2014). https://doi.org:10.1039/c3nr06918d

36 Wang, B. & Woo, C. H. Curie temperature and critical thickness of ferroelectric thin films. *J. Appl. Phys.* **97** (2005). https://doi.org:10.1063/1.1861517

37 Gao, P. *et al.* Possible absence of critical thickness and size effect in ultrathin perovskite ferroelectric films. *Nat. Commun.* **8**, 1-8 (2017).

38 Zheng, F. *et al.* Above 1% efficiency of a ferroelectric solar cell based on the Pb(Zr, Ti)$O_3$ film. *J. Mater. Chem. A* **2**, 1363-1368 (2014).

39 Scott, J. F. Applications of modern ferroelectrics. *Science* **315**, 954-959 (2007). https://doi.org:10.1126/science.1129564

40 Yuan, Y., Xiao, Z., Yang, B. & Huang, J. Arisingapplications of ferroelectric materials in photovoltaic devices. *J. Mater. Chem. A* **2**, 6027-6041 (2014). https://doi.org:10.1039/c3ta14188h

41 Li, M. *et al.* A family of oxide ion conductors based on the ferroelectric perovskite $Na_{0.5}Bi_{0.5}TiO_3$. *Nat. Mater.* **13**, 31-35 (2014). https://doi.org:10.1038/nmat3782

42 Junquera, J. & Ghosez, P. Critical thickness for ferroelectricity in perovskite ultrathin films. *Nat. Mater.* **422**, 506-509 (2003).

43 Sai, N., Kolpak, A. M. & Rappe, A. M. Ferroelectricity in Ultrathin Perovskite Films. *Phys. Rev. B* **72**, 020101 (2005).

44 Lee, D. *et al.* Emergence of room-temperature ferroelectricity at reduced dimensions. *Science* **349**, 1314-1317 (2015).

45 Fong, D. D. *et al.* Ferroelectricity in ultrathin perovskite films. *Science* **304**, 1650-1653 (2004).

46 Tsvetkov, N., Lu, Q., Sun, L., Crumlin, E. J. & Yildiz, B. Improved chemical and electrochemical stability of perovskite oxides with less reducible cations at the surface. *Nat. Mater.* **15**, 1010-1016 (2016). https://doi.org:10.1038/nmat4659

47 Scott, J. F. & Dawber, M. Oxygen-Vacancy Ordering as a Fatigue Mechanism in Perovskite Ferroelectrics. *Appl. Phys. Lett.* **76**, 3801-3803 (2000). https://doi.org:10.1063/1.126786

48 Cui, C., Xue, F., Hu, W.-J. & Li, L.-J. Two-dimensional materials with piezoelectric and ferroelectric functionalities. *npj 2D Mater. Appl.* **2**, 1-14 (2018).

49 Yuan, S. *et al.* Ferroelectric-driven performance enhancement of graphene field-effect transistors based on vertical tunneling heterostructures. *Adv. Mater.* **28**, 10048-10054 (2016).

50 Müller, J. *et al.* Ferroelectricity in simple binary $ZrO_2$ and $HfO_2$. *Nano Lett.* **12**, 4318-4323 (2012). https://doi.org:10.1021/nl302049k

51 Wu, W. *et al.* Piezoelectricity of single-atomic-layer $MoS_2$ for energy conversion and piezotronics. *Nature* **514**, 470-474 (2014). https://doi.org:10.1038/nature13792

52 Meyer, J. C. *et al.* The structure of suspended graphene sheets. *Nature* **446**, 60-63 (2007). https://doi.org:10.1038/nature05545

53 Duerloo, K.-A. N., Ong, M. T. & Reed, E. J. Intrinsic piezoelectricity in two-

dimensional materials. *J. Phys. Chem. Lett.* **3**, 2871-2876 (2012). https://doi.org:10.1021/jz3012436

54 Han, S. A. *et al.* Point-defect-passivated $MoS_2$ nanosheet-based high performance piezoelectric nanogenerator. *Adv. Mater.* **30**, 1800342 (2018). https://doi.org:10.1002/adma.201800342

55 Blonsky, M. N., Zhuang, H. L., Singh, A. K. & Hennig, R. G. Ab Initio prediction of piezoelectricity in two-dimensional materials. *ACS Nano* **9**, 9885-9891 (2015). https://doi.org:10.1021/acsnano.5b03394

56 Wang, L. *et al.* 2D piezotronics in atomically thin zinc oxide sheets: Interfacing gating and channel width gating. *Nano energy* **60**, 724-733 (2019). https://doi.org:10.1016/j.nanoen.2019.03.076

57 Wang, L. *et al.* Ultrathin piezotronic transistors with 2 nm channel lengths. *ACS Nano* **12**, 4903-4908 (2018). https://doi.org:10.1021/acsnano.8b01957

58 Wang, X. *et al.* Subatomic deformation driven by vertical piezoelectricity from CdS ultrathin films. *Sci. Adv.* **2**, e1600209-e1600209 (2016). https://doi.org:10.1126/sciadv.1600209

59 Fei, R., Li, W., Li, J. & Yang, L. Giant piezoelectricity of monolayer group IV monochalcogenides: SnSe, SnS, GeSe, and GeS. *Appl. Phys. Lett.* **107**, 173104 (2015). https://doi.org:10.1063/1.4934750

60 Yin, H., Gao, J., Zheng, G.-P., Wang, Y. & Ma, Y. Giant piezoelectric effects in monolayer group-V binary compounds with honeycomb phases: a first-principles prediction. *J. Phys. Chem. C* **121**, 25576-25584 (2017). https://doi.org:10.1021/acs.jpcc.7b08822

61 Kim, S. K. *et al.* Directional dependent piezoelectric effect in CVD grown monolayer $MoS_2$ for flexible piezoelectric nanogenerators. *Nano energy* **22**, 483-489 (2016). https://doi.org:10.1016/j.nanoen.2016.02.046

62 Lee, G.-J. *et al.* Piezoelectric energy harvesting from two-dimensional boron nitride nanoflakes. *ACS Appl. Mater. Interfaces* **11**, 37920-37926 (2019). https://doi.org:10.1021/acsami.9b12187

63 Li, Y. *et al.* Probing symmetry properties of few-layer $MoS_2$ and h-BN by optical second-harmonic generation. *Nano Lett.* **13**, 3329-3333 (2013). https://doi.org:10.1021/nl401561r

64 Hallil, H. *et al.* Strong piezoelectricity in 3R-$MoS_2$ flakes. *Adv. Electron. Mater.*, 2101131 (2022).

65 Chang, K. *et al.* Discovery of robust In-plane ferroelectricity in atomic-thick SnTe. *Science* **353**, 274-278 (2016).

66 Fei, Z. *et al.* Ferroelectric Switching of a Two-Dimensional Metal. *Nature* **560**,

336-339 (2018). https://doi.org:10.1038/s41586-018-0336-3

67 Yuan, S. *et al.* Room-temperature ferroelectricity in $MoTe_2$ down to the atomic monolayer limit. *Nat. Commun.* **10**, 1-6 (2019). https://doi.org:10.1038/s41467-019-09669-x

68 Xue, F. *et al.* Multidirection piezoelectricity in mono- and multilayered hexagonal α-$In_2Se_3$. *ACS Nano* **12**, 4976-4983 (2018). https://doi.org:10.1021/acsnano.8b02152

69 Zhou, Y. *et al.* Out-of-plane piezoelectricity and ferroelectricity in layered α-$In_2Se_3$ nanoflakes. *Nano Lett.* **17**, 5508-5513 (2017). https://doi.org:10.1021/acs.nanolett.7b02198

70 Guo, Y., Zhou, S., Bai, Y. & Zhao, J. Enhanced piezoelectric effect in Janus group-III chalcogenide monolayers. *Appl. Phys. Lett.* **110**, 163102 (2017). https://doi.org:10.1063/1.4981877

71 Wang, Y. *et al.* Piezoelectric responses of mechanically exfoliated two-dimensional $SnS_2$ nanosheets. *ACS Appl. Mater. Interfaces* **12**, 51662-51668 (2020). https://doi.org:10.1021/acsami.0c16039

72 Yang, P.-K. *et al.* Tin disulfide piezoelectric nanogenerators for biomechanical energy harvesting and intelligent human-robot interface applications. *Nano energy* **75**, 104879 (2020). https://doi.org:10.1016/j.nanoen.2020.104879

73 Fei, R., Kang, W. & Yang, L. Ferroelectricity and phase transitions in monolayer group-iv monochalcogenides. *Phys. Rev. Lett.* **117**, 097601 (2016).

74 Shirodkar, S. N. & Waghmare, U. V. Emergence of ferroelectricity at a metal-semiconductor transition in a 1T monolayer of $MoS_2$. *Phys. Rev. Lett.* **112**, 157601 (2014). https://doi.org:10.1103/PhysRevLett.112.157601

75 Xiao, C. *et al.* Elemental ferroelectricity and antiferroelectricity in group-V monolayer. *Adv. Funct. Mater.* **28**, 1707383-n/a (2018). https://doi.org:10.1002/adfm.201707383

76 Ding, W. *et al.* Prediction of intrinsic two-dimensional ferroelectrics in In2Se3 and other III2-VI3 van der Waals materials. *Nat. Commun.* **8**, 14956 (2017).

77 Xu, B. *et al.* Monolayer AgBiP2Se6: an atomically thin ferroelectric semiconductor with out-plane polarization. *Nanoscale* **9**, 8427-8434 (2017). https://doi.org:10.1039/C7NR02461D

78 Reimers, J. R., Tawfik, S. A. & Ford, M. J. J. C. s. Van der Waals forces control ferroelectric–antiferroelectric orderingin $CuInP_2S_6$ And $CuBiP_2S_6$ laminar materials. *Chem. Sci.* **9**, 7620-7627 (2018).

79 You, L. *et al.* In-plane ferroelectricity in thin flakes of van der Waals hybrid perovskite. *Adv. Mater.* **30**, e1803249-n/a (2018).

https://doi.org:10.1002/adma.201803249

80 Higashitarumizu, N. *et al.* Purely in-plane ferroelectricity in monolayer SnS at room temperature. *Nat. Commun.* **11**, 1-9 (2020). https://doi.org:10.1038/s41467-020-16291-9

81 Belianinov, A. *et al.* $CuInP_2S_6$ room temperature layered ferroelectric. *Nano Lett.* **15**, 3808-3814 (2015).

82 Cui, C. *et al.* Intercorrelated In-Plane and Out-of-Plane Ferroelectricity in Ultrathin Two-Dimensional Layered Semiconductor $In_2Se_3$. *Nano Lett.* **18**, 1253-1258 (2018). https://doi.org:10.1021/acs.nanolett.7b04852

83 Xue, F. *et al.* Room-temperature ferroelectricity in hexagonally layered α-$In_2Se_3$ nanoflakes down to the monolayer limit. *Adv. Funct. Mater.* **28**, n/a (2018). https://doi.org:10.1002/adfm.201803738

84 Xiao, J. *et al.* Intrinsic Two-Dimensional Ferroelectricity with Dipole Locking. *Phys. Rev. Lett.* **120**, 227601 (2018). https://doi.org:10.1103/PhysRevLett.120.227601

85 Yasuda, K., Wang, X., Watanabe, K., Taniguchi, T. & Jarillo-Herrero, P. Stacking-engineered ferroelectricity in bilayer boron nitride. *Science* **372**, 1458-1462 (2021). https://doi.org:10.1126/science.abd3230

86 Shayesteh Zeraati, A. *et al.* Improved synthesis of $Ti_3C_2T_x$ MXenes resulting in exceptional electrical conductivity, high synthesis yield, and enhanced capacitance. *Nanoscale* **13**, 3572-3580 (2021). https://doi.org:10.1039/D0NR06671K

87 Sui, F. *et al.* Sliding ferroelectricity in van der Waals layered γ-InSe semiconductor. *Nat. Commun.* **14**, 36 (2023). https://doi.org:10.1038/s41467-022-35490-0

88 Wang, X. *et al.* Interfacial ferroelectricity in rhombohedral-stacked bilayer transition metal dichalcogenides. *Nat. Nanotech.* **17**, 367-371 (2022). https://doi.org:10.1038/s41565-021-01059-z

89 Rogée, L. *et al.* Ferroelectricity in untwisted heterobilayers of transition metal dichalcogenides. *Science* **376**, 973-978 (2022). https://doi.org:10.1126/science.abm5734

90 Bian, R. *et al.* Developing fatigue-resistant ferroelectrics using interlayer sliding switching. *Science*, eado1744 (2024). https://doi.org:10.1126/science.ado1744

91 Susner, M. A., Chyasnavichyus, M., McGuire, M. A., Ganesh, P. & Maksymovych, P. Metal thio-and selenophosphates as mltifunctional van der Waals layered materials. *Adv. Mater.* **29**, 1602852 (2017).

92 Liu, F. *et al.* Room-temperature ferroelectricity in $CuInP_2S_6$ ultrathin flakes. *Nat.*

*Commun.* **7**, 12357-12357 (2016). https://doi.org:10.1038/ncomms12357

93 You, L. *et al.* Origin of giant negative piezoelectricity in a layered van der Waals ferroelectric. *Sci. Adv.* **5**, 3780-3780 (2019). https://doi.org:10.1126/sciadv.aav3780

94 Maisonneuve, V., Payen, C. & Cajipe, V. B. On $CuCrP_2S_6$: copper disorder, stacking distortions, and magnetic ordering. *J. Solid State Chem.* **116**, 208-210 (1995). https://doi.org:10.1006/jssc.1995.1204

95 Cho, K. *et al.* Tunable Ferroelectricity in van der Waals Layered Antiferroelectric $CuCrP_2S_6$. *Adv. Funct. Mater.* **32**, 2204214 (2022).

96 Park, C. B. *et al.* Observation of Spin-Induced Ferroelectricity in a Layered van der Waals Antiferromagnet $CuCrP_2S_6$. *Adv. Electron. Mater.* **8**, 2101072 (2022).

97 Lai, Y. *et al.* Two-dimensional ferromagnetism and driven ferroelectricityin van der Waals $CuCrP_2S_6$. *Nanoscale* **11**, 5163-5170 (2019).

98 Jiang, D. *et al.* Flexible electronics based on 2D transition metal dichalcogenides. *J. Mater. Chem. A* **10**, 89-121 (2022). https://doi.org:10.1039/D1TA06741A

99 Lin, L., Bi, X., Gu, Y., Wang, F. & Ye, J. Surface-enhanced Raman scattering nanotags for bioimaging. *J. Appl. Phys.* **129** (2021). https://doi.org:10.1063/5.0047578

100 Shao, G. Work function and electron affinity of semiconductors: doping effect and complication due to fermi level pinning. *Energy Environ. Mater.* **4**, 273-276 (2021). https://doi.org:https://doi.org/10.1002/eem2.12218

101 Clark, S. *et al.* First Principles Methods Using CASTEP. *Z. fur Krist. - Cryst. Mater.* **220**, 567-570 (2005). https://doi.org:10.1524/zkri.220.5.567.65075

102 Perdew, J. P., Burke, K. & Ernzerhof, M. Generalized Gradient Approximation Made Simple. *Phys. Rev. Lett.* **77**, 3865-3868 (1996). https://doi.org:10.1103/PhysRevLett.77.3865

103 Momma, K. & Izumi, F. VESTA 3 for three-dimensional visualization of crystal, volumetric and morphology data. *J. Appl. Cryst.* **44**, 1272-1276 (2011). https://doi.org:https://doi.org/10.1107/S0021889811038970

104 Lee, C., Wei, X., Kysar, J. W. & Hone, J. Measurement of the elastic properties and intrinsic strength of monolayer graphene. *Science* **321**, 385-388 (2008). https://doi.org:10.1126/science.1157996

105 Xia, F., Mueller, T., Lin, Y. M., Valdes-Garcia, A. & Avouris, P. Ultrafast graphene photodetector. *Nat. Nanotechnol.* **4**, 839-843 (2009). https://doi.org:10.1038/nnano.2009.292

106 Niu, L. *et al.* Controlled synthesis and room-temperature pyroelectricity of

$CuInP_2S_6$ ultrathin flakes. *Nano energy* **58**, 596-603 (2019). https://doi.org:10.1016/j.nanoen.2019.01.085

107 Si, M., Liao, P.-Y., Qiu, G., Duan, Y. & Ye, P. D. Ferroelectric field-effect transistors based on $MoS_2$ and $CuInP_2S_6$ two-dimensional van der Waals heterostructure. *ACS Nano* **12**, 6700-6705 (2018). https://doi.org:10.1021/acsnano.8b01810

108 Ding, R. *et al.* Effective piezo-phototronic enhancement of flexible photodetectors based on 2D hybrid perovskite ferroelectric single-crystalline thin-films. *Adv. Mater.* **33**, 2101263 (2021). https://doi.org:10.1002/adma.202101263

109 Cao, V. A. *et al.* Enhanced piezoelectric output performance of the SnS2/SnS heterostructure thin-film piezoelectric nanogenerator realized by atomic layer deposition. *ACS Nano* **15**, 10428-10436 (2021). https://doi.org:10.1021/acsnano.1c02757

110 Li, P. *et al.* A self-powered 2D-material sensor unit driven by a SnSe piezoelectric nanogenerator. *J. Mater. Chem. A* **9**, 4716-4723 (2021). https://doi.org:10.1039/d0ta10457d

111 Cui, X., Xu, Q., Ni, X., Zhang, Y. & Qin, Y. Atomic-thick 2D $MoS_2$/insulator interjection structures for enhancing nanogenerator output. *J. Mater. Chem. C* **6**, 899-896 (2018). https://doi.org:10.1039/c7tc05458k

112 Lee, J. H. *et al.* Reliable piezoelectricity in bilayer $WSe_2$ for piezoelectric nanogenerators. *Adv. Mater.* **29**, 1606667 (2017). https://doi.org:10.1002/adma.201606667

113 Yuan, S. *et al.* Enhanced piezoelectric response of layered $In_2Se_3/MoS_2$ nanosheet-based van der Waals heterostructures. *ACS Appl. Nano Mater.* **3**, 11979-11986 (2020). https://doi.org:10.1021/acsanm.0c02513

114 Rao, R., Selhorst, R., Conner, B. S. & Susner, M. A. Ferrielectric-paraelectric phase transitions in layered $CuInP_2S_6$ and $CuInP_2S_6$-$In_{4/3}P_2S_6$ heterostructures: A Raman spectroscopy and x-ray diffraction study. *Phys. Rev. Mater.* **6**, 045001 (2022). https://doi.org:10.1103/PhysRevMaterials.6.045001

115 Kim, D. M. *et al.* Thickness dependence of structural and piezoelectric properties of epitaxial $Pb(Zr_{0.52}Ti_{0.48})O_3$ films on Si and $SrTiO_3$ substrates. *Appli. Phys. Lett.* **88**, 142904 (2006). https://doi.org:10.1063/1.2185614

116 Lian, L. & Sottos, N. R. Effects of thickness on the piezoelectric and dielectric properties of lead zirconate titanate thin films. *J. Appl. Phys.* **87**, 3941-3949 (2000). https://doi.org:10.1063/1.372439

117 Lu, A.-Y. *et al.* Janus monolayers of transition metal dichalcogenides. *Nat.*

*Nanotechnol.* **12**, 744-749 (2017). https://doi.org:10.1038/nnano.2017.100

118 Liu, S. & Cohen, R. E. Origin of negative longitudinal piezoelectric effect. *Phys. Rev. Lett.* **119**, 207601-207601 (2017). https://doi.org:10.1103/PhysRevLett.119.207601

119 Qi, Y. & Rappe, A. M. Widespread negative longitudinal piezoelectric responses in ferroelectric crystals with layered structures. *Phys. Rev. Lett.* **126**, 217601-217601 (2021). https://doi.org:10.1103/PhysRevLett.126.217601

120 Brehm, J. A. *et al.* Tunable quadruple-well ferroelectric van der Waals crystals. *Nat. Mater.* **19**, 43-48 (2020). https://doi.org:10.1038/s41563-019-0532-z

121 Nasr Esfahani, E., Li, T., Huang, B., Xu, X. & Li, J. Piezoelectricity of atomically thin $WSe_2$ via laterally excited scanning probe microscopy. *Nano Energy* **52**, 117-122 (2018). https://doi.org:10.1016/j.nanoen.2018.07.050

122 Brehm, J. A. *et al.* Tunable Quadruple-Well Ferroelectric van der Waals crystals. *Nat. Mater.* **19**, 43-48 (2020).

123 Neumayer, S. M. *et al.* The Concept of Negative Capacitance in Ionically Conductive Van der Waals Ferroelectrics. *Adv. Energy Mater.* **10**, 2001726 (2020). https://doi.org:https://doi.org/10.1002/aenm.202001726

124 Neumayer, S. M. *et al.* Giant negative electrostriction and dielectric tunability in a van der Waals layered ferroelectric. *Phys. Rev. Mat.* **3**, 024401 (2019). https://doi.org:10.1103/PhysRevMaterials.3.024401

125 Hu, L. & Huang, X. Peculiar electronic, strong in-plane and out-of-plane second harmonic generation and piezoelectric properties of atom-thick α-$M_2X_3$ (M= Ga, In; X= S, Se): role of spontaneous electric dipole orientations. *RSC Adv.* **7**, 55034-55043 (2017).

126 Lueng, C. M., Chan, H. L. W., Surya, C. & Choy, C. L. Piezoelectric coefficient of aluminum nitride and gallium nitride. *J. Appl. Phys.* **88**, 5360-5363 (2000). https://doi.org:10.1063/1.1317244

127 Katsouras, I. *et al.* The negative piezoelectric effect of the ferroelectric polymer poly(vinylidene fluoride). *Nat. Mater.* **15**, 78-84 (2016). https://doi.org:10.1038/nmat4423

128 Zhou, J. *et al.* Flexible Piezotronic Strain Sensor. *Nano Lett.* **8**, 3035-3040 (2008). https://doi.org:10.1021/nl802367t

129 Zhai, K. *et al.* Room-Temperature Nonvolatile Memory Based on a Single-Phase Multiferroic Hexaferrite. *Adv. Funct. Mater.* **28**, 1705771 (2018).

130 Kim, M.-K. & Lee, J.-S. Ferroelectric analog synaptic transistors. *Nano Lett.* **19**, 2044-2050 (2019).

131 Ramesh, R. & Spaldin, N. A. Multiferroics: progress and prospects in thin films.

*Nat. Mater.* **6**, 21-29 (2007).

132 Fiebig, M., Lottermoser, T., Meier, D. & Trassin, M. The evolution of multiferroics. *Nat. Rev. Mater.* **1**, 1-14 (2016).

133 Zhao, T. *et al.* Electrical control of antiferromagnetic domains in multiferroic $BiFeO_3$ films at room temperature. *Nat. Mater.* **5**, 823-829 (2006).

134 Gong, C. *et al.* Discovery of intrinsic ferromagnetism in two-dimensional van der Waals crystals. *Nature* **546**, 265-269 (2017). https://doi.org:10.1038/nature22060

135 Huang, B. *et al.* Layer-Dependent Ferromagnetism in a van der Waals Crystal Down to the Monolayer Limit. *Nature* **546**, 270-273 (2017). https://doi.org:10.1038/nature22391

136 Xu, C. *et al.* Two-Dimensional Ferroelasticity in van der Waals β'-$In_2Se_3$. *Nat. Commun.* **12**, 3665 (2021).

137 Jeong, J. *et al.* Ferroelastic–Ferroelectric Multiferroicity in van der Waals Rhenium Dichalcogenides. *Adv. Mater.* **34**, 2108777 (2022).

138 Wu, Z. *et al.* Intercalation-Driven Ferroelectric-to-Ferroelastic Conversion in a Layered Hybrid Perovskite Crystal. *Nat. Commun.* **13**, 3104 (2022).

139 Huang, C. *et al.* Prediction of Intrinsic Ferromagnetic Ferroelectricity in a Transition-Metal Halide Monolayer. *Phys. Rev. Lett.* **120**, 147601 (2018).

140 Zhang, D., Schoenherr, P., Sharma, P. & Seidel, J. Ferroelectric Order in van der Waals Layered Materials. *Nat. Rev. Mater.* **8**, 25-40 (2023).

141 Maisonneuve, V. *et al.* Ionic Conductivity in ferroic $CuInP_2S_6$ and $CuCrP_2S_6$. *Ferroelectrics* **196**, 257-260 (1997).

142 Chen, J. *et al.* Mimicking neuroplasticity via ion migration in van der Waals layered copper indium thiophosphate. *Adv. Mater.* **34**, 2104676 (2022).

143 Qi, J., Wang, H., Chen, X. & Qian, X. Two-Dimensional Multiferroic Semiconductors with Coexisting Ferroelectricity and Ferromagnetism. *Appl. Phys. Lett.* **113**, 043102 (2018).

144 Ma, R. R. *et al.* Nanoscale Mapping of Cu-Ion Transport in van der Waals Layered $CuCrP_2S_6$. *Adv. Mater. Inter.* **9**, 2101769 (2022).

145 Wang, X. *et al.* Electrical and Magnetic Anisotropies in van der Waals Multiferroic $CuCrP_2S_6$. *Nat. Commun.* **14**, 840 (2023).

146 Cajipea, V. *et al.* Copper ordering in lamellar $CuMP_2S_6$ (M= Cr, In): transition to an antiferroelectric or ferroelectric phase. *Ferroelectrics* **185**, 135-138 (1996).

147 Io, W. F. *et al.* Direct observation of intrinsic room-temperature ferroelectricity in 2D layered $CuCrP_2S_6$. *Nat. Commun.* **14**, 7304 (2023). https://doi.org:10.1038/s41467-023-43097-2

148 Susner, M., Rao, R., Pelton, A., McLeod, M. & Maruyama, B. Temperature-Dependent Raman Scattering and X-ray Diffraction Study of Phase Transitions in Layered Multiferroic $CuCrP_2S_6$. *Phys. Rev. Mater.* **4**, 104003 (2020).

149 Lucazeau, G. Effect of pressure and temperature on raman spectra of solids: anharmonicity. *J. Raman Spectrosc.* **34**, 478-496 (2003). https://doi.org:https://doi.org/10.1002/jrs.1027

150 Nishino, R., Fujita, T. C., Kagawa, F. & Kawasaki, M. Evolution of Ferroelectricity in Ultrathin $PbTiO_3$ Films as Revealed by Electric Double Layer Gating. *Sci. Rep.* **10**, 10864 (2020). https://doi.org:10.1038/s41598-020-67580-8

151 Chandra, P., Dawber, M., Littlewood, P. B. & Scott, J. F. Scaling of the Coercive Field with Thickness in Thin-Film Ferroelectrics. *Ferroelectrics* **313**, 7-13 (2004). https://doi.org:10.1080/00150190490891157

152 Jo, J. Y., Kim, Y. S., Noh, T. W., Yoon, J.-G. & Song, T. K. Coercive Fields in Ultrathin $BaTiO_3$ Capacitors. *Appl. Phys. Lett.* **89** (2006).

153 Tagantsev, A. K. & Stolichnov, I. A. Injection-Controlled Size Effect on Switching of Ferroelectric Thin Films. *Appl. Phys. Lett.* **74**, 1326-1328 (1999).

154 Dawber, M., Chandra, P., Littlewood, P. B. & Scott, J. F. Depolarization Corrections to the Coercive Field in Thin-Film Ferroelectrics. *J. Condens. Matter Phys.* **15**, L393 (2003). https://doi.org:10.1088/0953-8984/15/24/106

155 Lai, Y. *et al.* Two-Dimensional Ferromagnetism and Driven Ferroelectricity in van der Waals $CuCrP_2S_6$. *Nanoscale* **11**, 5163-5170 (2019).

156 Susner, M. A. *et al.* Cation–Eutectic Transition via Sublattice Melting in $CuInP_2S_6/In_{4/3}P_2S_6$ van der Waals Layered Crystals. *ACS Nano* **11**, 7060-7073 (2017). https://doi.org:10.1021/acsnano.7b02695

157 Shibata, N. *et al.* Differential phase-contrast microscopy at atomic resolution. *Nat. Phys.* **8**, 611-615 (2012).

158 Hao, X. F. *et al.* Structural and Ferroelectric Transitions in Magnetic Nickelate $PbNiO_3$. *New J. Phys.* **16**, 015030 (2014). https://doi.org:10.1088/1367-2630/16/1/015030

159 Chanthbouala, A. *et al.* Solid-state memories based on ferroelectric tunnel junctions. *Nat. Nanotech.* **7**, 101-104 (2012). https://doi.org:10.1038/nnano.2011.213

160 Gao, X. S., Liu, J. M., Au, K. & Dai, J. Y. Nanoscale ferroelectric tunnel junctions based on ultrathin $BaTiO_3$ film and Ag nanoelectrodes. *Appl. Phys. Lett.* **101**, 142905 (2012). https://doi.org:10.1063/1.4756918